


4-24-2018

Magnetic Phases of Large-Spin Ultracold Bosons: Quantum Dimer Models and Spin Liquid Phases

Todd C. Rutkowski

Binghamton University--SUNY, trutkow1@binghamton.edu

Follow this and additional works at: https://orb.binghamton.edu/dissertation_and_theses

 Part of the [Atomic, Molecular and Optical Physics Commons](#), and the [Condensed Matter Physics Commons](#)

Recommended Citation

Rutkowski, Todd C., "Magnetic Phases of Large-Spin Ultracold Bosons: Quantum Dimer Models and Spin Liquid Phases" (2018).
Graduate Dissertations and Theses. 59.
https://orb.binghamton.edu/dissertation_and_theses/59

This Dissertation is brought to you for free and open access by the Dissertations, Theses and Capstones at The Open Repository @ Binghamton (The ORB). It has been accepted for inclusion in Graduate Dissertations and Theses by an authorized administrator of The Open Repository @ Binghamton (The ORB). For more information, please contact ORB@binghamton.edu.

MAGNETIC PHASES OF LARGE-SPIN ULTRACOLD BOSONS:
QUANTUM DIMER MODELS AND SPIN LIQUID PHASES

BY

TODD C. RUTKOWSKI

BS, The College at Brockport: SUNY, 2011

DISSERTATION

Submitted in partial fulfillment of the requirements for
the degree of Doctor of Philosophy in Physics
in the Graduate School of
Binghamton University
State University of New York
2018

© Copyright by Todd Christopher Rutkowski 2018

All Rights Reserved

Accepted in partial fulfillment of the requirements for
the degree of Doctor of Philosophy in Physics
in the Graduate School of
Binghamton University
State University of New York
2018

April 24, 2018

Charles Nelson, Chair
Department of Physics, Applied Physics and Astronomy, Binghamton University

Michael Lawler, Faculty Adviser
Department of Physics, Applied Physics and Astronomy, Binghamton University

Pegor Aynajian, Member
Department of Physics, Applied Physics and Astronomy, Binghamton University

Christof Grewer, Outside Examiner
Department of Chemistry, Binghamton University

Abstract

This thesis investigates the plausibility of producing a quantum spin liquid (QSL) with ultracold bosonic atoms optically confined to the Mott insulating state. QSLs have received a great deal of attention for being an antiferromagnetic groundstate with many exotic properties, including the absence of local order, long-range entanglement, and fractionalized excitations. However, the identification and characterization of these phases in solid state systems remains a great challenge. Here we outline an alternate route to uncovering the QSL phase, which from the nature of spin angular momentum for ultracold atoms encounters many properties unique to these systems along the way. This proposal is possible because the magnetic exchange interactions for Mott insulating ultracold atoms are mediated by the hopping of whole atoms. Whole-atom exchange—a unique property of cold atoms—allows large fluctuations between the quantized Zeeman sublevels of each atomic spin. As we demonstrate, these fluctuations increase when large-spin atoms are used, or when interactions are tuned via optical Feshbach resonance (OFR). These strong quantum spin fluctuations inhibit classical magnetic ordering, and lead to a QSL ground state.

To illustrate the relationship between the spin magnitude, interaction strength, and QSL ground state, we present two distinct approaches to solving the relevant Hamiltonian. With mean field theory we find that for large spin ($f > 2$), and strong scattering through the spin-singlet channel, that magnetically-ordered Bose-Einstein condensates are unstable to the formation of a QSL. We then utilize Rayleigh-Schödinger perturbation theory to derive an effective Hamiltonian for our system in the Hilbert space of nearest-neighbor singlet coverings. At large spin this Hamiltonian

produces a type of quantum dimer model (QDM), which are known to possess QSL phases. We derive the QDM parameters t, t' and V as a function of spin on several lattices, finding they scale with the inverse number of Zeeman sublevels, $(2f + 1)^{-\epsilon}$. We then determine the proximity of the physically accessible states to the QSL phase, and discuss how other regions of the phase diagram may be accessed. We then conclude by highlighting several advantages to studying QSLs and QDMs with ultracold bosons.

For my family: past, present, and future.

Acknowledgements

I would like to begin by thanking the many people who have helped me in the process of writing this thesis. First, I would like to thank my research adviser, Dr. Michael Lawler, as without his assistance none of this would be possible. I am also thankful to have spent two summers working at the Laboratory for Atomic and Solid State Physics at Cornell University. During these summers, I developed a fruitful collaboration with Dr. Erich Mueller and Dr. Bhuvanesh Sundar, which led to new and exciting ways of thinking about our project, and to whom I owe many thanks. Additionally, I would like to thank my committee members, Dr. Nelson, Dr. Aynajian, and Dr. Grewer, for the time they have taken to help me complete my PhD requirements. This gratitude extends to all the professors who have supervised my studies over the years, and to my fellow graduate students and office mates, who have shared in the struggles and joys of my journey.

I also owe many thanks to my family, who have made me into the person that I am today. My father, David, for showing me the importance of hard work and sacrifice. My mother, Kalyn, whose belief in me kept me going through even the most difficult times. My sisters, Erin and Megan, who constantly inspire me with their strength and spirit. My grandparents, who showed me the importance of family, and my Grandpa Fred, who taught me the true value of an education. Finally, I would like to thank my loving wife, Charity, as none of my this would have been possible without her unwavering support. Her smile and laughter has always given me a reason to keep pushing forward, and for that, I am forever grateful.

Contents

List of Tables	x
List of Figures	xiii
List of Abbreviations	xxii
1: Introduction	
1.1 The search for exotic magnetism	1
1.2 Thesis description	5
1.3 Thesis overview	6
2: Quantum Magnetism and Ultracold Atoms	
2.1 Magnetic phases in solid state systems	8
2.2 Quantum dimer models and quantum spin liquids	14
2.3 Exotic magnetic phases with ultracold atoms	23
3: A Spin Model for Ultracold Bosons	
3.1 The Bose-Hubbard model	32
3.2 Deriving an effective spin model	38
3.3 Tuning interactions with optical Feshbach resonance	42
3.4 A discussion of relevant energy scales	50
3.5 The phase diagram predicted by spinor mean field theory	54
4: Quantum Spin Liquids	
4.1 Spin liquid mean field theory	59
4.2 The short-ranged resonating valence bond ansatz	65
4.3 The spin nematic ansatz	77
4.4 Bose-Einstein condensate ground states	82
4.5 The experimental accessibility of quantum spin liquids	85
5: Quantum Dimer Models	
5.1 The singlet basis and the dimer basis	88
5.2 Exact diagonalization with small systems	94

5.3	Deriving a quantum dimer model for ultracold bosons	96
5.4	The quantum dimer model on different lattices	98
5.5	The phase diagram of the quantum dimer model	102
5.6	The experimental accessibility of the quantum dimer model	106
6: Conclusions		
Appendices		
A:	Calculations of atomic and lattice energy scales	110
B:	Rotational symmetry and related properties	113
C:	Path Integral Formulation of the QSL MF Theory	122
D:	Spin liquid mean field theory	127
E:	Raleigh-Schrödinger perturbation theory	136
F:	Deriving a quantum dimer model	138
	References	152

List of Tables

2.1	Atomic energy scales for two species of alkali atoms. These energies are used to calculate laser parameters needed to trap the atoms in an optical lattice, as discussed in Fig. 2.16. The optical lattice frequencies ω_L are tuned relative to the transition frequency between the highest occupied S orbital and the lowest unoccupied P orbital on the same shell. The detuning δ must be larger than both the spin-orbit and hyperfine splitting to produce degenerate angular momentum states in the lattice. The laser detuning and transition linewidth dictate the scattering rate of atoms out of the trap, which puts an upper-bound on the lifetime of cold atoms experiments.	28
3.1	Relevant length scales for two commonly used alkali atoms in an optical lattice at $T = 300$ pK. At these ultracold temperatures, the thermal de Broglie wavelength is much larger than the van der Waal's radius of their interaction potential. This results in an effective contact interaction, characterized by the s-wave scattering length a_0 at low energies. Since a_0 is much smaller than the lattice constant only onsite interactions are relevant.	33
3.2	S-wave scattering lengths for several commonly used bosonic isotopes. These values are determined by comparing multi-channel scattering calculations with experimental measurements of collisional dynamics and magnetic Feshbach resonances [127–129]. They include short-ranged isotropic contributions from magnetic DDIs, in addition to electronic Born-Oppenheimer molecular potentials [130, 131]. For ^{52}Cr and ^{164}Dy —which have large dipole moments—the scattering lengths vary greatly across different spin channels, and reliable values are difficult to extract by these methods. For alkali atoms on the other hand, the scattering lengths are known to high accuracy, and roughly the same through each channel	34
3.3	Ratios of lattice and interaction energy scales for particular lattice depths, in the absence of any Feshbach-tuned scattering. The lattice depths are chosen to satisfy $Ug_0 > t > E_{\text{dip}}$ and $\frac{4t^2}{Ug_0} > E_{\text{dip}}$, which are required for Eqs. 3.14 and 3.19 to be valid.	39

3.4	Ratios of lattice and interaction energy scales for particular lattice depths, with an optical Feshbach resonance tuning the scattering lengths such that $a_0 \sim a_B$. The lattice depths are chosen to satisfy $Ug_F > t > E_{\text{dip}}$ and $\frac{4t^2}{Ug_0} > \frac{4t^2}{Ug_2}, E_{\text{dip}}$. We see that even in the presence of a strong OFR, it is possible to choose parameters such that our approximations used to obtain Eqs. 3.14, 3.19, and 3.31 remain valid.	49
3.5	Experimental parameters used to calculate the lattice and interaction energy scales of Tab. 3.6. The hyperfine spin manifolds are chosen for their stability (see for example the discussion in Ref. [127]). The lattice depth and Feshbach tuning are chosen to satisfy the conditions in Tab. 3.4. The temperature is chosen to be towards the lower bound of achievable temperatures for Mott insulators (see for example Ref. [116]). The upper-bound for any external magnetic fields used in calculations.	50
3.6	Atomic and lattice energy scales for an alkali gas trapped in an optical lattice, in descending order of magnitude. Most parameters used in these calculations are provided in Tabs. 2.1 and 3.5. We point out that the nearest-neighbor DDI and the tensor light shifts from the photoassociation lasers are neglected in our treatment, which is acceptable since they are the smallest energy scales in the problem, and down by almost an order of magnitude from the exchange energy.	51
5.1	Pictorial derivation of the t and t' terms of the quantum dimer model on a square lattice. Blue lines indicate dimer bonds, while yellow lines indicate the empty bonds which $\hat{A}^\dagger \hat{A}$ act upon to move the system from $ b\rangle$ to $ c\rangle$ to $ a\rangle$. The multiplicity is the total number of terms in the Hamiltonian which produce identical dimer resonances, and is the product of the number of yellow lines in one single row. The kinetic resonances result in $t : 2\beta \square_{a,b}$ and $t' : 4\beta^2 \square \square_{a,b}$, while, the effective potential becomes $V : 2\beta^2(N_{\downarrow\downarrow} + N_{\downarrow\uparrow} + N_{\uparrow\downarrow}) \propto -4\beta^2 N_{\text{flip}} \delta_{a,b}$.	100
5.2	Coefficients of the quantum dimer model on different lattice geometries, determined from the method demonstrated pictorially for a square lattice in Tabs. 5.1 and 5.1. The large- f ground states on square and triangular lattices are determined by numerical diagonalization as discussed in section 5.2. The appearance of the second-order, three bond resonance t' is unique to the quantum dimer model as derived from the singlet Hamiltonian, Eq. 5.1.	103

F.1	Angular momentum quantum numbers for two commonly used species of alkali atoms. Shown are the electronic spin s , the electronic orbital angular momentum l , the nuclear spin i , and the hyperfine spin $f = i \pm j$, where $j = s + l$ is the total electronic angular momentum. The electronic magnetic moment relative to the Bohr magneton (μ_e/μ_B) and the nuclear magnetic moment relative to the nuclear magneton (μ_{nuc}/μ_N) are shown.	139
F.2	Pictorial derivation of the t and t' terms of the quantum dimer model on the triangular lattice. We note that there is a sub-leading contribution to the 4-site resonance. The kinetic resonances result in $t : 2(\beta + \beta^2)\square_{a,b}$ and $t' : 4\beta^2\square\square_{a,b}$. Meanwhile, the effective repulsive potential becomes $V : 4\beta^2 N_{\text{flip}}\delta_{a,b}$	151

List of Figures

2.1	The band structure of weakly interacting electrons in a 1-dimensional periodic potential. The band gap Δ characterizes the minimum energy needed to excite an electron from the valence band to the conduction band. The Pauli Exclusion principle dictates that no two fermions can occupy a single-particle state simultaneously. Therefore, the electronic ground state is found by filling up available energy states from low to high, resulting in a Fermi surface. This is in contrast to the ground state of bosonic systems in which all of the bosons may occupy the lowest-energy state simultaneously, and Bose-Einstein condensation may occur.	9
2.2	A pictorial representation of the Hubbard Model, where blue circles represent electrons, and the black solid line represents the underlying lattice potential. When an electron hops from one lattice site to another, the energy is reduced by t . If any site is doubly occupied, then the energy is increased by U . The ground state for $t \gg U$ is that of a band metal, where metallic or insulating behavior come from a filled valence band and a gap to the conduction band, as shown in Fig. 2.1. For $U \gg t$ the strong repulsive interactions quench the kinetic energy, and for one particle per site the system becomes a Mott insulator. . .	10
2.3	Three classical magnetic orders. (a) Ferromagnetism is responsible for macroscopically magnetic materials, such as iron bar magnets. (b) Antiferromagnetism is a magnetic ordering with zero macroscopic magnetization, and is found in many transition metal oxides. (c) Paramagnetism has no magnetic order, and the spins only align in response to an external applied field. Most chemical elements are paramagnetic, and both ferromagnetic and antiferromagnetic materials are paramagnetic at high temperatures.	11
2.4	Magnetic susceptibility for the classical magnetic orders. The susceptibility characterizes the material's response to changes in the external magnetic field. Both ferromagnetic and antiferromagnetic materials behave like paramagnets at high temperatures. Ferromagnets develop magnetic order below their Curie Temperature T_C , while antiferromagnets become ordered below their Néel Temperature, T_N	12

2.5	The inverse magnetic susceptibility as a function of temperature. The inverse susceptibility is useful for determining the sign of a material’s spin-exchange interactions, and therefore whether one expects a low-temperature ferromagnet or antiferromagnet. This is done by extrapolating the high-temperature behavior—which follows the Curie-Weiss Law ($\chi^{-1} \propto T - \Theta$)—to the temperature axis to determine the Curie-Weiss temperature. Paramagnets intercept at $T = 0$, while ferromagnets have a positive Curie-Weiss Temperature T_C . Antiferromagnetic materials will a negative Curie-Weiss Temperature Θ_{AF} . This is an important measurement in the determination of spin liquid candidates, as several materials show antiferromagnetic exchange interactions from their inverse susceptibility, but show no signs of magnetic ordering several orders of magnitude below their expected phase transition around $ \theta_{AF} $	13
2.6	A schematic phase diagram of the Hubbard Model. Tuning the ratio of the potential and kinetic energy U/t , the system passes from metal to insulator in what is known as the Mott transition. In the intermediate regime ($U/t \sim 1$), strong virtual hopping increases the charge and spin fluctuations. The enhanced spin fluctuations in this region can “melt” the classical spin ordering on geometrically frustrated lattices.	14
2.7	Geometrical frustration of Ising spins on a triangle. For antiferromagnetic interactions, each spin tries to align anti-parallel to its neighbors. For Ising spins constrained to point up or down along one axis on a triangular lattice, it is impossible to meet this criteria simultaneously for each spin, and so there may be a large number of degenerate “next-best” arrangements. Since the system cannot reach its ideal configuration, it is said to be frustrated. Spin fluctuations are be increased by the presence of geometrical frustration.	15
2.8	Example of the pictorial dimer representation used throughout this work. The two circles represent particles on sites A and B, and the solid line connecting them indicates that these spins are in a singlet state, or dimer. A singlet state consists of two quantum spins in a superposition of up and down states, resulting in a total spin moment of zero.	16
2.9	An example of a dimer covering on a square lattice. Shaded blue squares represent flippable plaquettes, in which the dimers may rearrange locally. Dimers on non-flippable plaquettes require non-local rearrangements in the form of closed loops. Defects where an atom is not paired to any dimer, known as a spinon, are fundamental excitations of this system.	17

2.10	Three phases of the quantum dimer model on a square lattice, which are encountered as the ratio of potential-to-kinetic energy (V/t) is varied. When the potential energy is negative ($V/t < 0$), the system will attempt to maximize the number of flippable plaquettes, resulting in the columnar phase. For $0 < V/t < 1$ the terms are comparable, and the plaquette phase emerges. The point $V/t = 1$ is a special point, known as the RK point, where the system behaves as a s-RVB spin liquid (described in Sec. 2.2.3). For all values of $V/t > 1$, the staggered phase, in which there are no flippable plaquettes, is the exact ground state.	18
2.11	Spinon confinement in a columnar VBC phase on a square lattice. Two spinons are created in pairs by breaking a nearest-neighbor singlet dimer, with some energy Δ . As one spinon moves away from its original location, it leaves behind a string of dimers which are distorted from the original columnar configuration (shown in red). If each unfavorable bond costs some energy ϵ , the energy to move the spinons a distance d apart grows as ϵd . When the energy of their separation costs more than the energy to create two new pairs ($\epsilon d > 2\Delta$), new spinons will be created at the ends of the string, resulting in a system which only has nearest-neighbor spinon pairs. This limiting of the possible separation distance is known as confinement.	21
2.12	Spinon deconfinement in a RVB spin liquid. To break a dimer and create a spinon pair requires some energy Δ . However, as each spinon is moved apart, they distort only the 4 bonds adjacent to themselves, limiting the energy needed for separation. Since there is no upper bound to the distance d at which they are found as isolated particles, they are said to be deconfined. Each lone spinon is considered a fractionalized excitation, in that they have a quantum number ($s = 1/2$) which is a fraction of the quantum number of the “unfractionalized” triplet excitation ($s = 1$).	22
2.13	The fractional occupation of the single-particle ground state, N_0/N . This quantity serves as the order parameter for the phase transition from a gas to a Bose-Einstein condensate. This second-order transition occurs at the critical temperature $T = T_C$, and in the vicinity of T_C this quantity takes the form $N_0/N \simeq (1 - T/T_C)^\epsilon$, where the critical exponent $\epsilon = 1/2$	24
2.14	The momentum distribution of a Bose-Einstein condensate, above and below the transition temperature. As the temperature is lowered below T_C , macroscopic occupation of the lowest momentum state occurs. This results in a sharp peak at the center of the momentum distribution, and is evidence of the growing occupation of the ground state.	24

2.15	Trapping mechanisms used to study cold atomic gases. A harmonic magnetic trap is used to confine the atoms within a vacuum, while optical lasers are used to cool the atoms via Doppler cooling. Additional lasers are used to create an optical lattice, which confines the atoms to a periodic lattice potential.	26
2.16	Energy structure of a two-level atomic system, which is optically coupled to an oscillating electric field of frequency ω_L . State $ g\rangle$ is the electronic ground state of the atom, while $ e\rangle$ is the first excited state, and is separated by an energy $\hbar\omega_e$. For the alkali atoms shown in Tab. 2.1, the laser detuning δ must be large enough to prevent sizable occupation of the excited state, which allows for an effective description in terms of the ground state. The detuning may be considered either “blue” or “red”, depending whether the laser energy is greater or less than the atomic transition frequency, respectively.	27
2.17	In an optical lattice, neutral atoms are trapped in the periodic wells of the laser potential via the AC Stark Shift. At low temperatures, the atoms in each potential well are approximated by a 3D harmonic oscillator. When the kinetic degrees of freedom have been frozen out, the remaining interaction is an effective spin-spin interaction. A ferromagnetic state is shown, but a multitude of the magnetic phases found in solid state systems are possible, as well as many phases which may be unique to cold atom systems.	29
2.18	A comparison of the whole-atom exchange and superexchange mechanisms in cold atoms and solid state. For atomic gases optically confined to the Mott state (top), the exchange of whole spin- f atoms leads to magnetic fluctuations on the order of $2f$. In the solid state by contrast (bottom), electron superexchange restricts fluctuations to order ~ 1 , which can be small compared to the total spin on each site. Therefore, large-spin atoms are an ideal tool with which to study fluctuation-driven states—especially those which are not readily accessible with solid state systems.	31
3.1	A schematic mean field phase diagram for the scalar Bose-Hubbard model, in which the interactions are spin independent. By tuning the optical lattice depth, the ratio t/U may be varied, and the system moves between the Mott insulator and superfluid phases—a feature of the model which was first proposed [132], and then successfully observed experimentally for the first time using ultracold atoms [57]. For spin-dependent interactions, one may assume a similar phase diagram, but with rich spin structure as a function of the different scattering lengths a_F	37

- 3.2 (a) The magnitude of t and Ug_F from Eq. 3.14, as calculated from Eqs. 3.11 and 3.13. (b) The magnitude of the exchange interactions from Eq. 3.19. These are shown in comparison to the nearest-neighbor dipole-dipole interaction, and as a function of lattice depth V_{trap} for $f = 1$ ^{23}Na atoms. For our description to be valid, we require that $Ug_0 > t > E_{\text{dip}}$ and $\frac{4t^2}{Ug_0} > E_{\text{dip}}$, which from these plots can be seen to occur for $V_{\text{trap}}/E_{\text{recoil}} \sim 5\text{--}15$, well within experimental limits. 40
- 3.3 A schematic of optical Feshbach resonance. Two alkali atoms in the $^nS_{1/2}$ ground state are coupled to a bound molecular state (of which there are many, each with differing spin and/or vibrational/rotational quantum numbers) through the use of a photoassociation laser. If the laser detuning δ_{PA} is large compared to the splitting of these molecular bound states, then photo-induced occupation of the molecular state will be small. The result is an effective shift in the scattering lengths of the ground state atoms. Additionally, since coupling to the molecular state depends on the total electronic angular momentum of the colliding atoms, and since the projections of different electronic states into the hyperfine basis are not equal, the shift through each spin channel will be different, resulting in the form of Eq. 3.28. 44
- 3.4 An example of some energy scales relevant to the optical Feshbach resonance proposed in Sec. 3.3. For alkali atoms, the photoassociation laser couples the $L = 0, S = 0$ ground state to the $L = 1, S = 0$ excited state. If the laser detuning δ_{PA} is large compared to the molecular and atomic hyperfine splitting, then different hyperfine states will not be resolved during this photoassociation, and so the process is independent of the nuclear spin. 46
- 3.5 A plot of α_F/α_0 from Eq. 3.28 for alkali atoms as a function of F . Since α_F monotonically decreases with increasing F , the $F = 0$ channel will exhibit the largest shift in scattering length for a given Feshbach tuning Θ_{Fesh} . For alkali atoms, the background scattering lengths are roughly equal, which allows OFR tuning to access the limit where $g_0 \ll g_{F \neq 0}$, resulting in the effective singlet Hamiltonian of Eq. 3.31. 48
- 3.6 Lattice and interaction energies, in the presence of an OFR which tunes the scattering lengths such that $a_0 \sim a_B$. This figure shows (a) the magnitude of t and Ug_F from Eq. 3.14 and (b) the magnitude of the exchange interactions from Eq. 3.19 compared to the DDI as a function of lattice depth for ^{23}Na , with a Feshbach tuning of $\Theta_{\text{Fesh}} = 20$. For Eq. 3.31 to be valid, we require that $Ug_F > t > E_{\text{dip}}$ and $\frac{4t^2}{Ug_0} > \frac{4t^2}{Ug_2}, E_{\text{dip}}$. From these plots, this region is seen to occur for $V_{\text{trap}}/E_{\text{recoil}} \sim 12\text{--}20$, which is within the range of experimental parameters. 49

3.7	Phase diagram for an $f = 1$ spinor condensate (such as ^{23}Na) in an external magnetic field $B_{\text{eff}} = \mu B/2J$. The ratio of the scattering lengths g_0/g_2 and may be tuned with an optical Feshbach resonance as described in Sec. 3.3. For zero magnetic field ($B_{\text{eff}} = 0$) the system is a spin nematic for $g_0/g_2 = (0, 1)$, which corresponds to the spinor condensate ground states found in Chap. 4, while for $g_0/g_2 = (-\infty, 0)$ and $g_0/g_2 = (1, \infty)$ the system is antiferromagnetic and ferromagnetic respectively. The application of a magnetic field expands the ferromagnetic region, and induces a small magnetization in the nematic state which points along the field axis. In this way, the phase contains aspects of both the nematic and ferromagnetic phases, and so we elect to call it the “mixed” phase. However, this phase is not to be confused with the mixed phase of the QDM.	56
3.8	Characterization of the spinor wavefunction for $B_{\text{eff}} = 0$. (a) Shows the expectation value of the spin projection along the quantization axis for spins on sublattice i (blue) and j (red). AF, N, and F denote the antiferromagnetic, nematic, and ferromagnetic phases respectively. (b) Shows the expectation values of the $k = 1$ (black) and $k = 2$ (blue) spherical tensor operators. It is seen that for $g_0/g_2 = (0, 1)$, where $\langle \hat{S}_z \rangle = 0$ the $k = 2$ component becomes large, while the $k = 1$ component goes to zero, indicating nematic order in this region. . . .	57
3.9	Characterization of the spinor wavefunction for $B_{\text{eff}} = 0.4$. (a) Shows the expectation value of the spin projection along the quantization axis for spins on sublattice i (blue) and j (red). AF, M, and F denote the antiferromagnetic, “mixed”, and ferromagnetic phases respectively. (b) Shows the expectation values of the $k = 1$ (black) and $k = 2$ (blue) spherical tensor operators. It is seen that within the mixed phase the $k = 2$ component becomes large, while the $k = 1$ component becomes small, and that both continuously approach their values in the ferromagnetic phase as g_0/g_2 is increased. This indicates that the “mixed” phase is a nematic state which is being biased in the applied field direction, hence the non-zero magnetization but large nematic-character to the spinor in this region.	58
4.1	Phase diagram of the s-RVB ansatz ($\alpha_{F \neq 0} \rightarrow \infty$) as a function of f . For $f \leq 2$ the ground state is a spin nematic with $\langle \mathbf{S} \rangle = 0$ and $\langle S_x^2 \rangle = \langle S_y^2 \rangle \neq \langle S_z^2 \rangle$ on each site. For $f > 2$, degeneracy of the magnetic sublevels enhances fluctuations, and the ground state becomes a short-range resonating valence bond (s-RVB) spin liquid.	70

4.2	Spin uncertainty vs. spin quantum number f on a log-log plot, calculated using the Q^{00} only large- f limit expansion. The uncertainty of a each component $\Delta\hat{S}_\alpha$, where $\alpha = \{x, y, z\}$, is given by Eq. 4.21, is seen to grow with increasing spin f . The uncertainty relative to the spin magnitude $S = \sqrt{f(f+1)}$ goes to a constant value of 1, indicating maximum spin uncertainty (and hence quantum fluctuations) in the large- f limit. This is in contrast to solid-state spin models, where electron mediated exchange interactions cause the relative magnitude of the spin fluctuations to decrease with increasing f , and so the spins behave more classically in the large-spin limit.	73
4.3	The mean field ground state is shown in Fig. 4.3a, and the ground state projected onto the physical one-particle-per-site Hilbert space is shown in Fig. 4.3b. Black dots represent sites on a 2×2 lattice. Blue lines represent a singlet between two atoms at sites i and j , created by $\hat{A}_{i,j}^{00\dagger}$, and a double bond is created by $(\hat{A}_{ij}^{00\dagger})^2$. Atoms exist only at the end of the bonds, and so a disconnected site is empty, a site which is a part of two bonds has two atoms, etc.	78
4.4	Phase diagram on the square lattice of the nematic ansatz as a function of f and α , where $\alpha = g_{F \neq 0}/g_0$ parametrizes the relative scattering lengths, as introduced by Eq. 4.31. The fluctuations responsible for the spin liquid state are enhanced by the increasing number of magnetic sublevels as one moves to large f , and by increased scattering through the singlet channel ($F = 0$) as one moves to large α . For $f \leq 2$ the system is nematic for all α , while for $\alpha = 1$ the spin liquid phase is not accessed at any f . The phase diagram for the triangular lattice is qualitatively similar in that the s-RVB region expands to smaller values of α , but condensate order still occurs for $f \leq 2$ at all interaction strengths.	81
4.5	The excitation gap as a function of inverse system size. For the spin liquid phase, the gap remains constant as the system is taken to large system sizes. For the spin nematic phase, the gap is roughly 2 orders of magnitude smaller, and decreases in a clear linear trend as the system size is increase. It is therefore clear that the phases are either a gapped spin liquid, or a gapless spinor condensate which possesses nematic symmetry.	83
4.6	Relative contribution from the higher-order scattering channels ($F > 0$) for an $f = 3$ system, as captured by the Q_R parameter defined in Eq. 4.32. In the spin liquid phase ($\alpha \gtrsim 18$) all pairings except the singlet pairing Q^{00} are negligible, while in the spin nematic phase ($\alpha \lesssim 18$) pairing through the non-zero angular momentum channels becomes relevant. Measurement of this parameter could allow observation of the quantum phase transition associated with the tuning of the scattering lengths.	86

5.1	Examples of singlet cover states. The numbers label the lattice sites, while connected sites represent a spin singlet between the atoms on those sites. In this example, $ a\rangle = \hat{A}_{1,2}^\dagger \hat{A}_{4,5}^\dagger \hat{A}_{3,6}^\dagger 0\rangle$. The notation $ (i, j) : a\rangle$ denotes a state where sites i and j are paired in a singlet, the original partners of i and j in $ a\rangle$ are paired in another singlet, and all the other bonds in $ a\rangle$ are left unchanged. This notation is used in the supplementary materials to derive an effective dimer model (Eq. 5.18).	90
5.2	Examples of transition graphs between non-orthogonal singlet coverings. The magnitude of the overlap is given by Eq. 5.5 and is shown in the figure for the two cases. The overlap S_{ab} comes from a single 4-site loop, and represents the largest possible overlap in magnitude. The overlap S_{ac} comes from a single 6-site loop, and is down in magnitude by a factor of $(2f + 1)^{-1}$. In the large- f limit, all singlet coverings become orthogonal as the overlaps approach zero.	92
5.3	Pictorial representation of an orthogonal dimer state constructed from non-orthogonal singlet coverings, as expressed in Eq. 5.7. A dimer state $ \bar{a}\rangle$ has an associated $\mathcal{O}(1)$ singlet covering $ a\rangle$, which is used to label the state. At $\mathcal{O}(f^{-1})$ and higher, it contains contributions from all coverings $ b\rangle$ which differ from $ a\rangle$ by a 4-site loop in their transition graph, including those which lie outside the nearest-neighbor-only Hilbert space.	93
5.4	Dimer-dimer correlations on a square lattice with periodic boundary conditions. The thicknesses of each bond represents the probability of measuring a dimer on that bond, relative to the reference dimer. (a) The large- f limit, with $f = 100$, shows a mixing of the columnar and plaquette orders. (b) For accessible spin values, such as $f = 3$ shown, the correlations weaken, but remain mixed.	95
5.5	Excitation energy as a function of the spin f . We find that the energy gap decreases as $(2f + 1)^{-1}$ in the large- f limit. For the experimentally accessible spins ($f = 1, \dots, 8$) we find the excitation energy ranges between roughly 0.16–0.9 (J/g_0). For an $f = 2$ system of ^{87}Rb , we may use Tab. 3.6 to determine that $\Delta E \simeq 0.9J/g_0 \simeq 7.5$ Hz. In this case, the nearest-neighbor DDI of $\sim 1.8\text{Hz}$ does <i>not</i> take the system outside of the nearest-neighbor dimer subspace spanned by our QDM.	96

- 5.6 The phase diagram for the quantum dimer model on a 4×4 square lattice, obtained by exact diagonalization of Eq. 5.18. We find columnar and staggered phases as shown in Fig. 2.10, as well as a mixed phase which contains components of both the columnar and plaquette phase. We discover that the region accessible by using atoms of different hyperfine spin f lies along a line approaching $V/t = 0$ as $f \rightarrow \infty$. Notably, the RK point at $V/t = 1$ is not accessed directly by increasing the spin. Furthermore, we find that the presence of the unique 3-bond resonance t' widens the disordered region between the columnar and staggered phases by increasing dimer fluctuations, induces a 6-site plaquette phase at large t' , which is not present in QDMs derived from electron superexchange. The dimer-dimer correlations used to distinguish these phases are shown in Figs. 5.7 and 5.8. 104
- 5.7 Dimer-dimer correlations for three phases of the quantum dimer model on a 4×4 square lattice with periodic boundary conditions (Eq. 5.18 and Fig. 5.6). Reflection symmetry is utilized to enhance the readability of these correlations, by doubling the visual size of the lattice in each figure. (a) The “mixed” phase contains a linear superposition of the columnar and 4-site plaquette phases. (b) The physical state realized by using $f = 3$ atoms (^{52}Cr for example) contains weak correlations which fall off rapidly with distance, and we note good agreement with the numerical results shown in Fig. 5.4. (c) The RVB spin liquid phase is located at the RK point ($V/t = 1$ and $t' = 0$), and shows static correlations beyond nearest-neighbors, as all possible dimer coverings are present in the superposition. 105
- 5.8 Dimer-dimer correlations for the plaquette phases of the quantum dimer model on a 4×4 square lattice with periodic boundary conditions (Eq. 5.18). (a) Due to the presence of a non-zero 3-bond resonance ($t' \neq 0$) we find a 6-site plaquette phase, which is unique to the QDM as derived from whole-atom exchange. (b) The 4-site plaquette phase found with QDMs derived from electron superexchange is not found in our model, but is present as a component in the mixed phase. 106

List of Abbreviations

BZ	Brillouin zone
DDI	Dipole-dipole interactions
FT	Fourier transform
FQHE	Fractional quantum Hall effect
MF	Mean field
NMR	Nuclear magnetic resonance
OFR	Optical Feshbach resonance
QDM	Quantum dimer model
QSL	Quantum spin liquid
RK	Rokhsar and Kivelson point
RVB	Resonating valence bond
s-RVB	Short-ranged resonating valence bond
SHO	Simple harmonic oscillator
VBC	Valence bond crystal

Chapter 1: Introduction

1.1 The search for exotic magnetism

Progress in physics has been defined by the paradigm shifts undertaken to assimilate new and unexpected findings into our understanding of reality, and the field of condensed matter physics remains in the aftermath of such a shift. Traditionally, phases of matter and phase transitions have been understood by examining how the ordering of each phase breaks some symmetry of the underlying physical laws, following the methods of Landau [1]. However, upon the discovery of the Fractional Quantum Hall Effect (FQHE) in 2D electron gases [2, 3], it was observed that not all distinct quantum phases break a distinct symmetry, and thus elude a description with Landau theory. As FQHE systems were further investigated and modelled, it became clear that the community was exploring an entirely new type of condensed matter phase—one defined not by a broken symmetry, but by fractionalized excitations [4, 5], topological symmetry [6, 7], and emergent gauge degrees of freedom [8]. These surprising findings stimulated an overwhelming interest in the condensed matter community, and it was only a matter of time before new fractionalized and topological phases were being proposed and studied.

One of these proposed phases was the so-called resonating valence bond (RVB) ground state wave-function for a quantum antiferromagnet. These RVB phases—proposed by Anderson prior to the discovery of the FQHE [9], and inspired by Pauling’s work with resonating valence bonds [10]—were shown to possess topological order and fractionalized excitations [11, 12]. These discoveries, which were made

around the same time that Anderson was suggesting the pairing mechanism in high- T_C cuprate superconductors could be caused by proximity to the RVB phase [13], resulted in an explosion of interest over the following decades [14].

In the time since, these RVB states have been classified as members of a larger group of entangled magnetic ground states, known as quantum spin liquids (QSL). Broadly speaking, a QSL is the ground state of an insulating antiferromagnet in which large fluctuations of the spins between their quantized Zeeman sublevels prevent the onset of collective magnetic ordering down to zero temperature, and so retain the statistics of a liquid [15]. No symmetry is broken when the QSL phase is entered by cooling from the high-temperature paramagnetic phase, and so they cannot be described by conventional Landau Theory. As such, they possess hallmark properties of a “post-Landau” phase, including long-range entanglement [16, 17], fractionalized excitations [18–20], topological order [21–23], and emergent gauge dynamics [15, 24].

Strong numerical evidence suggests spin liquid ground states on several frustrated lattices [25, 26], but the experimental study of the QSLs has proved challenging. The list of spin liquid candidate materials has been growing [27], and increasingly detailed measurements have allowed for a better understanding of their material properties [28–30], but a “smoking gun” experiment by which to unambiguously identify QSL ground states has remained elusive [31–33]. This has in some ways caused a disconnect between theory and experiment, which has slowed progress in the field for decades. Although a plethora of possible QSL phases may be calculated theoretically, no single model has thus far accounted for the measured properties of current candidate materials.

One route towards breaking this deadlock requires improved accuracy of experimental probes, such as an increased energy resolution for inelastic neutron scattering, or a finer spatial resolution for SQUID-based microscopy. While extremely important to pursue, this route is straightforward conceptually, and one can imagine other novel

routes to be explored in the meantime. One such route involves finding candidate materials in which the microscopic Hamiltonian is known with certainty, leading to a more direct interpretation of the measured data. This thesis embarks on this latter route, and explores the possibility of finding QSL physics in new condensed matter systems.

Finding new spin liquid candidates amounts to finding systems with sufficiently large quantum spin fluctuations. To achieve large fluctuations between Zeeman sub-levels in a solid-state system—where electron hopping mediates the magnetic exchange interactions—one must restrict the search to low-dimensional, geometrically-frustrated, spin-1/2 antiferromagnets [25, 31, 34–37]. These frustrated antiferromagnets possess competing interactions which cannot be simultaneously satisfied, resulting in a large classical degeneracy of their ground state [38–41]. Large spin fluctuations may then melt the magnetic order, and drive the systems towards the spin liquid phase.

Despite knowing what is required of candidate materials, many challenges remain. Firstly, not all materials with spin-1/2 moments on a classically frustrated lattice are guaranteed to possess QSL ground states. Furthermore, materials which do are often structurally complex, and the presence of interlayer coupling, anisotropic exchange interactions, and disordered magnetic moments, make it difficult to develop accurate microscopic models by which to explain scattering and thermodynamics measurements. Therefore, in this thesis we specifically seek systems for which the interaction Hamiltonian may be determined with relative certainty, and which possess a QSL phase somewhere on their phase diagram.

Quantum dimer models (QDM) are one such example of a microscopic model which can produce QSL ground states. QDMs describe the dynamics of close-packed hard-core dimers on a lattice, and have received continued attention since their original proposal by Rokhsar and Kivelson in 1988 [42]. Exotic physics emerges in these

systems from the interplay between quantum fluctuations, hard-core constraints, lattice geometry, and system topology. Their rich phase diagram contains a short-ranged version of Anderson’s RVB spin liquid, as well as conventional symmetry-broken phases known as valence bond crystals (VBC) [43]. As a type of QSL, the RVB phase exhibits all of the desired properties—topological order and fractionalized excitations [12, 44, 45], emergent gauge dynamics [43, 46, 47], and quantum critical points [48–50]. Furthermore, the creation and manipulation of a QDM would be a major step forward in the quest for topologically protected quantum computing, due to its close relation with Kitaev spin liquids [33, 51–53]. Unfortunately again, there are no clear-cut examples of materials governed solely by a QDM Hamiltonian, and so we must look in new places to find clean physical realizations of this model.

Systems of cold atomic gases loaded into optical lattices may provide the alternate route to experimentally observing the quantum dimer models and spin liquid phases that we seek. Experiments with ultracold atoms, as they are often called, offer unprecedented levels of tunability and control over lattice parameters and particle-particle interactions, and have repeatedly proven their effectiveness as quantum simulators of condensed matter models and phases [54–56]. The experimental demonstration of atomic Mott insulators and their associated Hubbard models [57–60], and the growing capability to control and probe the magnetic interactions [61–64], has opened the door for the study of magnetic ground states using ultracold atoms.

In particular, when an atomic gas is cooled near absolute zero and confined with an array of lasers—a so-called optical lattice—the spin degree of freedom remains unfrozen [65, 66] and the low-energy spin interactions are manifest as a virtual exchange of whole atoms between lattice sites [62, 67]. Counter-intuitively, this whole-atom exchange produces fluctuations which increase with the atomic hyperfine spin f [68], in dramatic contrast to solid-state systems, where fluctuations are suppressed and classical ordering occurs for large spin moments. This peculiar behavior of ultracold

atoms may allow large- f Mott insulators to exhibit exotic magnetic phases traditionally associated with low-spin materials, including atomic spin liquids. In fact, crystallized dimer phases [69–72], resonating plaquette phases [73–76], and dimer liquid phases [77–82]—all hallmarks of the QDM—have been studied theoretically for large- N $SU(N)$ and dipolar quantum gases [83, 84]. However, these previous studies have largely considered ways by which to simulate quantum dimer physics, and to engineer systems such that the relevant degrees of freedom may be mapped to a QDM. Therefore, determining how terms in the microscopic QDM Hamiltonian depend on physical parameters, and determining which regions of the phase diagram are physically accessible, are open questions which we address thoroughly in this thesis.

1.2 Thesis description

This thesis details a proposal for using of large-spin ultracold atoms to engineer and observe exotic magnetic phases, such as quantum spin liquids, and ground states of the quantum dimer model including ordered valence bond crystals (VBC). We believe that by fundamentally broadening the search in this way, we may bypass several persistent difficulties. Specifically, the microscopic Hamiltonian for a cold atom system can be determined more directly than in the solid state, and so we may model a QDM with a high degree accuracy. We may then determine the physically accessible regions of the phase diagram, and investigate whether a QSL ground states could someday be observed experimentally using ultracold atoms.

As discussed in the following chapters, the study presented in this thesis is unique in many ways. We find evidence for exotic magnetism without requiring enhanced symmetry, geometrical frustration, or a mapping from an equivalent Hamiltonian. Instead, we find that the naturally occurring whole-atom exchange interaction—which is fundamentally different than electron superexchange in a solids, due to the presence

higher-order Heisenberg couplings—allows sufficiently large quantum spin fluctuations to melt the order and produce a genuine spin liquid phase. All that is required are large-spin atoms and the assistance of an optical Feshbach resonance—a widely used method of tuning particle-particle interactions in systems of ultracold atoms.

Another important aspect of this work is the explicit calculation of a quantum dimer model for ultracold atoms. Not only does our work provide a rigorous perturbative expansion of the QDM in terms a physically small parameter, but in doing so, we uncover a second-order kinetic term unique to this system. This term favors disorder and pushes the system towards a liquid ground state. For these reasons, we firmly believe the results presented in this thesis provide strong evidence that the quantum dimer model and resonating valence bond regions of its phase diagram could be observed for the first time in their purest form using large-spin ultracold atoms.

1.3 Thesis overview

This thesis is organized as follows. Chapter 2 reviews the background physics of quantum magnetism in many-body systems, and provides a description of quantum spin liquids and the phases accessible to quantum dimer models. The history of observing exotic phases of matter with ultracold atoms is reviewed, and their potential for investigating entangled magnetic phases is discussed. Chapter 3 begins with the derivation of the microscopic Hamiltonian for a gas of bosonic atoms in a 2-dimensional optical lattice. A protocol for tuning the interactions via optical Feshbach resonance is then presented, and estimates of relevant energy scales and required experimental parameters are calculated to ensure the validity of our proposal. Chapter 3 is then concluded with a determination of the ground state phase diagram for the microscopic Hamiltonian using the conventional spinor mean field theory, for which nematic and antiferromagnetic phases are found.

Chapters 4 and 5 present the major contributions of this thesis—the broadening of the search for quantum spin liquids and a rigorous derivation of the quantum dimer models for ultracold atoms. Chapter 4 begins by developing a mean field (MF) theory for bosons in an optical lattice. A spin liquid phase is found to be a competitive ground state to the spin nematic and antiferromagnetic states for large spin and interaction strength, and spin fluctuations are shown to be a maximum in this region. The chapter is concluded when the mean field QSL wavefunction is shown to take the form of a short-range RVB state when projected to the one-particle-per-site Hilbert space. This motivates the reformulation of the microscopic Hamiltonian in the form of a quantum dimer model, which is the subject of Chapter 5. This chapter begins with a discussion of the dimer Hilbert space, and is followed by a rigorous application of Rayleigh-Schrödinger perturbation theory to derive an effective QDM for ultracold bosonic atoms. Results from this perturbation expansion are compared with numerical results which we perform on the unperturbed Hamiltonian. The phase diagram is then calculated, and the physically accessible region of the parameter space is identified. Finally, Chapter 6 concludes this work by reviewing its prominent contributions, and discusses this work in the context of the greater search for exotic magnetic phases.

Chapter 2: Quantum Magnetism and Ultracold Atoms

2.1 Magnetic phases in solid state systems

2.1.1 The Hubbard and Heisenberg models

We may begin to understand low-energy physics of materials by considering the Hubbard model, which serves as a common starting point for the study of electrons in periodic potentials [85, 86]. This model was developed to describe the transition from metallic behavior—where electrons are free to move about the lattice due and electron-electron interactions are small—to the Mott insulating state—where electrons are localized at particular lattice sites due to strong electron-electron interactions. This model also describes common band insulators, in which the conductivity is determined by the filling fraction, and the presence of a band gap between the valence and conduction bands, as shown in Fig. 2.1. While our search for exotic magnetism does require insulating materials, band insulators do not possess magnetic ordering in the ground state, and so we restrict ourselves throughout this work to Mott insulators with one-particle-per-site.

The Hubbard model is typically expressed as

$$H = -t \sum_{\langle i,j \rangle, \sigma} (\hat{c}_{i\sigma}^\dagger \hat{c}_{j\sigma} + \text{H.c.}) + U \sum_i \hat{n}_{i\uparrow} \hat{n}_{i\downarrow}, \quad (2.1)$$

where $\hat{c}_{i\sigma}^\dagger/\hat{c}_{i\sigma}$ are creation/annihilation operators for electrons at lattice site i and with

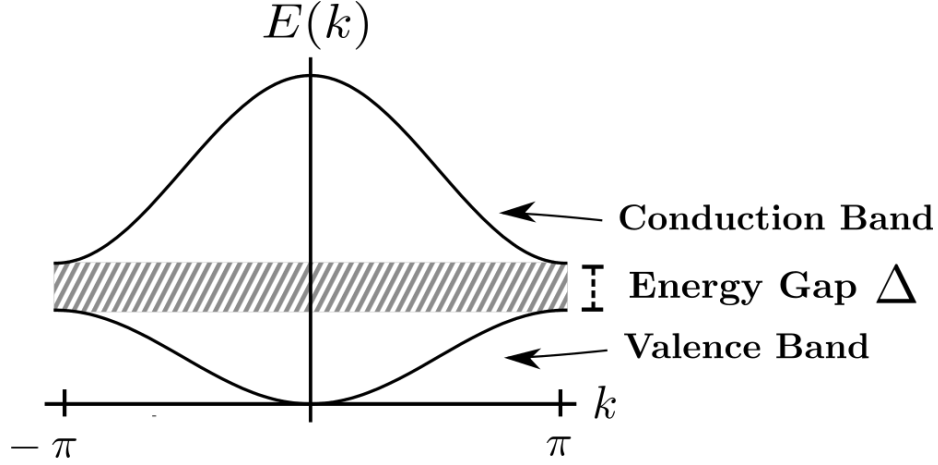


Figure 2.1: The band structure of weakly interacting electrons in a 1-dimensional periodic potential. The band gap Δ characterizes the minimum energy needed to excite an electron from the valence band to the conduction band. The Pauli Exclusion principle dictates that no two fermions can occupy a single-particle state simultaneously. Therefore, the electronic ground state is found by filling up available energy states from low to high, resulting in a Fermi surface. This is in contrast to the ground state of bosonic systems in which all of the bosons may occupy the lowest-energy state simultaneously, and Bose-Einstein condensation may occur.

spin $\sigma = \{\uparrow, \downarrow\}$, while $\hat{n}_{i,\sigma} = \hat{c}_{i\sigma}^\dagger \hat{c}_{i\sigma}$ is the number operator which simply counts the number of electrons on lattice site i . The first term—parametrized by t —represents the kinetic energy of electrons hopping between nearest-neighbor sites, while the second term—parametrized by U —accounts for the potential energy of interaction between two electrons on the same site, as shown in Fig. 2.2. In the weakly interacting limit ($U/t \ll 1$), one recovers the physics of nearly free electrons in a periodic potential, with energy bands corresponding to the different Bloch states. In the one-particle-per-site strongly interacting limit ($U/t \gg 1$), one obtains the physics of a Mott insulator, where strong electronic repulsion prevents transport of electrons through the lattice.

In the Mott insulating regime, we may neglect hopping and treat the electrons as fixed spins on a lattice. We then reintroduce hopping as a weak perturbation, and one obtains the antiferromagnetic Heisenberg model [87]. In this model, the electrons'

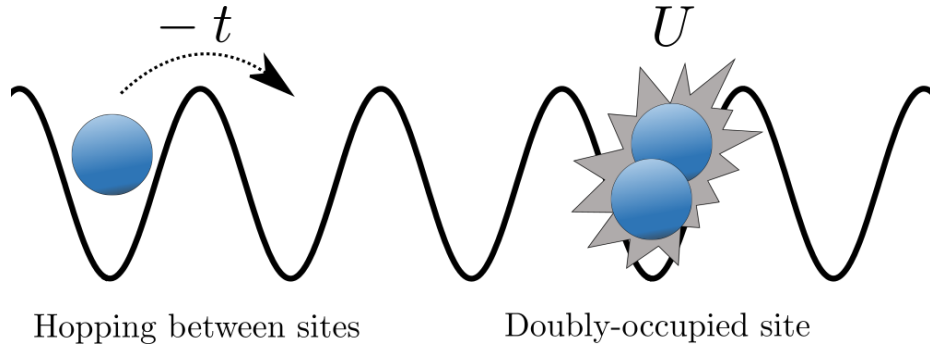


Figure 2.2: A pictorial representation of the Hubbard Model, where blue circles represent electrons, and the black solid line represents the underlying lattice potential. When an electron hops from one lattice site to another, the energy is reduced by t . If any site is doubly occupied, then the energy is increased by U . The ground state for $t \gg U$ is that of a band metal, where metallic or insulating behavior come from a filled valence band and a gap to the conduction band, as shown in Fig. 2.1. For $U \gg t$ the strong repulsive interactions quench the kinetic energy, and for one particle per site the system becomes a Mott insulator.

kinetic degrees of freedom remain frozen, so the dynamics are controlled by the spin magnetic moment on each site. This spin could be that of a single valence electron, a combination of several electrons, or could include the nuclear spin. In these cases, virtual hopping processes allow spin-exchange interactions between different sites of the lattice. This may be written as

$$H = \frac{1}{2} \sum_{i,j} J_{ij} \hat{\mathbf{S}}_i \cdot \hat{\mathbf{S}}_j, \quad (2.2)$$

where $\hat{\mathbf{S}}_i$ denotes the spin operator for the spin on site i . Here, J_{ij} measures the strength of the interaction between the spins on i^{th} and j^{th} sites. The ground state properties of this Hamiltonian will depend on strongly on the geometry of the lattice and the nature of the couplings $J_{i,j}$. While the solution of this problem is well understood for simple lattices and interactions, studying this model on so-called “geometrically frustrated” lattices leads to much richer and more exotic phases, as described in Subsec. 2.2.1 to follow.

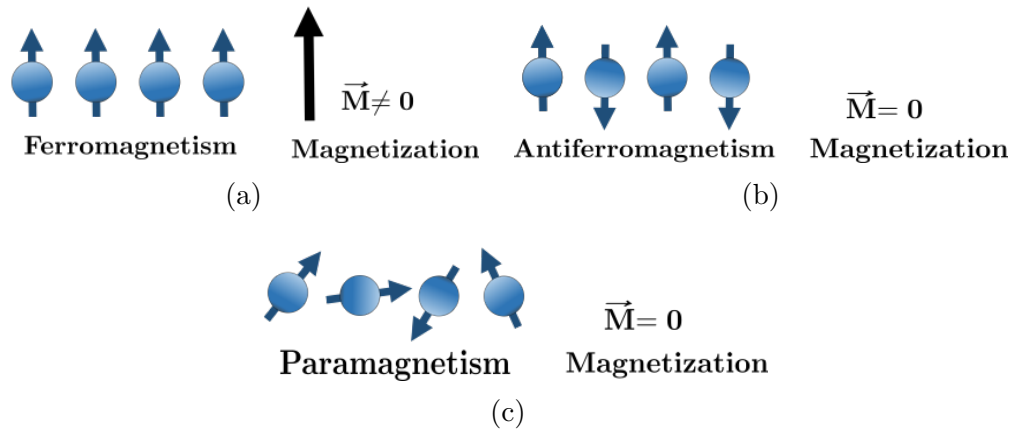


Figure 2.3: Three classical magnetic orders. (a) Ferromagnetism is responsible for macroscopically magnetic materials, such as iron bar magnets. (b) Antiferromagnetism is a magnetic ordering with zero macroscopic magnetization, and is found in many transition metal oxides. (c) Paramagnetism has no magnetic order, and the spins only align in response to an external applied field. Most chemical elements are paramagnetic, and both ferromagnetic and antiferromagnetic materials are paramagnetic at high temperatures.

2.1.2 Classical spin orders

For simple lattice geometries the Heisenberg model can be solved with a mean field theory, and one finds the three of the major types of classical magnetic ordering—ferromagnetism, antiferromagnetism, and paramagnetism—as depicted in Fig. 2.3. Mean field theory was developed by Pierre Curie and Pierre Weiss [88] during early studies of magnetism, where they used it to describe the magnetic susceptibility of ferromagnets in the paramagnetic phase above the transition temperature to the magnetically ordered state. At high temperatures, both ferromagnetic and antiferromagnetic materials behave as paramagnets, with random orientation of spin moments and no macroscopic magnetization. However, upon cooling below the critical temperature, spontaneous magnetic ordering occurs.

The paramagnetic-magnetic phase transition can be observed by measuring the material’s magnetic susceptibility, $\chi = \partial M / \partial B$, which characterizes the change in the material’s magnetization with respect to changes in an external magnetic field,

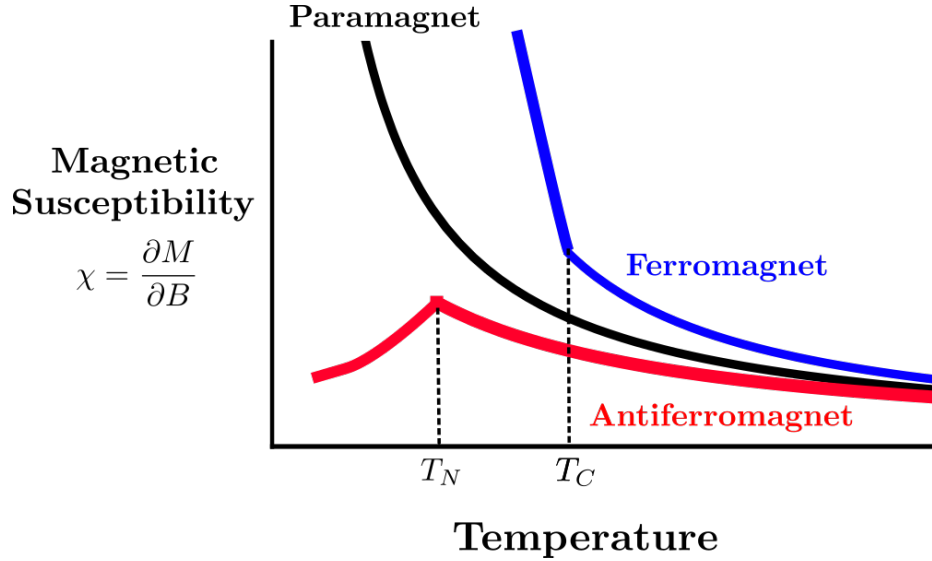


Figure 2.4: Magnetic susceptibility for the classical magnetic orders. The susceptibility characterizes the material’s response to changes in the external magnetic field. Both ferromagnetic and antiferromagnetic materials behave like paramagnets at high temperatures. Ferromagnets develop magnetic order below their Curie Temperature T_C , while antiferromagnets become ordered below their Néel Temperature, T_N .

as shown in Fig. 2.4. The behavior of the χ in the paramagnetic regime can be described by what is known as the Curie-Weiss Law, and is given by

$$\chi = \frac{C}{T - \Theta}, \quad (2.3)$$

where C is the Curie constant, T is the temperature, and Θ is the Curie temperature or critical temperature of the phase transition (also written as T_C for ferromagnets). Then, by fitting the inverse susceptibility at high temperature to the Curie-Weiss Law, one determines the nature of the magnetic interactions in the material, which is shown in Fig. 2.5. Materials with ferromagnetic interactions have a Curie temperature $\Theta > 0$, while antiferromagnetic materials have $\Theta < 0$.

A fundamental characteristic of ferromagnetic and antiferromagnetic orders is that they break spin-rotational symmetry, despite the fact that the spin-spin interactions of the Heisenberg model (Eq. 2.2) are symmetric (unchanged) under spin rotations. In the paramagnetic phase, thermal fluctuations result in a ground state which pre-

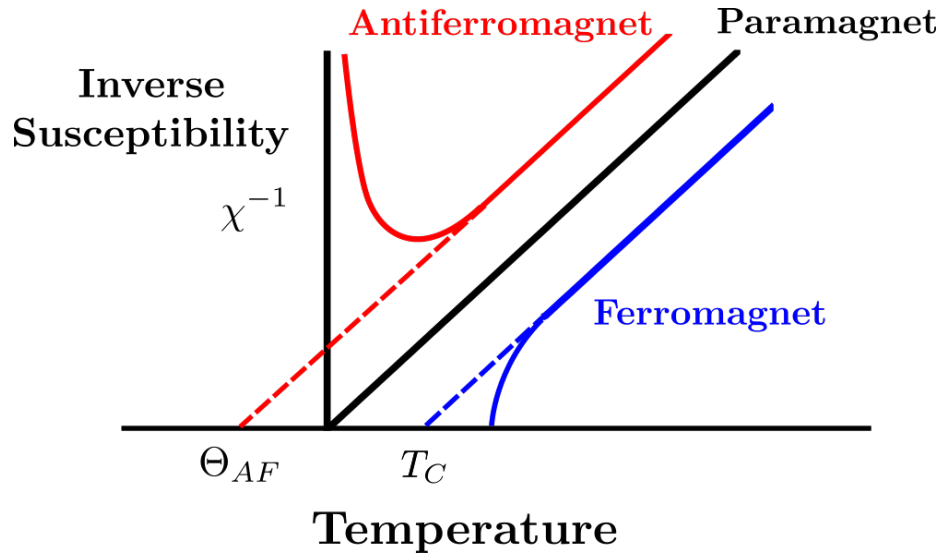


Figure 2.5: The inverse magnetic susceptibility as a function of temperature. The inverse susceptibility is useful for determining the sign of a material’s spin-exchange interactions, and therefore whether one expects a low-temperature ferromagnet or antiferromagnet. This is done by extrapolating the high-temperature behavior—which follows the Curie-Weiss Law ($\chi^{-1} \propto T - \Theta$)—to the temperature axis to determine the Curie-Weiss temperature. Paramagnets intercept at $T = 0$, while ferromagnets have a positive Curie-Weiss Temperature T_C . Antiferromagnetic materials will have a negative Curie-Weiss Temperature Θ_{AF} . This is an important measurement in the determination of spin liquid candidates, as several materials show antiferromagnetic exchange interactions from their inverse susceptibility, but show no signs of magnetic ordering several orders of magnitude below their expected phase transition around $|\theta_{AF}|$.

serves the spin-rotational symmetry of the underlying interactions. However, below the transition temperatures, fluctuations are decreased, and the spin-rotational symmetry is spontaneously broken when the spin moments point along some specific axis. Phase transitions into and out of these magnetically ordered phases are described by Landau’s Theory of Phase Transitions, since the different states are defined by their different symmetries.

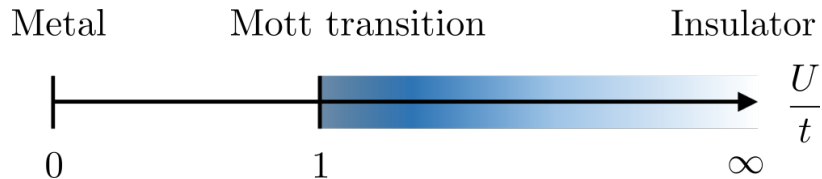


Figure 2.6: A schematic phase diagram of the Hubbard Model. Tuning the ratio of the potential and kinetic energy U/t , the system passes from metal to insulator in what is known as the Mott transition. In the intermediate regime ($U/t \sim 1$), strong virtual hopping increases the charge and spin fluctuations. The enhanced spin fluctuations in this region can “melt” the classical spin ordering on geometrically frustrated lattices.

2.2 Quantum dimer models and quantum spin liquids

2.2.1 Frustrated interactions and spin fluctuations

In many-body spin systems at low temperatures, quantum fluctuations of the spin moments play a significant role in determining the nature of the magnetic ground state. Classical and mean field approximations treat the quantum mechanical spins as classical magnetic moment vectors. To introduce fluctuations around the MF ground state the spin operators $\hat{\mathbf{S}}_i$ may be written in a bosonic representation, known as Holstein-Primakoff bosons [89], which are expanded as a power series in $1/S$, and diagonalized via a Bogoliubov transformation [87, 90]. In the large spin limit ($S \gg 0$), spin fluctuations around the MF ordering are sufficiently captured by this approximation, and the spins indeed behave like classical vectors. For certain systems however, quantum spin fluctuations radically change the ground state of Eq. 2.2. This is particularly the case when systems are close to the Mott-insulator transition (Fig. 2.6) and for geometrically frustrated lattices.

Geometrical frustration occurs on lattices which contain “triangular-motifs” [31], including triangular, kagome, and hyper-kagome lattices. On these lattices, spins can-

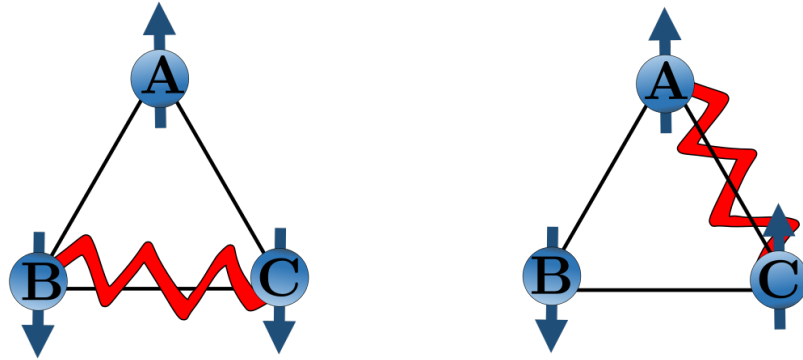


Figure 2.7: Geometrical frustration of Ising spins on a triangle. For antiferromagnetic interactions, each spin tries to align anti-parallel to its neighbors. For Ising spins constrained to point up or down along one axis on a triangular lattice, it is impossible to meet this criteria simultaneously for each spin, and so there may be a large number of degenerate “next-best” arrangements. Since the system cannot reach its ideal configuration, it is said to be frustrated. Spin fluctuations are increased by the presence of geometrical frustration.

not minimize their energy through any single ordering pattern [15]. Classically, this may result in a number of degenerate states corresponding to equal energy configurations of local spins. A simple example of geometrical frustration is shown in Fig. 2.7, for Ising spins with antiferromagnetic interactions on a triangular lattice. The idea is that Ising spins which reside on the corners of a triangle cannot simultaneously minimize their energy by pointing in opposite directions of each other, as desired by their local antiferromagnetic interaction. This results in frustration, as spin configurations which minimize the energy locally often do not minimize the energy globally. The system therefore possesses a highly degenerate ground state, due to many possible next-best arrangements of the spins locally. When a system of spins is geometrically frustrated, spin fluctuations tend to kick the system around between the degenerate configurations, resulting in highly disordered spin states.

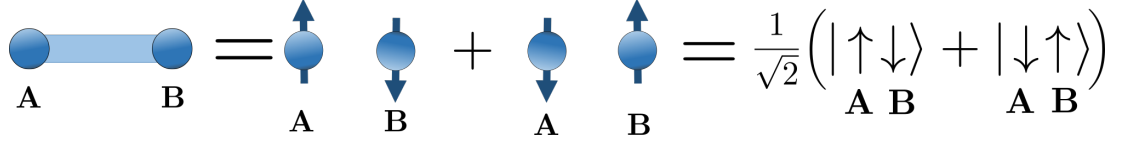


Figure 2.8: Example of the pictorial dimer representation used throughout this work. The two circles represent particles on sites A and B, and the solid line connecting them indicates that these spins are in a singlet state, or dimer. A singlet state consists of two quantum spins in a superposition of up and down states, resulting in a total spin moment of zero.

2.2.2 Valence bond crystals and the quantum dimer model

Valence bond solids, or valence bond crystals (VBC), have spins on neighboring sites which pair-off to form spin-singlet pairs with a total $S = 0$. When these singlet pairs exist on a lattice, they are also known as dimers, and are described pictorially and mathematically in Fig. 2.8. This pairing originates from the fact that each term in the antiferromagnetic Heisenberg model, which takes the form $\hat{\mathbf{S}}_1 \cdot \hat{\mathbf{S}}_1$, may be solved by moving from the basis of individual spins 1 and 2, to basis states constructed from the total angular momentum basis. A dimerized ground state of a Heisenberg spin system attempts to minimize the energy by minimizing the energy locally, and the system will be tessellated by these dimers, as shown in Fig. 2.9. This is related to the so-called domino tiling of a region, and the number of unique dimer patterns has been calculated exactly by the method of Pfaffians [91, 92].

The dynamics of a valence bond state are governed by a type of Hamiltonian called a quantum dimer model (e.g. [46, 93]). A typical QDM for a square lattice would be written as,

$$\hat{H}_{\text{QDM}} = \sum_{\text{plaquettes}} \left[-t \left(\left| \begin{array}{c} \text{---} \\ \text{---} \end{array} \right\rangle \langle \text{||} | + \text{H.c.} \right) + V \left(\left| \begin{array}{c} \text{---} \\ \text{---} \end{array} \right\rangle \langle \text{---} | + \left| \text{||} \right\rangle \langle \text{||} | \right) \right]. \quad (2.4)$$

This description captures the dynamics of the valence bond state through a kinetic term parametrized by t , and a potential term of parametrized by V . The underlying

Dimer covering on a square lattice

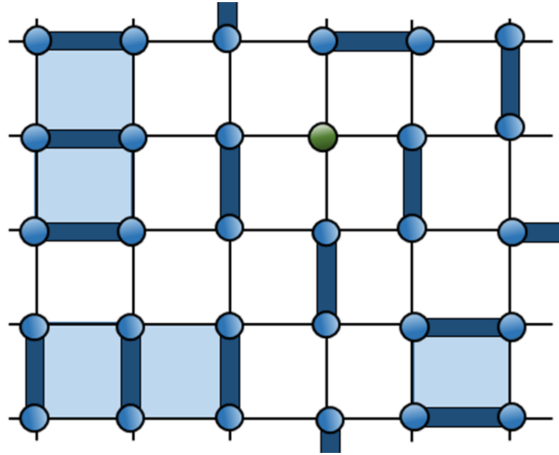


Figure 2.9: An example of a dimer covering on a square lattice. Shaded blue squares represent flippable plaquettes, in which the dimers may rearrange locally. Dimers on non-flippable plaquettes require non-local rearrangements in the form of closed loops. Defects where an atom is not paired to any dimer, known as a spinon, are fundamental excitations of this system.

one-particle-per-site constraints result in hardcore, non-overlapping dimers, such that no spins exist in multiple dimer pairs simultaneously. Therefore, all dimer motion must involve rearrangements of neighboring pairs called flippable plaquettes, as shown in Fig. 2.9, or longer chains called flippable loops. Meanwhile, the potential energy term represents an effective repulsion of dimers, and prefers configurations which minimize the number of flippable plaquettes.

There are three main categories of VBC/dimer phase: columnar, plaquette/mixed, and staggered, which are shown in Fig. 2.10. The columnar phase is built from repeating columns (or rows) of parallel bonds, and is favored when the kinetic energy is large ($V/t \ll 1$). In the plaquette phase, dimer bonds resonate between different configurations inside a multi-site unit cell, such as the vertical and horizontal configurations of two bonds around a flippable plaquette on a square lattice. Plaquette phases on a triangular and kagome lattices have resonances of larger sizes. The mixed phase is simply a plaquette phase with an unequal superposition of the different dimer

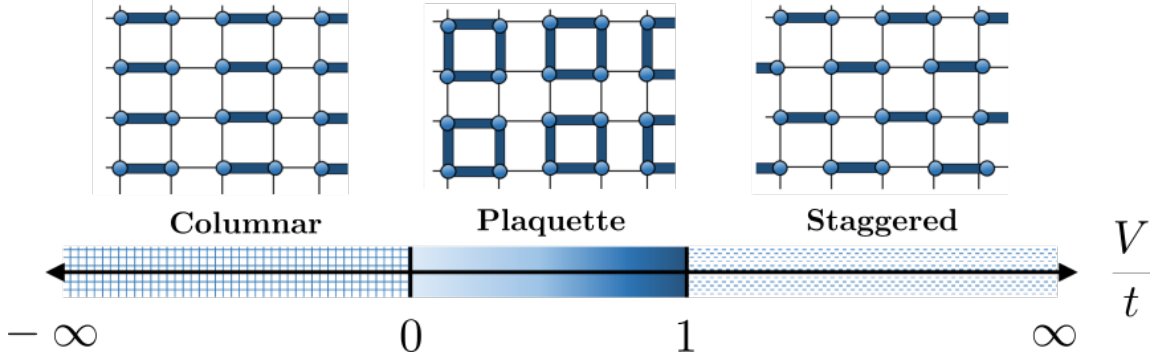


Figure 2.10: Three phases of the quantum dimer model on a square lattice, which are encountered as the ratio of potential-to-kinetic energy (V/t) is varied. When the potential energy is negative ($V/t < 0$), the system will attempt to maximize the number of flippable plaquettes, resulting in the columnar phase. For $0 < V/t < 1$ the terms are comparable, and the plaquette phase emerges. The point $V/t = 1$ is a special point, known as the RK point, where the system behaves as a s-RVB spin liquid (described in Sec. 2.2.3). For all values of $V/t > 1$, the staggered phase, in which there are no flippable plaquettes, is the exact ground state.

patterns in resonance. Finally, the staggered phase is such that there are no flippable plaquettes, and is an exact eigenstate of this model when the potential is greater than the kinetic term ($V/t > 1$).

2.2.3 Quantum spin liquids

A spin liquid is a Mott insulator with antiferromagnetic exchange interactions, which resists magnetic order all the way down to absolute zero temperature. Here “liquid” implies an analogy with the common solid-liquid phase transition, where a disordered liquid freezes into an ordered solid at low temperature. Since the disordered spins of a spin liquid never freeze into a magnetically ordered phase, the spins are said to remain a liquid. However, the liquid description only applies to the orientations of the spins, not their physical location in the lattice, and the system remains a one-particle-per-site Mott insulator.

To achieve a spin liquid ground state, it is necessary to have large spin fluctuations. These fluctuations effectively melt the long-range Néel order that would appear in the

ground state of antiferromagnets. Spin uncertainty is largest for small magnitudes of the spin, and in solid state systems, spin liquid candidate materials are those whose magnetism is governed by the behavior of a single spin- $1/2$ electrons on each site. These spin fluctuations are enhanced further by geometrical frustration, and when quantum fluctuations are included, geometrically frustrated systems may become spin liquids.

A particularly important class of QSL are known as resonating valence bond states (RVB). Historically, these states were introduced in an attempt to understand the pairing mechanism of cuprate superconductors [9, 13, 14], specifically the phase diagram of hole-doped La_2CuO_4 . An RVB state consists of an equal superposition of the equal energy valence bond coverings of the lattice. In this way, it can be thought of as a superposition of spin singlet coverings, which are themselves spin superpositions. This results in a highly entangled ground state, which no longer breaks rotational symmetry of the lattice. Anderson's idea was that when a QSL is hole-doped by introducing empty sites into the Mott insulating state, the entangled electron pairs will become mobile and become superconducting. If the valence bond patterns of an RVB spin liquid consist of only nearest-neighbor dimer pairs, the system may be described by a QDM (Eq. 2.4), where depending on the lattice, the RVB QSL phase occurs at or in the vicinity of the Rokhsar-Kivelson Point ($v/t = 1$). While Anderson's RVB has failed to accurately describe cuprate superconductors, the theoretical connections between RVB spin liquids and exotic entangled states has remained a driving force behind the investigation into spin liquid phases [14].

2.2.4 Fundamental excitations of VBCs and QSLs

A major difference between the antiferromagnetic Néel-ordered state and the QSL state, is the nature of their low energy excitations [16, 90]. Néel states break the $SU(2)$ spin rotational symmetry of the Heisenberg model (Eq. 2.2), and therefore possess

a low-energy hydrodynamic mode associated with the broken symmetry, following from Goldstone's theorem [94]. The Goldstone modes for the Néel state are long-wavelength spin waves, which when quantized are called magnons, and are spin-1 bosonic excitations. Furthermore, the energy spectrum of these excitations is gapless, and so they may be created with arbitrarily low energy.

When considering valence bond crystal states with only nearest-neighbor dimers, the chosen dimer pattern breaks the rotational symmetry of the lattice, and so there exist a set of degenerate equal-energy configurations corresponding to different rotations of each possible covering pattern [95]. The fundamental excitations of this system are those by which a singlet bond ($S = 0$) is promoted to a triplet bond ($S = 1$), by changing the orientation state of one of the composite spins [15]. The triplet state exists at a finite energy above the singlet state, and so the energy spectrum for a VBC is gapped. We can equivalently view this energy gap as the amount of energy required to create two spinons.

In a VBC, spinons are confined and thus cannot be observed as isolated excitations. As two spinons migrate away from each other, they leave a string of distorted dimers connecting them, as depicted in Fig. 2.11. These distortions break the background dimer order, and cost energy for each dimer that is distorted. Therefore, when two spinons are separated, they experience an effective potential which increases linearly with the separation distance. At some critical distance it becomes energetically favorable to release the energy store in the dimers, and create two new spinons to pair each of the separated pair. Therefore, spinons are not found as isolated excitations in these system, and they are said to be confined. This confinement of the spinons is a direct result of the ordered dimer background, and the means that the fundamental excitations of the VBC are the spin-1 triplets [95].

For a QSL on the other hand, the spinons are not confined, as described in Fig. 2.12. As two spinons move apart, only dimers local to each spinon are disrupted, and

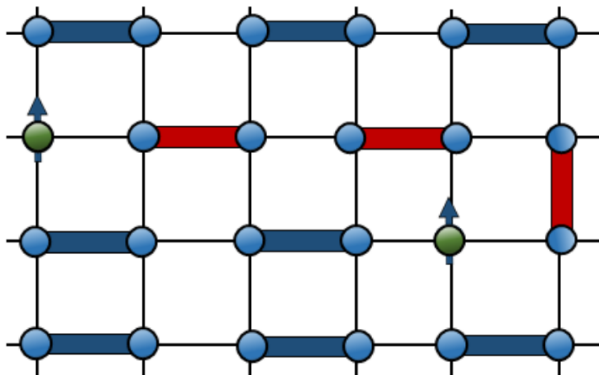


Figure 2.11: Spinon confinement in a columnar VBC phase on a square lattice. Two spinons are created in pairs by breaking a nearest-neighbor singlet dimer, with some energy Δ . As one spinon moves away from its original location, it leaves behind a string of dimers which are distorted from the original columnar configuration (shown in red). If each unfavorable bond costs some energy ϵ , the energy to move the spinons a distance d apart grows as ϵd . When the energy of their separation costs more than the energy to create two new pairs ($\epsilon d > 2\Delta$), new spinons will be created at the ends of the string, resulting in a system which only has nearest-neighbor spinon pairs. This limiting of the possible separation distance is known as confinement.

so there is no linear potential associated with their separation. These spinons may be found as isolated, fractionalized, spin-1/2 excitations, since they have a quantum number of one-half the fundamental triplet excitation in the VBC.

2.2.5 The experimental search for quantum spin liquids

Despite a large body of theoretical work, the experimental identification of true two-dimensional spin liquid materials has proven challenging. Firstly, the materials need to be Mott insulators which possess localized spin-1/2 moments, interacting through antiferromagnetic exchange interactions. Additionally, geometrically frustrated lattices are required to maximize spin fluctuations and uncertainty. The material must also exhibit no magnetic ordering at any temperature, which is equivalent to observing paramagnetic behavior at all temperatures. This can be determined from magnetic susceptibility measurements, as shown in Figs. 2.4 and 2.5. Once a material meets these requirements, it may be considered a spin liquid candidate material.

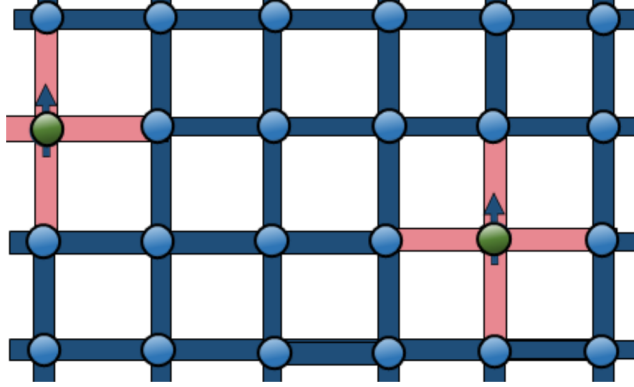


Figure 2.12: Spinon deconfinement in a RVB spin liquid. To break a dimer and create a spinon pair requires some energy Δ . However, as each spinon is moved apart, they distort only the 4 bonds adjacent to themselves, limiting the energy needed for separation. Since there is no upper bound to the distance d at which they are found as isolated particles, they are said to be deconfined. Each lone spinon is considered a fractionalized excitation, in that they have a quantum number ($s = 1/2$) which is a fraction of the quantum number of the “unfractionalized” triplet excitation ($s = 1$).

When a spin liquid candidate material is found, there are several ways to experimentally study its properties. Neutron scattering experiments provide a way to probe the spin-spin correlations and excitations of a material, magnetic heat capacity measurements provide information about the low-energy density of states, and both NMR and muon resonance spectroscopy (μ RS) provide information about local spin moments in the material. Together, these different experiments paint a good picture of the spin liquid candidate, but there is still no single experiment which unequivocally determines a spin liquid phase [31]. Comparison of neutron scattering data for Herbertsmithite [28], a spin- $1/2$ Mott insulator with a kagome lattice, with the spectrum obtained from a Z_2 spin liquid [19], provides compelling evidence for the presence of a QSL state in at least one candidate material. However, for all the effort that has been spent studying and characterizing spin liquid candidate materials, the number of systems being studied remains quite small.

2.3 Exotic magnetic phases with ultracold atoms

The field known as ultracold atoms, or cold atoms, has a history of experimentally verifying predictions of condensed matter physics, and so one may expect that experiments with cold atomic gases could provide a way to study exotic magnetic states, such as quantum spin liquids and valence bond crystals. This history begins with the creation of a Bose-Einstein condensate (BEC) with bosonic rubidium atoms (possessing integer spin $f = 1, 2, 3 \dots$) in a magneto-optical trap. The existence of this phase of matter was proposed by Einstein 1925 when applying Satyendra Nath Bose's quantum statistics of light to a gas of atoms with integer spin. It was predicted that such a gas would undergo a phase transition into a state with a macroscopically large fraction of atoms in the lowest energy state, as shown in Fig. 2.13. This theory proved successful in describing the superfluid properties of Helium-4, but it was over 75 years before Einstein's idea of a condensed bose gas was observed in a lab.

Advancements in the laser cooling and trapping of neutral atoms allowed for the cooling of an isolated gas of atoms to record low temperatures [96, 97], and BECs were observed with rubidium vapor [98], sodium [99], and lithium gases [100] soon after. In these experiments a cloud of rubidium vapor was held in a magnetic trap and cooled using a combination of laser cooling and evaporative cooling, to a temperature of about 170 nK. By analyzing the momentum distribution of the particles (Fig. 2.14) and calculating the fraction of particles in the ground state (Fig. 2.13), they determined that a Bose-Einstein condensate had formed. More recently, BECs of larger atoms such as Chromium [101] and Dysprosium [102] have been created, and the list continues to grow. While there are now a multitude of phases and phenomena being investigated with cold atomic gases, there is no doubt that its birth from a clear and stunning observation of Bose-Einstein statistics quickly put the field of ultracold atoms on the map.

Order Parameter for BEC Phase Transition

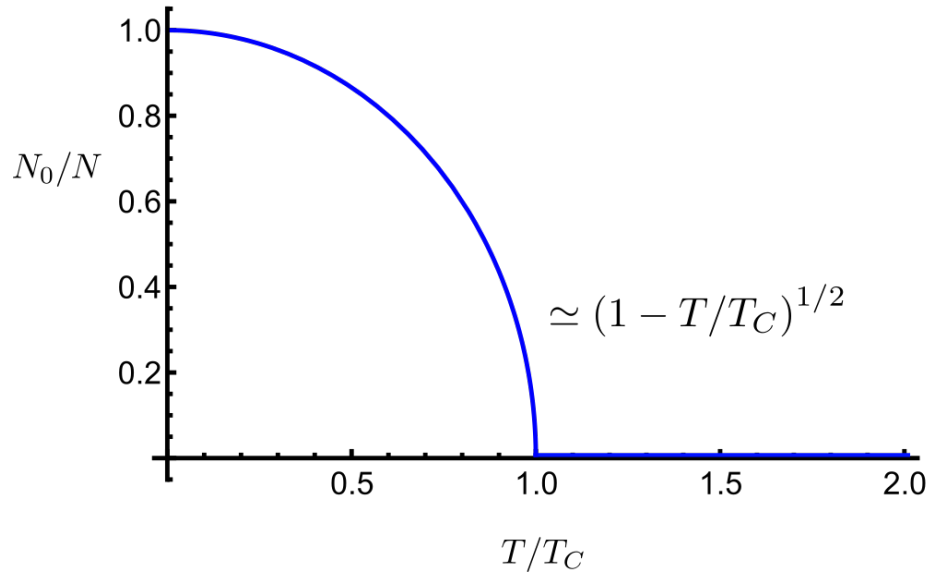


Figure 2.13: The fractional occupation of the single-particle ground state, N_0/N . This quantity serves as the order parameter for the phase transition from a gas to a Bose-Einstein condensate. This second-order transition occurs at the critical temperature $T = T_C$, and in the vicinity of T_C this quantity takes the form $N_0/N \simeq (1 - T/T_C)^\epsilon$, where the critical exponent $\epsilon = 1/2$.

Momentum distribution above and below T_C

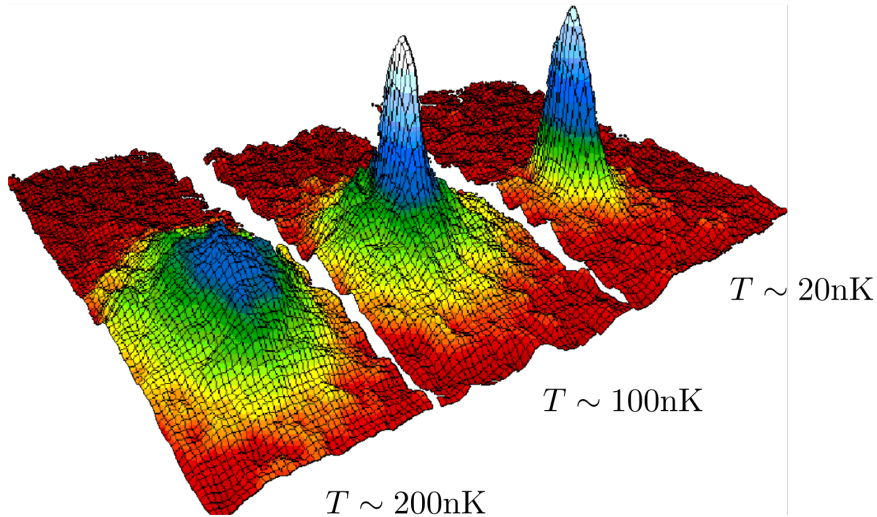


Figure 2.14: The momentum distribution of a Bose-Einstein condensate, above and below the transition temperature. As the temperature is lowered below T_C , macroscopic occupation of the lowest momentum state occurs. This results in a sharp peak at the center of the momentum distribution, and is evidence of the growing occupation of the ground state.

2.3.1 Optical lattices

The first cold atom experiments used magnetic fields from sets of Helmholtz coils to create the magnetic field gradients needed to spatially trap the electrically neutral atoms. A drawback of these magnetic traps is that magnetic field induces a Zeeman splitting between of the degenerate spin states, and so the trapped gas is typically spin-polarized, with all spin-dynamics frozen out. The development of optical trapping, which uses lasers to create the confining potential, was required to observe magnetic phenomena. Optical trapping, as shown in Fig. 2.15, allows the observation of spin dynamics through Stern-Gerlach measurements made on the condensate cloud [65]. These additional spin degrees of freedom quickly inspired new theoretical descriptions of the BEC gas in which spin-dynamics were included. The pioneering work of Ohmi and Machida [103] and Tin-Lun Ho [104] led to a wide study of these spinor condensates, where the spin structure of the BEC were examined. Theoretical predictions of spin ordering and topological spin textures have since been experimentally observed [105, 106], and spinor condensates have since been used to study topological knots found in the order parameter of a nematic spinor condensate [107].

One of the primary developments was that interfering lasers could produce a periodic potential which could trap atoms via the AC Stark effect [65]. By using multiple lasers, the periodic potential could be made to resemble the periodic potential felt by electrons in a crystal lattice. This setup became known as an optical lattice, and it was soon after discovered that atoms in an optical lattice approximately obey the Hubbard model [58, 67]. This demonstrated that cold atoms in optical lattices could be used to simulate the physics of electrons in solids [108]. Due to their artificial nature, experimenters possess a high degree of control over the microscopic parameters in these systems [109]. The lattice spacing, geometry, and depth can be controlled by adjusting the laser parameters, the particle statistics can be chosen by using either

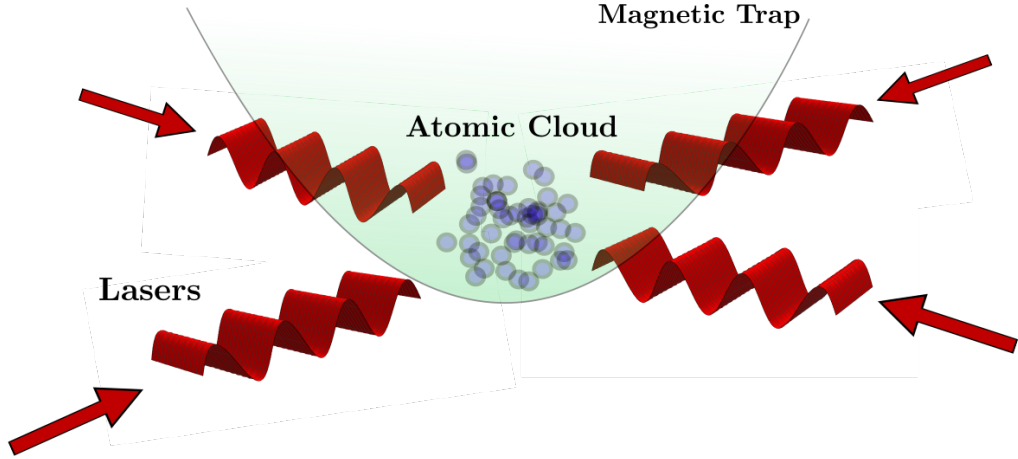


Figure 2.15: Trapping mechanisms used to study cold atomic gases. A harmonic magnetic trap is used to confine the atoms within a vacuum, while optical lasers are used to cool the atoms via Doppler cooling. Additional lasers are used to create an optical lattice, which confines the atoms to a periodic lattice potential.

fermionic or bosonic atoms, and the interaction strength between the atoms can even be tuned from repulsive to attractive using Feshbach Resonance. This incredible tunability allows experimentalists to fluidly explore the parameter space of the cold atom systems in many ways which are unique to the field.

For instance, to construct a one-dimensional optical lattice two counter-propagating lasers are used to construct a standing wave. For propagation along the \mathbf{x} axis, we may write the electric field for these two waves as $E_{\pm}(x, t) = E_0 e^{\pm i(kx - \omega_L t)}$. For neutral atoms coupled to a weak laser field, the leading order interaction will have the dipole form $\hat{H}_{\text{dip}} = -\hat{\mathbf{d}} \cdot \hat{\mathbf{E}}$, where \mathbf{d} is the electric dipole moment operator for the atom. This operator has only off-diagonal elements in the basis of the atomic eigenstates, $\langle e_i | \hat{\mathbf{d}} | e_j \rangle$, and the laser induces transitions between these coupled atomic states. If the laser frequency ω_L is tuned near a transition between a ground state $|g\rangle$ and an excited state $|e\rangle$, which differ in energy by an amount $\hbar\omega_e$, then the system will undergo Rabi oscillations at the frequency $\Omega \propto E(x) \langle e | d_z | g \rangle$, where $E(x)$ is the time-averaged electric field. Using the rotating frame approximation, we move to a frame rotating at the laser frequency ω_L and eliminate the counter-rotating

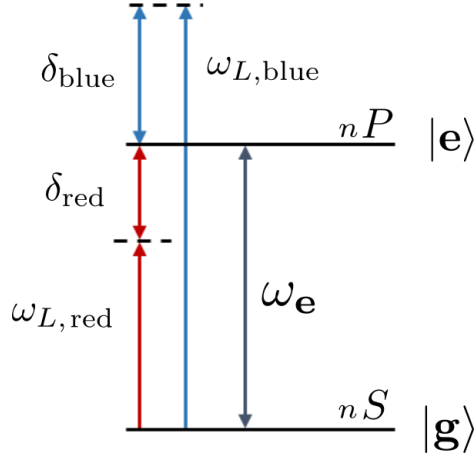


Figure 2.16: Energy structure of a two-level atomic system, which is optically coupled to an oscillating electric field of frequency ω_L . State $|g\rangle$ is the electronic ground state of the atom, while $|e\rangle$ is the first excited state, and is separated by an energy $\hbar\omega_e$. For the alkali atoms shown in Tab. 2.1, the laser detuning δ must be large enough to prevent sizable occupation of the excited state, which allows for an effective description in terms of the ground state. The detuning may be considered either “blue” or “red”, depending whether the laser energy is greater or less than the atomic transition frequency, respectively.

modes oscillating at $\omega_L + \omega_e$, while keeping modes which oscillate at the laser detuning $\delta \equiv \omega_L - \omega_e$, as shown in Fig. 2.16. If the laser detuning is small compared to ω_L , this approximation will be valid. For a low-amplitude laser, such that $|E|$ is small, the laser detuning will be large compared to the Rabi frequency $\delta > \Omega$. At low saturation, the occupancy of the excited state will be small, and we can adiabatically eliminate that state with second-order perturbation theory, leaving behind an effective interaction for the ground state $|g\rangle$.

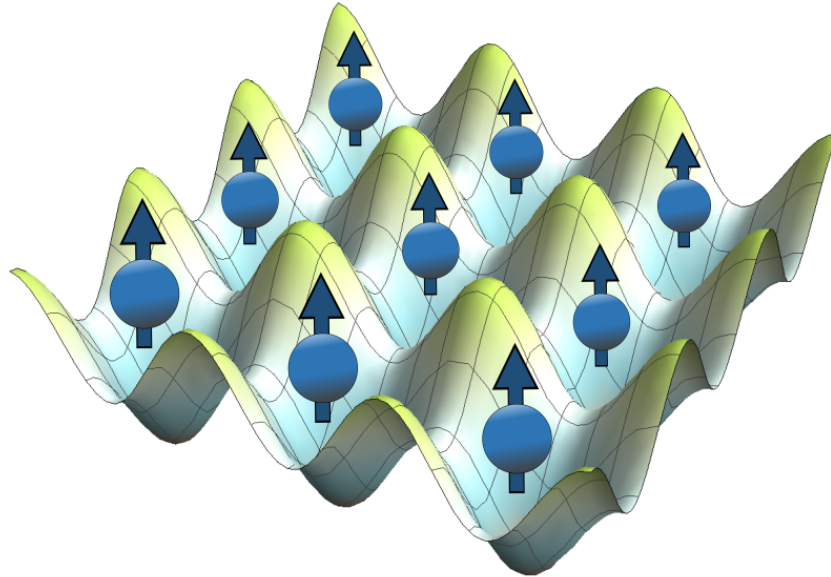
The effective ground state interaction takes the form $V_{\text{eff}}(x) \propto |E|^2 \cos^2(kx)/\delta$, such that it depends on the square of the laser amplitude, and exhibits a periodicity of half the laser wavelength $\lambda/2$. The effective force from this potential is $F_{\text{dip}} = -\nabla_x V_{\text{eff}}(x)$, and so spatial variations in the amplitude of the time-averaged standing wave creates an effective restoring force pointing towards the nodes or anti-nodes in the case of blue-detuned ($\delta > 0$) or red-detuned ($\delta < 0$) light, respectively. It is worth mentioning that the scattering rate from the trap varies as $\Gamma \propto |E|^2/\delta^2$,

	^{23}Na	^{87}Rb
nS-nP, ω_e	508 THz (590 nm)	382 THz (785 nm)
Spin-orbit	0.52 THz	6.8 THz
Hyperfine	1.8 GHz	6.8 GHz
nS-nP linewidth	$2\pi \times 10$ MHz	$2\pi \times 6$ MHz
Lattice scattering	9.9 mHz	0.5 mHz

Table 2.1: Atomic energy scales for two species of alkali atoms. These energies are used to calculate laser parameters needed to trap the atoms in an optical lattice, as discussed in Fig. 2.16. The optical lattice frequencies ω_L are tuned relative to the transition frequency between the highest occupied S orbital and the lowest unoccupied P orbital on the same shell. The detuning δ must be larger than both the spin-orbit and hyperfine splitting to produce degenerate angular momentum states in the lattice. The laser detuning and transition linewidth dictate the scattering rate of atoms out of the trap, which puts an upper-bound on the lifetime of cold atoms experiments.

and so it is advantageous to make the detuning as large as possible, while keeping it much smaller than the transition frequency ω_e . Approximate energies for two of the standard alkali species, sodium and rubidium, are shown in Tab. 2.1. By introducing additional lasers, a variety of lattice geometries and dimensionalities can be constructed, including two dimensional frustrated lattices such as triangular and kagome lattices [54, 110, 111].

For a low-temperature atomic gas in an optical lattice with a large trapping potential V_{eff} and weak interparticle interactions, the atoms remain in the the lowest Bloch band. In this scenario, we may approximate the minima of the trap at site i as harmonic potentials $V_i(x) \sim U(x - x_i)^2$. Furthermore, we may expand these Bloch waves in terms of Wannier functions, which are each spatially localized around a particular lattice site. This transformation gives a description which takes the form of a Hubbard Model (Eq. 2.1). By varying the trapping potential U , the atoms can be taken from the nearly-free electron limit to the tight-binding limit. In bosonic systems, this transition is called the Mott-superfluid transition and its observation was a hallmark achievement in the quest to model solid state physics using cold atoms



Atoms in an Optical Lattice

Figure 2.17: In an optical lattice, neutral atoms are trapped in the periodic wells of the laser potential via the AC Stark Shift. At low temperatures, the atoms in each potential well are approximated by a 3D harmonic oscillator. When the kinetic degrees of freedom have been frozen out, the remaining interaction is an effective spin-spin interaction. A ferromagnetic state is shown, but a multitude of the magnetic phases found in solid state systems are possible, as well as many phases which may be unique to cold atom systems.

[57]. Furthermore, since the optical lattice preserves spin degeneracy, interactions at sufficiently low temperatures take place solely in the form of magnetic interactions, resulting in an effective spin model. This includes the ability to simulate the Heisenberg Model and its phases, both classical—as depicted in Fig. 2.17—and exotic, such as spin liquids.

2.3.2 Quantum magnetism with ultracold atoms

A major challenge in using cold atoms to simulate magnetic models such as the Heisenberg Model, has been reaching the extremely low temperatures required. This is because to observe magnetic order, the thermal energy must be much smaller than

the superexchange energy ($k_b T \ll J$), and so a very low entropy-per-particle (\mathcal{S}/N) must be achieved to see the appearance of Néel ordering in these systems. With laser cooling followed by evaporative cooling, cold gases may be brought to approximately $\mathcal{S}/N \sim 1k_B$, [112]. Although this entropy-per-particle is low enough to observe Bose-Einstein condensation [98] and degeneracy in a Fermi gas [113], it is above the scale at which magnetic superexchange interactions are expected to dominate, $\mathcal{S}/N \sim 0.35k_B$, [55]. However, recent experimental advances in cooling have greatly reduced the accessible entropy [112, 114–116], and allowed successful demonstration of antiferromagnetic behavior [117, 118]. Coupled with the site-resolved imaging [64], there is a growing class of magnetic systems to create and probe. It is therefore the opportune time for theorists to explore the space of accessible phases, and help guide experimentalists towards unexpected findings.

Thus far, most theoretical studies of spin liquid states in cold atom systems have focused on fermionic systems with enhanced rotational symmetry [77, 79]. Therefore, the models being used are more symmetric than the minimal $SU(2)$ spin symmetry required by nature, and so spin liquid states in these systems are by nature highly symmetric. This enhanced symmetry may be a topological symmetry [119], or it may result from a decoupling of orbital and nuclear spins in systems of alkali-earth metal atoms [84]. The latter case produces $SU(N)$ symmetric models, where $N = 2S + 1$ and S is the nuclear spin. It has been proposed that these $SU(N)$ symmetric systems can be used to simulate several interesting phases, such as transition metal oxides, heavy-fermion materials, and spin liquids [83]. While enhanced symmetry is helpful, it is not necessary to create a QSL using ultracold atoms. Therefore, we believe that it is worthwhile to study emergent QSL behavior in models possessing only generic $SU(2)$ symmetry.

Large spin fluctuations are necessary to stabilize entangled magnetic phases such as VBCs and QSLs. In solid state systems this requires the spin on each site be

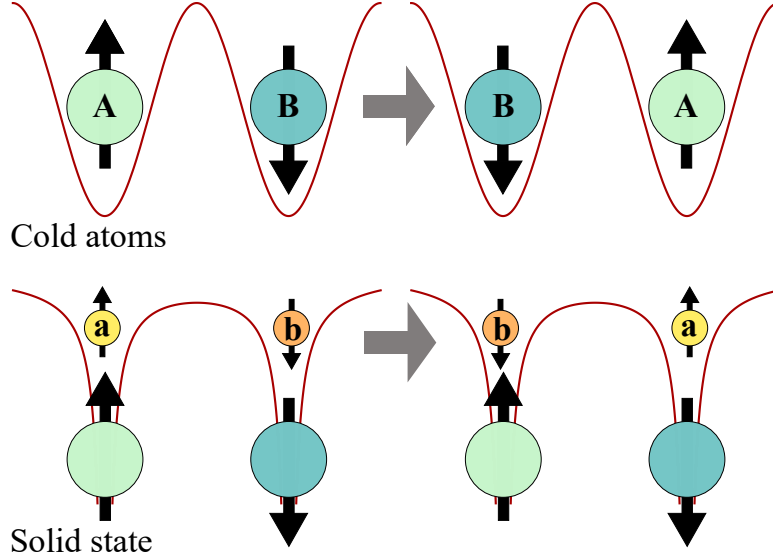


Figure 2.18: A comparison of the whole-atom exchange and superexchange mechanisms in cold atoms and solid state. For atomic gases optically confined to the Mott state (top), the exchange of whole spin- f atoms leads to magnetic fluctuations on the order of $2f$. In the solid state by contrast (bottom), electron superexchange restricts fluctuations to order ~ 1 , which can be small compared to the total spin on each site. Therefore, large-spin atoms are an ideal tool with which to study fluctuation-driven states—especially those which are not readily accessible with solid state systems.

as small as possible, because the spin- $1/2$ valence electrons mediate the exchange interactions [120]. Through an exchange of electrons on neighboring sites, the total spin projection on each site m can only change by an amount $\Delta m = \pm 1$, so for spin $f = 1/2$ systems the relative change in spin reaches the maximum possible value, $\Delta m/f = \pm 2$. For large values of the spin f on each site, Δm remains unchanged. This is because the exchange is still mediated by a single spin- $1/2$ electron, and so the relative change $\Delta m/f$ decreases with increasing f . In cold atom systems, whole atoms hop between the lattice sites to mediate exchange interactions [68], in a process called whole-atom exchange. This allows a change in spin of $\Delta m = \pm 2f$, and so $\Delta m/f = \pm 2$ for all values of f , and does not disappear at large spin. In cold atoms, large-spin systems may have the necessary fluctuations to possess spin liquid phases. The contrast between electron superexchange in a solid state system and whole-atom exchange in an optical lattice is shown pictorially in Fig. 2.18.

Chapter 3: A Spin Model for Ultracold Bosons

3.1 The Bose-Hubbard model

We begin with the continuum Hamiltonian for a dilute gas of spin- f bosons with spin-dependent interactions. This Hamiltonian may be written $\hat{H} = \hat{H}_1 + \hat{H}_2$, where \hat{H}_1 denotes the single-particle energy, and \hat{H}_2 denotes the two-particle interaction energy. The single-particle Hamiltonian,

$$\hat{H}_1 = \sum_{m=-f}^f \int d\mathbf{r} \hat{\psi}_m^\dagger(\mathbf{r}) \left[-\frac{\hbar^2 \nabla^2}{2M} + U_{\text{lat}}(\mathbf{r}) \right] \hat{\psi}_m(\mathbf{r}), \quad (3.1)$$

contains the kinetic and potential energy of the mass M atoms, written in terms of field operators $\hat{\psi}_m^\dagger(\mathbf{r})/\hat{\psi}_m(\mathbf{r})$, which create/annihilate spin- f bosons with hyperfine spin projection m at position \mathbf{r} . These field operators obey typical bosonic commutation relations,

$$[\hat{\psi}_m(\mathbf{r}), \hat{\psi}_{m'}^\dagger(\mathbf{r}')] = \delta(\mathbf{r} - \mathbf{r}') \delta_{m,m'}, \quad (3.2)$$

and

$$[\hat{\psi}_m(\mathbf{r}), \hat{\psi}_{m'}(\mathbf{r}')] = 0. \quad (3.3)$$

The potential energy associated with the presence of the optical lattice takes the form $U_{\text{lat}}(x, y) = V_{\text{trap}}(\sin^2[kx] + \sin^2[ky])$ for a square lattice, where V_{trap} is the depth of the optical lattice and is proportional to the laser intensity, while k is the wavevector of the lattice laser—as described in Subsec. 2.3.1.

	²³Na	⁸⁷Rb
Thermal de Broglie	37.3 μm	19.2 μm
Lattice wavelength	514 nm	514 nm
Lattice constant	257 nm	257 nm
Lattice SHO width	387 \AA	409 \AA
Scattering Length, a_0	26.4 \AA	46.3 \AA
van der Waal's radius	2.3 \AA	3.0 \AA

Table 3.1: Relevant length scales for two commonly used alkali atoms in an optical lattice at $T = 300$ pK. At these ultracold temperatures, the thermal de Broglie wavelength is much larger than the van der Waal's radius of their interaction potential. This results in an effective contact interaction, characterized by the s-wave scattering length a_0 at low energies. Since a_0 is much smaller than the lattice constant only onsite interactions are relevant.

For neutral atoms, the interaction energy takes the form of a Lennard-Jones potential. However, in the ultracold limit the thermal de Broglie wavelength of the atoms at temperature T ,

$$\lambda = \frac{h}{\sqrt{2k_BMT}}, \quad (3.4)$$

is longer than the characteristic length of their interaction potential, as shown in Tab. 3.1, which provides a comparison of relevant length scales. In this case, the two-body interaction is effectively a contact interaction dependent on the combined spin F of the two colliding atoms, given by $v(\mathbf{r}, \mathbf{r}') = g_F \delta(\mathbf{r} - \mathbf{r}')$. The coupling constant g_F can be determined by applying the Born Approximation to first order [121], and is given by

$$g_F = \frac{4\pi\hbar^2}{M} a_F, \quad (3.5)$$

where a_F is the s-wave scattering length of the spin- F scattering channel, and corresponds to the low-energy ($l = 0$) term in the partial wave expansion of the scattered wavefunction. These scattering lengths are shown in Tab. 3.2 for several commonly

Atomic Species		Scattering Lengths (units of Bohr radii, $a_B \sim 0.53\text{\AA}$)				
Isotope	f	a_0	a_2	a_4	a_6	Source
^{23}Na	1	50.0 ± 1.6	55.0 ± 1.7			[122]
^{87}Rb	2	87.4 ± 1.0	92.4 ± 1.0	100.5 ± 1.0		[123, 124]
^{52}Cr	3	40 ± 10	-7 ± 20	58 ± 6	102.5 ± 0.4	[125–127]
^{164}Dy	8	92 ± 8	N/A			[102]

Table 3.2: S-wave scattering lengths for several commonly used bosonic isotopes. These values are determined by comparing multi-channel scattering calculations with experimental measurements of collisional dynamics and magnetic Feshbach resonances [127–129]. They include short-ranged isotropic contributions from magnetic DDIs, in addition to electronic Born-Oppenheimer molecular potentials [130, 131]. For ^{52}Cr and ^{164}Dy —which have large dipole moments—the scattering lengths vary greatly across different spin channels, and reliable values are difficult to extract by these methods. For alkali atoms on the other hand, the scattering lengths are known to high accuracy, and roughly the same through each channel

used atoms. We note that the natural decoupling of the interaction into total angular momentum channels, each parametrized by a scattering length a_F , arises from the rotational symmetry of the low-energy interaction, which conserves the total angular momentum of two bosons during a collision [104].

With these considerations, the spin-dependent two-particle interaction energy,

$$\hat{H}_2 = \frac{1}{2} \sum_{F,M} g_F \int d\mathbf{r} \hat{A}_{FM}^\dagger(\mathbf{r}) \hat{A}_{FM}(\mathbf{r}), \quad (3.6)$$

is written in terms of the operators $\hat{A}_{FM}^\dagger/\hat{A}_{FM}$ which create/annihilate a pair of atoms with total spin F and projection M . These operators are related to the field operators $\hat{\psi}_m^\dagger(\mathbf{r})$ through the Clebsch-Gordan coefficients as follows,

$$\hat{A}_{FM}^\dagger(\mathbf{r}) = \sum_{m,m'} \langle f, m; f, m' | F, M \rangle \hat{\psi}_m^\dagger(\mathbf{r}) \hat{\psi}_{m'}^\dagger(\mathbf{r}) \quad (3.7)$$

Furthermore, from the symmetry of the Clebsch-Gordan coefficients (see App. B.1)

and the commutation relations of the bosonic field operators, we find that $\hat{A}_{FM}^\dagger(\mathbf{r}) = 0$ for odd values of F . Therefore, scattering only occurs through even spin channels. Throughout this work, all sums over F imply a sum over the even channels $F = 0, 2, 4, \dots$ only, unless otherwise specified.

In the presence of the periodic optical lattice potential, the single-particle wavefunctions will take the form of Bloch waves. Since we wish to describe insulating magnetic states, it is convenient in the tight-binding limit to use wavefunctions which are localized around each site. A common choice for these functions are the Wannier functions, which are real, orthogonal functions constructed from the Bloch waves and centered around each lattice site. These are the optimal basis to use when the thermal energy is small compared to the lattice depth ($k_B T \ll V_{\text{trap}}$). In this case, the atoms become kinetically trapped—residing at the bottom of the potential well of each lattice site—though tunnelling between sites may still occur. For example, for ^{87}Rb at 300 pK, we have a thermal energy of $k_B T/h \sim 6.25$ Hz. If an optical lattice of wavelength $\lambda_{\text{lat}} = 514$ nm creates a periodic potential of amplitude $V_{\text{trap}} \sim 16 E_R = 16 \hbar^2 k_{\text{lat}}^2 / 2M \sim 142$ kHz, then the atoms will be kinetically trapped.

When we consider the dynamics of atoms confined to the isolated potential minima of each lattice site, we may Taylor expand to second order and treat every minima as a spherically symmetric simple harmonic oscillator (SHO) potential. In this case, the Wannier functions may be approximated by 3D SHO eigenstates centered around each lattice site. Additionally, if the thermal energy is small compared to the spacing between the SHO energy levels ($k_B T \ll \hbar \omega_{\text{trap}}$, with $\omega_{\text{trap}} = \sqrt{2V_{\text{trap}} k^2 / M} \sim 2\pi \times 24.6$ MHz, as shown in Tab. 3.6) then we may assume that only the ground state mode of the oscillator to be occupied. With these considerations, we expand our field operators using

$$\hat{\psi}_m^\dagger(\mathbf{r}) = \sum_i \Phi(\mathbf{r} - \mathbf{r}_i) \hat{b}_{i,m}^\dagger, \quad (3.8)$$

where the operator $\hat{b}_{i,m}^\dagger$ ($\hat{b}_{i,m}$) creates(annihilates) a spin- f bosonic atom on site i and

with magnetic hyperfine projection m , and $\Phi(\mathbf{r} - \mathbf{r}_i)$ is the wavefunction centered around site i . For the ground state of a 3D SHO we have $\Phi(\mathbf{r}) = \phi(x)\phi(y)\phi(z)$, where

$$\phi(x) = \left(\frac{M\omega_{\text{trap}}}{\pi\hbar} \right)^{\frac{1}{4}} e^{-\frac{M\omega_{\text{trap}}x^2}{2\hbar}}, \quad (3.9)$$

for each of the Cartesian coordinates.

When Eq. 3.8 is inserted into the continuum Hamiltonian of Eqs. 3.1 and 3.6, the result is a tight-binding Hamiltonian where the interaction between particles on different sites is directly proportional to the overlap of their single-particle wave functions. We obtain

$$\hat{H} = - \sum_{i,j} t_{i,j} \hat{b}_{i,m}^\dagger \hat{b}_{j,m} + \frac{1}{2} \sum_{FM} g_F \sum_{i,j,k,l} U_{i,j,k,l} \hat{A}_{i,j}^{FM\dagger} \hat{A}_{k,l}^{FM}, \quad (3.10)$$

where $t_{i,j} = t_{i,j}^{\text{hop}} + t_{i,j}^{\text{overlap}}$ comes from the single-particle term (Eq. 3.1), with

$$t_{i,j}^{\text{hop}} = \int d\mathbf{r} \Phi^*(\mathbf{r} - \mathbf{r}_i) \left(\frac{\hbar^2 \nabla^2}{2M} \right) \Phi(\mathbf{r} - \mathbf{r}_j) \quad (3.11)$$

and

$$t_{i,j}^{\text{overlap}} = V_{\text{trap}} \int d\mathbf{r} \Phi^*(\mathbf{r} - \mathbf{r}_i) [\sin^2(kx) + \sin^2(ky) + \sin^2(kz)] \Phi(\mathbf{r} - \mathbf{r}_j), \quad (3.12)$$

while the interaction term (Eq. 3.6) gives

$$U_{i,j,k,l} = \int d\mathbf{r} \Phi(\mathbf{r} - \mathbf{r}_i) \Phi(\mathbf{r} - \mathbf{r}_j) \Phi^*(\mathbf{r} - \mathbf{r}_k) \Phi^*(\mathbf{r} - \mathbf{r}_l). \quad (3.13)$$

For these parameters, the leading order contribution is typically several orders of magnitude larger ($\gtrsim 6$) than the next-leading order, and so we retain only the dominant contributions from each. For example, the leading-order term for $t_{i,j}^{\text{overlap}}$ is the on site term $t_{i,i}^{\text{overlap}}$, and results in spatially-uniform shift to the chemical potential.

Bose-Hubbard Model phase diagram

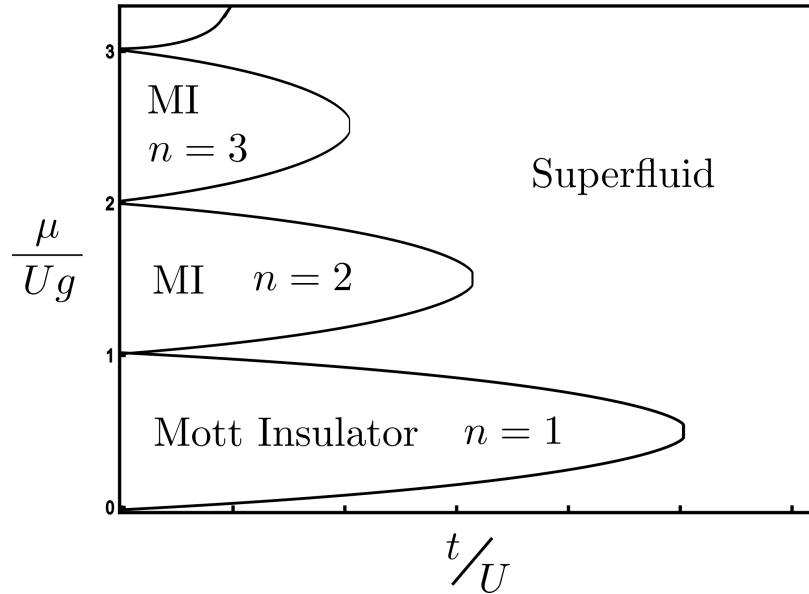


Figure 3.1: A schematic mean field phase diagram for the scalar Bose-Hubbard model, in which the interactions are spin independent. By tuning the optical lattice depth, the ratio t/U may be varied, and the system moves between the Mott insulator and superfluid phases—a feature of the model which was first proposed [132], and then successfully observed experimentally for the first time using ultracold atoms [57]. For spin-dependent interactions, one may assume a similar phase diagram, but with rich spin structure as a function of the different scattering lengths a_F .

In the one-particle-per-site limit this overall shift may simply be ignored. For the hopping term $t_{i,j}^{\text{hop}}$, the on-site contribution is zero, while all hopping beyond nearest neighbors is subdominant, and so we retain only nearest-neighbor hopping ($t \equiv t_{i,j}$ if i and j are nearest-neighbors). While for the interaction energy the on-site term $U_{i,i,i,i}$ dominant, and so off-site interactions may be neglected ($U \equiv U_{i,i,i,i}$)—which is to be expected from an effective contact interaction.

After dropping all sub-dominant and trivial terms, we obtain a form of the spin- f Bose-Hubbard model [67, 132, 133] with spin-dependent interactions. This is given by

$$\hat{H}_{BH} = -t \sum_{\langle i,j \rangle} \sum_{m=-f}^f (\hat{b}_{i,m}^\dagger \hat{b}_{j,m} + \text{H. c.}) + U \sum_i \sum_{F=0,2,\dots}^{2f} g_F \hat{P}_i^F, \quad (3.14)$$

where i ranges over all N lattice sites, and $\langle i, j \rangle$ denotes a sum over all distinct

nearest-neighbor pairs. The on-site interaction is written in terms of projection operators $\hat{P}_i^F = \sum_{M=-F, \dots, F} |F, M\rangle_{ii} \langle F, M|$, which project the two-particle states on site i into the subspace, with total angular momentum F .

By manipulation of the optical lattice depth (V_{trap}), it is possible to tune the ratio U/t from Eq. 3.14. For small U/t the system behaves as an atomic superfluid where the atoms are allowed to hop freely around the lattice. The wavefunctions of the superfluid atoms are therefore spatially extended throughout the lattice and are all at the $k = 0$ point of the lowest Bloch band. This may be written as $|SF\rangle = (\hat{b}_{k=0}^\dagger)^N |0\rangle$. On the other hand, for large U/t the system is a Mott insulator, with atoms kinetically trapped on each lattice site. The wavefunction for this phase may be written $|MI\rangle = \prod_i (\hat{b}_i^\dagger)^n |0\rangle$. By tuning the lattice depth alone, the system can be taken back and forth between these two phases. This allows experimentalists to explore a large region of the systems parameter space. The phase diagram for a spinless system has been understood theoretically [67, 132] (as shown in Fig. 3.1) and features such as the Mott-superfluid transition have been observed experimentally [57].

3.2 Deriving an effective spin model

With spin-dependent interactions, we anticipate that the Mott insulating lobes of Fig. 3.1 contain various spin orderings and phases. To determine these phases we require a description of the Mott limit, where the kinetic energy is completely quenched relative to the on-site repulsion ($t \ll U$). This allows for a perturbative expansion of Eq. 3.14 to second order in t/U . In this case, the unperturbed Hamiltonian is $\hat{H}_0 = U \sum_i \sum_{FM} g_F \hat{P}_i^F$. If we take $N_{\text{atoms}} = N_{\text{sites}}$, then the ground state will be the one-particle-per-site Mott insulating state with an energy $E = 0$. A state with a single doubly-occupied site will be higher in energy with $E = U g_F$. The perturbation

Atom	f	$\frac{V_{\text{trap}}}{E_{\text{R}}}$	Θ_{Fesh}	$\frac{g_2}{g_0}$	$\frac{U_{g_0}}{t}$	$\frac{t}{E_{\text{dip}}}$	$\frac{4t^2/U_{g_0}}{E_{\text{dip}}}$
^{23}Na	1	12	0	1.10	42.5	112	10.6
^{87}Rb	2	11	0	1.06	33.6	67.6	2.91
^{52}Cr	3	10	0	0.175	17.2	12.00	2.78

Table 3.3: Ratios of lattice and interaction energy scales for particular lattice depths, in the absence of any Feshbach-tuned scattering. The lattice depths are chosen to satisfy $U_{g_0} > t > E_{\text{dip}}$ and $\frac{4t^2}{U_{g_0}} > E_{\text{dip}}$, which are required for Eqs. 3.14 and 3.19 to be valid.

$\hat{H}' = -t \sum_{\langle i,j \rangle} \sum_{m=-f}^f (\hat{b}_{i,m}^\dagger \hat{b}_{j,m} + \text{H. c.})$ connects the ground state and first excited state manifolds. We then find the effective two-site Hamiltonian in the Mott sector to be

$$\hat{H} = -\frac{4t^2}{U} \sum_{FM} \frac{1}{g_F} \sum_{\substack{m,m' \\ n,n'}} C_{m,m'}^{FM} C_{n,n'}^{FM} |m, m'\rangle \langle n, n'| \quad (3.15)$$

at second order, where $|m, m'\rangle$ represents a state where the two atoms on nearest-neighbor sites i and j have hyperfine spin projections m and m' . Finally, to put this in the common form (cf. [62, 72]) we write it in terms of the total spin projection operators $\hat{P}_{i,j}^F$, giving

$$\hat{H} = -J \sum_{\langle i,j \rangle} \sum_{FM} \frac{1}{g_F} |F, M\rangle \langle F, M| = -J \sum_{\langle i,j \rangle} \sum_F \frac{1}{g_F} \hat{P}_{i,j}^F, \quad (3.16)$$

where $J = 4t^2/U$ sets the exchange energy J/g_F through each channel, and the projection operator $\hat{P}_{i,j}^F$ now projects two sites i and j into total angular momentum state F . The kinetic, potential, and exchange energies (t , U and J) are calculated for various trap depths and plotted in Fig. 3.2, to determine the validity of our effective model, Eq. 3.15. A suitable choice of lattice depth, and the resulting energies, are shown for $f = 1, 2, 3$ atoms in Tab. 3.3.

At this point, one commonly re-expresses the $\hat{P}_{i,j}^F$ operators of Eq. 3.16 in terms of

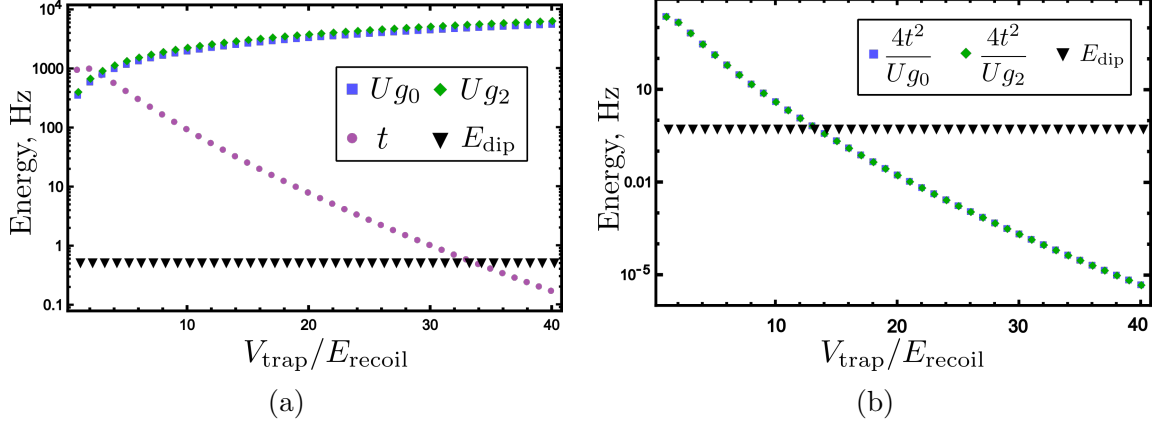


Figure 3.2: (a) The magnitude of t and $U g_F$ from Eq. 3.14, as calculated from Eqs. 3.11 and 3.13. (b) The magnitude of the exchange interactions from Eq. 3.19. These are shown in comparison to the nearest-neighbor dipole-dipole interaction, and as a function of lattice depth V_{trap} for $f = 1$ ^{23}Na atoms. For our description to be valid, we require that $U g_0 > t > E_{\text{dip}}$ and $\frac{4t^2}{U g_0} > E_{\text{dip}}$, which from these plots can be seen to occur for $V_{\text{trap}}/E_{\text{recoil}} \sim 5\text{--}15$, well within experimental limits.

a polynomial in the Heisenberg coupling $\hat{\mathbf{S}}_i \cdot \hat{\mathbf{S}}_j$, or with tensor operators of increasing rank. For example, in terms of spin operators we may write

$$\hat{H} = \sum_{\langle i,j \rangle} \sum_{n=0}^{n_{\text{max}}=2f} c_n (\hat{\mathbf{S}}_i \cdot \hat{\mathbf{S}}_j)^n, \quad (3.17)$$

where successively higher powers of $\hat{\mathbf{S}}_i \cdot \hat{\mathbf{S}}_j$ are introduced for larger hyperfine spin f . For a spin-1/2 system, where $n_{\text{max}} = 1$, Eq. 3.17 simply recovers the Heisenberg model of Eq. 2.2. For a spin-1 system, where $n_{\text{max}} = 2$, we obtain the bilinear-biquadratic Heisenberg model, which has a long history of study for 1D antiferromagnetic chains [134–139], and has been looked at more recently on higher-dimensional lattices [140, 141]. It has also previously been studied in the context of spin- f cold atoms [62, 142–144]. In all cases, a competition between nematic order and dimerization is predicted. We show in Chap. 4 that this competition occurs at larger f as well.

While expansions in terms of Heisenberg couplings have been successful for low-spin systems, these methods do not move fluidly from one spin f to another, since one must continually introduce new terms in the Hamiltonian upon increasing the spin.

Previous schemes overcome this difficulty by describing the terms as stereographic projections of polyhedra of increasing order [145, 146]. In this work, we instead proceed by returning our Hamiltonian to the formalism of second quantization.

To return Eq. 3.16 to second quantization we write the projection operators as $\hat{P}_{i,j}^F = \sum_M \hat{A}_{i,j}^{FM\dagger} \hat{A}_{i,j}^{FM}$, where the $\hat{A}_{i,j}^{FM\dagger}(\hat{A}_{i,j}^{FM})$ pair operators create(annihilate) a pair of bosons on sites i and j in total angular momentum state $|F, M\rangle$, which in analogy with Eq. 3.7 are given by

$$\hat{A}_{i,j}^{FM} = \sum_{m,n} C_{m,n}^{FM} \hat{b}_{i,m} \hat{b}_{j,n} \quad (3.18)$$

in terms of the boson operators $\hat{b}_{im}^\dagger(\hat{b}_{im})$. With these considerations in mind, we write our spin Hamiltonian in second quantization as

$$\hat{H}_{\text{spin}} = -J \sum_{\langle i,j \rangle} \sum_{F,M} \frac{1}{g_F} \hat{A}_{i,j}^{FM\dagger} \hat{A}_{i,j}^{FM}. \quad (3.19)$$

In this form, to describe a system with a given atomic hyperfine spin f , one simply calculates the Clebsch-Gordan coefficients through the even- F pairing channels, up to $2f$. The straightforward calculation of these coefficients then provides for a much simpler study at large f .

The presence of the Clebsch-Gordan coefficients $C_{m,n}^{FM} = \langle f, m; f, n | F, M \rangle$ in Eq. 3.18 ensures that the pair operators $\hat{A}_{i,j}^{FM}$ rotate irreducibly as an object with angular momentum F under $SU(2)$ spin rotations. However, despite rotating like particles with a well defined angular momentum, these operators do not have the commutation relations of particles (either fermionic or bosonic), and therefore the two atoms created by this operator do not represent a bound molecular state. We find that for two bonds

$i-j$ and $k-l$ the commutation relations are

$$\left[\hat{A}_{i,j}^{FM}, \hat{A}_{k,l}^{F'M'\dagger} \right] = \begin{cases} \delta_{F,F'} \delta_{M,M'}, & \text{for } i-j = k-l \\ 0, & \text{for } i-j \neq k-l, \end{cases} \quad (3.20)$$

but for bonds which share only a single site (in this case we choose $i = k$ and $j \neq l$) we have

$$\left[A_{i,j}^{FM}, A_{k,l}^{F'M'\dagger} \right] = C_{m,m'}^{FM} C_{m,n'}^{F'M'} \delta_{k,i} b_{l,n'}^\dagger b_{j,m'}. \quad (3.21)$$

This prevents us from a description where the $|FM\rangle$ states represent fundamental spins defined on the bonds of the lattice.

Another important property of the $\hat{A}_{i,j}^{FM}$ is that since $C_{m,m'}^{FM} = 0$ unless $m + m' = M$, the $\hat{A}_{i,j}^{FM}$ operators only couple neighboring spins when this condition is met. So for example, \hat{A}^{F0} operators will only couple spins with $m' = -m$, and the $\hat{A}^{2f,2f}$ operators will only couple spins of $m = m' = f$. Therefore, terms in Eq. 3.19 with $|M| = 2f$ describe ferromagnetic interactions, while terms with $M = 0$ describe antiferromagnetic interactions.

3.3 Tuning interactions with optical Feshbach resonance

A primary attraction of studying cold atom systems, is the possibility of tuning interparticle interactions. While the exchange energy J from Eq. 3.19 may be controlled by tuning the optical lattice depth, to fully explore the phase diagram we require at least some control of the scattering lengths a_F , and hence the coupling constants g_F . Historically, magnetic Feshbach resonances [147–155] have been used to tune the scattering-length by coupling an open scattering channel with the close-channel of a molecular bound state. Unfortunately, the magnetic field used in this technique

leads to strong Zeeman splitting and the subsequent freezing of the spin dynamics, effectively resulting in a scalar Bose gas, as shown in Fig. 3.1.

Rather, to retain the hyperfine spin dynamics, a wide range of light-induced tuning methods—generally referred to as optical Feshbach resonances—have been proposed and demonstrated for many different atomic species [156–182]. A schematic diagram of the energy levels involved in this process are shown in Fig. 3.3. The effect of these techniques depends on the nature of the particular molecular state which is being optically coupled to the incident scattering channel. In this section, we follow the proposal of Ref. [176] to produce a shift in the scattering length which is dependent on the total spin F .

To achieve the spin-dependent tuning that we seek, we consider an OFR between pairs of atoms by shining a laser tuned near a transition to an excited molecular state, labeled by orbital angular momentum $L = 1$, electronic spin $S = 0$, and total electronic angular momentum $J = 1$ (see Fig. 3.4). The nuclear angular momentum is not relevant so long as the detuning of the laser is large compared to the hyperfine splitting (see Eq. 3.4). In the cold collision limit the rotational angular momentum of the nuclei vanishes ($R = 0$) and so we may neglect rotation induced energy splittings of the molecular bound states. Since the incident atoms are chosen to have no total orbital angular momentum, the only allowed optical transitions are to a $L = 1$ molecular state.

The Hamiltonian for the relevant electronic and nuclear degrees of freedom involved in this process may be written in the form

$$\hat{H}_{\text{Fesh}} = \hat{H}_{\text{atom}} + \hat{H}_{\text{mol}} + \hat{H}_{\text{Int}}, \quad (3.22)$$

where since the effects of an optical Feshbach resonance are local, we have dropped spatial indices from the bosonic operators. The atomic contribution consists of the

Optical Feshbach Resonance for Alkali gas

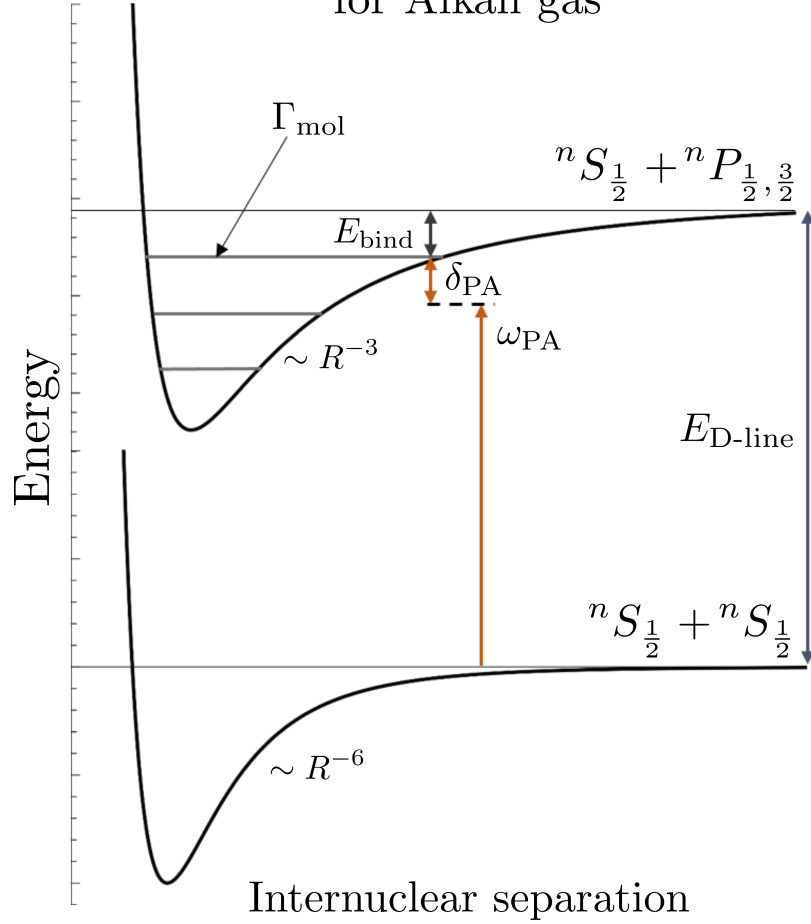


Figure 3.3: A schematic of optical Feshbach resonance. Two alkali atoms in the ${}^nS_{1/2}$ ground state are coupled to a bound molecular state (of which there are many, each with differing spin and/or vibrational/rotational quantum numbers) through the use of a photoassociation laser. If the laser detuning δ_{PA} is large compared to the splitting of these molecular bound states, then photo-induced occupation of the molecular state will be small. The result is an effective shift in the scattering lengths of the ground state atoms. Additionally, since coupling to the molecular state depends on the total electronic angular momentum of the colliding atoms, and since the projections of different electronic states into the hyperfine basis are not equal, the shift through each spin channel will be different, resulting in the form of Eq. 3.28.

hyperfine coupling of the nuclear and electronic angular momentum, which is given by

$$\hat{H}_{\text{atom}} = E_{HF} \sum_{\substack{m_j, m'_j \\ m_i, m'_i}} (\hat{\mathbf{J}})_{m_j, m'_j} \cdot (\hat{\mathbf{I}})_{m_i, m'_i} \hat{b}_{m_j, m_i}^\dagger \hat{b}_{m'_j, m'_i}, \quad (3.23)$$

where E_{HF} is the atomic hyperfine coupling constant, $\hat{\mathbf{J}}$ is the total electronic angular momentum operator, $\hat{\mathbf{I}}$ is the total nuclear angular momentum operator, and \hat{b}_{m_s, m_i} annihilates a boson in the state $|m_s, m_i\rangle$.

The molecular Hamiltonian \hat{H}_{mol} models the binding energy of the molecule, and is given by

$$\hat{H}_{\text{mol}} = E_B \sum_{m_i, m'_i} \hat{B}_{m_i, m'_i}^\dagger \hat{B}_{m_i, m'_i}, \quad (3.24)$$

where $\hat{B}_{m_i, m'_i}^\dagger$ creates a molecule with an electronic spin $S = 0$ and electronic orbital angular momentum $J = 1$. If the quantization axis of the electronic orbital angular momentum J is chosen in the same direction as the Feshbach laser's angular momentum, then only one of the molecular states in the $J = 1$ triplet is coupled via the laser to the atomic singlet (such that $\Delta M_J = \pm 1$). We denote the binding energy of one of these molecular states by E_B .

Finally, the Feshbach interaction term \hat{H}_{Int} coupling between the unbound atoms and the molecular bound state induced by the photoassociation laser. This photo-induced molecular formation is modeled with the dipole approximation, and couples incident circularly polarized light with the atoms. After applying the rotating wave approximation to this description we obtain

$$\hat{H}_{\text{Int}} = \sum_{m_i, m'_i} \Omega e^{-i\omega_{\text{PA}} t} \hat{B}_{m_i, m'_i}^\dagger \left(\frac{\hat{b}_{\frac{1}{2}, m_i} \hat{b}_{-\frac{1}{2}, m'_i} - \hat{b}_{-\frac{1}{2}, m_i} \hat{b}_{\frac{1}{2}, m'_i}}{\sqrt{2}} \right) + \text{H. c.} \quad (3.25)$$

where ω_{PA} is the angular frequency of the photoassociation laser which induces the molecule formation, and the term in parenthesis destroys an atomic pair with $S = 1$

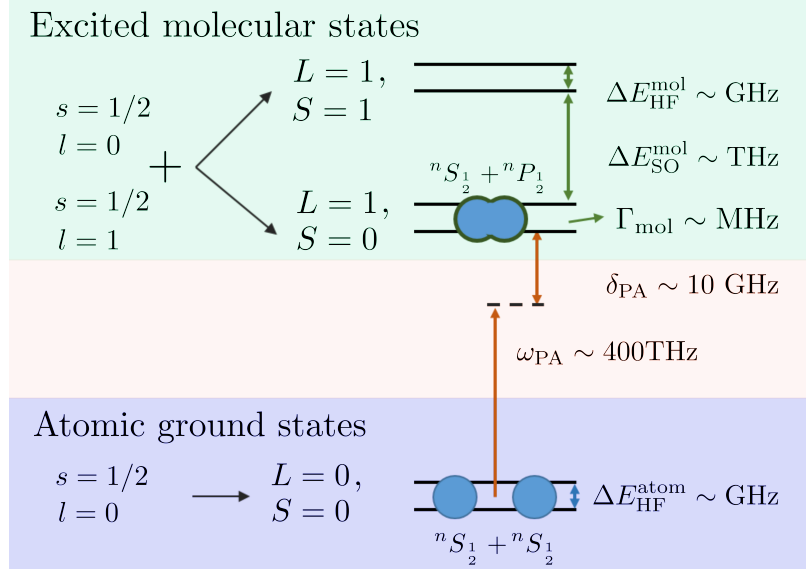


Figure 3.4: An example of some energy scales relevant to the optical Feshbach resonance proposed in Sec. 3.3. For alkali atoms, the photoassociation laser couples the $L = 0, S = 0$ ground state to the $L = 1, S = 0$ excited state. If the laser detuning δ_{PA} is large compared to the molecular and atomic hyperfine splitting, then different hyperfine states will not be resolved during this photoassociation, and so the process is independent of the nuclear spin.

and $L = 0$, while the nuclear spins remain arbitrary. The generalized Rabi frequency Ω is proportional to the square of the dipole-transition matrix element between the atomic and molecular states and the laser intensity, and is thus a tunable parameter.

The detuning between the laser energy and molecular binding energy is defined $\delta_{\text{PA}} \equiv \hbar\omega_{\text{PA}} - E_b$, and plays a crucial role in the analysis of this perturbation. Mainly, for large detuning the stimulated occupation of the molecular state will remain small. Then, following [176], we may adiabatically eliminate the molecular state using second-order perturbation theory to obtain an effective interaction for the atoms, which gives

$$\hat{H}_{\text{Fesh}} = -\frac{\Omega^2}{\delta_{\text{PA}}} \sum_{m_i, m'_i} \left(\frac{\hat{b}_{\frac{1}{2}, m_i} \hat{b}_{-\frac{1}{2}, m'_i} - \hat{b}_{-\frac{1}{2}, m_i} \hat{b}_{\frac{1}{2}, m'_i}}{\sqrt{2}} \right)^\dagger \left(\frac{\hat{b}_{\frac{1}{2}, m_i} \hat{b}_{-\frac{1}{2}, m'_i} - \hat{b}_{-\frac{1}{2}, m_i} \hat{b}_{\frac{1}{2}, m'_i}}{\sqrt{2}} \right). \quad (3.26)$$

If the overall chemical potential is chosen such that only a single hyperfine eigenstate

is occupied, we may project the operators $\hat{b}_{m_j, m_i}^\dagger$ into the hyperfine basis and retain only terms that lie within the appropriate hyperfine sector.

By projecting Eq. 3.26 into the total hyperfine spin basis $|F, M\rangle$, we obtain

$$\hat{H}_{\text{Fesh}} = -\frac{\Omega^2}{\delta_{\text{PA}}} \sum_{FM} \alpha_F \hat{A}_{i,i}^{FM\dagger} \hat{A}_{i,i}^{FM}, \quad (3.27)$$

where coefficient α_F is the square of the overlap between the electronic spin singlet ($S = 0$) and the hyperfine state with total spin F [183]. As detailed in the App. F.1, we find

$$\alpha_F = \frac{(2f+1)(f+1) - F(F+1)/2}{2(i+1/2)^2} \quad (3.28)$$

for alkali atoms which have $s = 1/2$ and nuclear spin $i > 0$, while for ^{52}Cr which has $l = i = 0$ we find $\alpha_F = \delta_{F,0}$, where δ is the Kronecker delta symbol. A plot of α_F as a function of F is shown in Fig. 3.5, where it is seen that α_F decreases with increasing F . In this way, the $F = 0$ channel will be affected the most by this form of optical Feshbach resonance, while scattering through the $F = 2f$ channel will be affected the least.

Most importantly, since Eq. 3.27 takes the same form as the scattering interaction from Eq. 3.14, we can absorb the effect of the optical Feshbach resonance by defining a new scattering length a_F , and hence a new coupling of

$$g_F = g_F^{(0)} - \alpha_F \frac{\Omega^2}{U\delta_{\text{PA}}}. \quad (3.29)$$

where $g_F^{(0)}$ now denotes the contribution from the background scattering lengths from Tab. 3.2, which include on-site dipole-dipole interactions. From this we may define a dimensionless parameter, which we call the Feshbach tuning

$$\Theta_{\text{Fesh}} \equiv \frac{\Omega^2}{\delta_{\text{PA}}} \frac{1}{U} \frac{M}{4\pi\hbar^2 a_B} \propto \frac{\Omega^2}{\delta_{\text{PA}}}, \quad (3.30)$$

Feshbach parameters, α_F

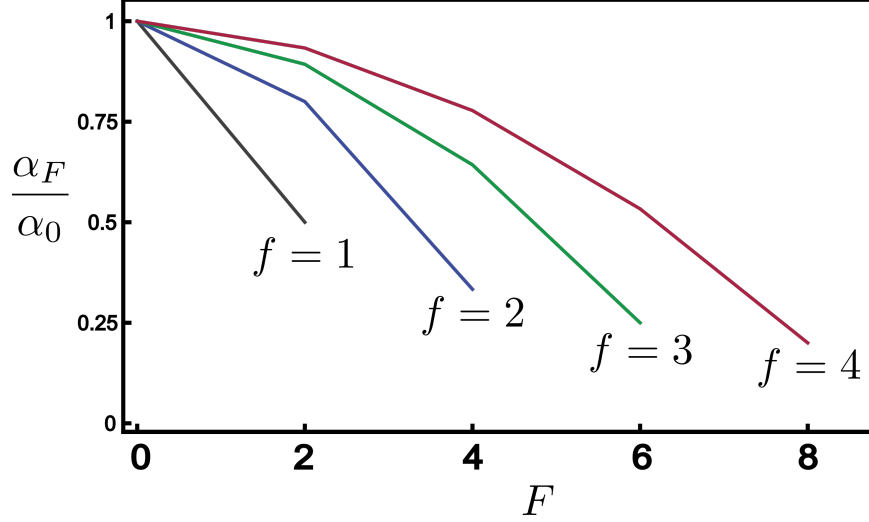


Figure 3.5: A plot of α_F/α_0 from Eq. 3.28 for alkali atoms as a function of F . Since α_F monotonically decreases with increasing F , the $F = 0$ channel will exhibit the largest shift in scattering length for a given Feshbach tuning Θ_{Fesh} . For alkali atoms, the background scattering lengths are roughly equal, which allows OFR tuning to access the limit where $g_0 \ll g_{F \neq 0}$, resulting in the effective singlet Hamiltonian of Eq. 3.31.

which characterizes the shift in the scattering lengths in units of the Bohr radius a_B . The magnitude of this parameter may be manipulated by changing the intensity and detuning of the Feshbach laser, while the sign may be changed by implementing either “blue” ($\delta_{\text{PA}} > 0$) or “red” ($\delta_{\text{PA}} < 0$) detuning.

In particular, if we choose the Feshbach tuning Θ_{Fesh} such that $a_0 \lesssim a_B$, then since α_F forms an decreasing series with F we find that super-exchange ($J = 4t^2/Ug_F$) through the $F = 0$ channel will dominate over the other channels. In this case, the ratio $g_0/g_{F \neq 0}$ is small, and we may keep only the $F = 0$ channel from Eq. 3.19, giving us an effective singlet Hamiltonian of

$$\hat{H}_{00} = -\frac{4t^2}{Ug_0} \sum_{\langle ij \rangle} \hat{A}_{ij}^{00\dagger} \hat{A}_{ij}^{00}, \quad (3.31)$$

where $\hat{A}_{ij}^{00} = \sum_m (-1)^m \hat{b}_{i,m} \hat{b}_{j,-m} / \sqrt{2f+1}$ annihilates a pair of bosons at sites i and j

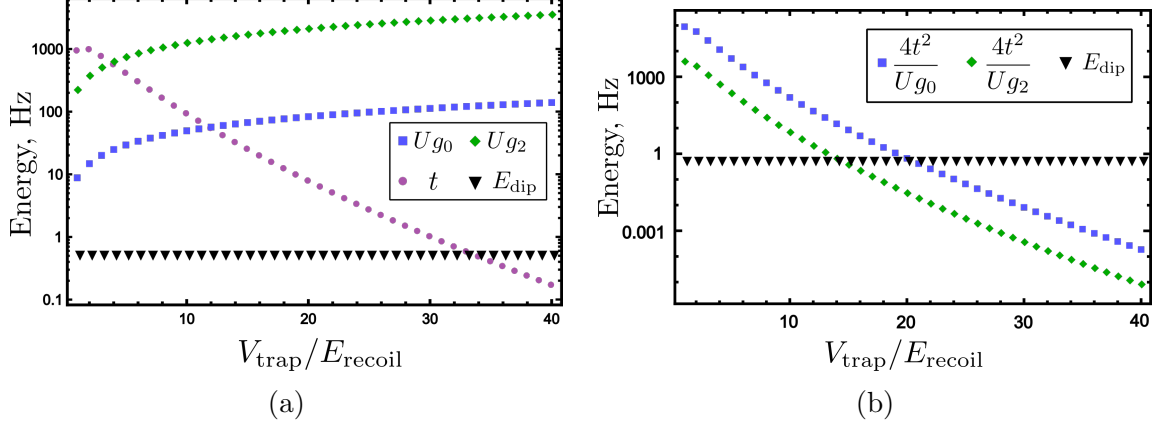


Figure 3.6: Lattice and interaction energies, in the presence of an OFR which tunes the scattering lengths such that $a_0 \sim a_B$. This figure shows (a) the magnitude of t and Ug_F from Eq. 3.14 and (b) the magnitude of the exchange interactions from Eq. 3.19 compared to the DDI as a function of lattice depth for ^{23}Na , with a Feshbach tuning of $\Theta_{\text{Fesh}} = 20$. For Eq. 3.31 to be valid, we require that $Ug_F > t > E_{\text{dip}}$ and $\frac{4t^2}{U_{g_0}} > \frac{4t^2}{U_{g_2}}, E_{\text{dip}}$. From these plots, this region is seen to occur for $V_{\text{trap}}/E_{\text{recoil}} \sim 12\text{--}20$, which is within the range of experimental parameters.

in a hyperfine spin singlet. This Hamiltonian favors the formation of nearest-neighbor singlets, and can lead to quantum spin liquid and resonating valence bond phases, as discussed at length in Chaps. 4 and 5.

Atom	f	$\frac{V_{\text{trap}}}{E_{\text{R}}}$	Θ_{Fesh}	$\frac{g_2}{g_0}$	$\frac{U_{g_0}}{t}$	$\frac{t}{E_{\text{dip}}}$	$\frac{4t^2/U_{g_0}}{E_{\text{dip}}}$
^{23}Na	1	20	65	24.5	10.7	16.3	6.07
^{87}Rb	2	16	45	8.23	8.72	10.85	4.97
^{52}Cr	3	16.5	0.69	30.5	4.52	2.26	2.00

Table 3.4: Ratios of lattice and interaction energy scales for particular lattice depths, with an optical Feshbach resonance tuning the scattering lengths such that $a_0 \sim a_B$. The lattice depths are chosen to satisfy $Ug_F > t > E_{\text{dip}}$ and $\frac{4t^2}{U_{g_0}} > \frac{4t^2}{U_{g_2}}, E_{\text{dip}}$. We see that even in the presence of a strong OFR, it is possible to choose parameters such that our approximations used to obtain Eqs. 3.14, 3.19, and 3.31 remain valid.

Parameter	Symbol	^{23}Na	^{87}Rb
Mass	M	22.99 amu	86.9 amu
Electron spin	s	1/2	1/2
Orbital momentum	l	0	0
Nuclear spin	i	3/2	3/2
Hyperfine spin (possible)	f	1, 2	1, 2
Hyperfine spin (chosen)	f	1	2
Electron magnetic moment	μ_j	1.73 μ_B	
Nuclear magnetic moment	μ_i	2.22 μ_N	2.75 μ_N
Lattice depth	$V_{\text{trap}}/E_{\text{recoil}}$	20	16
Feshbach tuning	Θ_{Fesh}	65	45
Temperature	T	300 pK	
Magnetic field from Earth	B_{Earth}	25×10^{-6} T	

Table 3.5: Experimental parameters used to calculate the lattice and interaction energy scales of Tab. 3.6. The hyperfine spin manifolds are chosen for their stability (see for example the discussion in Ref. [127]). The lattice depth and Feshbach tuning are chosen to satisfy the conditions in Tab. 3.4. The temperature is chosen to be towards the lower bound of achievable temperatures for Mott insulators (see for example Ref. [116]). The upper-bound for any external magnetic fields used in calculations.

3.4 A discussion of relevant energy scales

In this section, we discuss and summarize relevant energy scales for our cold atom system, including possible perturbative effects which have been neglected. Tabs. 2.1 and 3.6 summarize these energy scales and are used as reference throughout this section. In particular, it shows realistic choices of atoms, lattice depth, and Feshbach tuning, for which the derivation of Eqs. 3.19 and 3.31 from Eq. 3.14 remain valid, and for which we believe would take experimentalists closest to a physical realization of the models predicted in Chaps. 4 and 5. The calculation for many of these energy scales is presented in App. A.

Energy Scale	Symbol	²³ Na	⁸⁷ Rb	Source
Electronic Zeeman energy	$\mu_j B_{\text{Earth}}$	606 kHz		Tab. 3.5
SHO frequency	ω_{trap}	294 kHz	69.5 kHz	Eq. A.1
Recoil energy	E_{recoil}	32.8 kHz	8.29 kHz	Eq. A.2
Nuclear Zeeman energy	$\mu_i B_{\text{Earth}}$	423 Hz	524 Hz	Tab. 3.5
Onsite interaction	$U g_0$	435 Hz	119 Hz	Eq. 3.13
Hopping energy	t	17.7 Hz	14.4 Hz	Eq. 3.11
Exchange interaction	$4t^2/U g_0$	24.5 Hz	8.23 Hz	Eqs. 3.13 & 3.11
Thermal energy	$k_b T$	6.25 Hz		Tab. 3.5
Quadratic Zeeman shift	q_{Zeeman}	16.9 Hz	4.36 Hz	Eq. A.3
Nearest-neighbor dipole	E_{dip}	2.22 Hz	1.81 Hz	Eq. A.4
Quadratic AC Stark shift	q_{Stark}	1.4 Hz	0.44 Hz	Eq. A.5
Inelastic scattering rate	Γ_{scatter}	10 mHz	0.5 mHz	Eq. A.6

Table 3.6: Atomic and lattice energy scales for an alkali gas trapped in an optical lattice, in descending order of magnitude. Most parameters used in these calculations are provided in Tabs. 2.1 and 3.5. We point out that the nearest-neighbor DDI and the tensor light shifts from the photoassociation lasers are neglected in our treatment, which is acceptable since they are the smallest energy scales in the problem, and down by almost an order of magnitude from the exchange energy.

In our derivations, we assume that there is no external magnetic field applied to the system. However, for the study of low-energy magnetic phases even the Earth's magnetic field creates a linear Zeeman energy which in some cases is several orders of magnitude larger than the lattice energies. This may be compensated for by applying a slowly varying parabolic Magnetic field across the entire system. This auxiliary field achieves two things. First, its magnitude and direction may be chosen to effectively cancel the Earth's magnetic field for a large region in the center of the trap. Second, at the edges of the trap where the fields no longer cancel, the field gradient acts as an additional confining potential, keeping the atoms centrally located and preventing them from falling out the sides of the optical lattice. However, if we confine our attention to the physics within the center of the trap, then we may neglect the presence of this small and slowly-varying field. Additionally, the quadratic Zeeman shift from the Earth's field is negligible, and will be even more negligible when an auxiliary field is used.

Inelastic scattering of atoms with the optical lattice can result in kinetically hot atoms which escape from the trap. However, for blue detuned lattices of wavelength $\lambda = 530$ nm, we find the scattering rate is $\mathcal{O}(\text{mHz})$, while the lifetime of cold atoms experiments is often 1s or less. Therefore, we expect scattering from the optical lattice play no appreciable role in experimental realizations of our proposal.

A concern specific to the study of large spin gases is the presence of dipole-dipole interactions (DDI), since the magnitude of the dipole energy grows as j^2 , where j is the total electronic angular momentum. The contribution from the nuclear magnetic moment is much smaller and may be neglected. The on-site dipole interaction is absorbed into the background scattering lengths of Tab. 3.2, while the magnitude of the long-range component goes as $|\mathbf{r}_i - \mathbf{r}_j|^{-3}$. We find that the Feshbach tuning scheme which we propose to produce Eq. 3.31 actually increases the strength of exchange interaction relative to the nearest-neighbor dipole-dipole energy.

With these considerations, we anticipate that the most straightforward application of our model is to alkali systems. Those which are readily available for study include $F = 1$ systems of ^{23}Na and ^{87}Rb , $F = 2$ systems of ^{87}Rb . To use even larger spins, experiments involving radioactive isotopes with lifetimes longer than typical experimental cycles are also possible [127]. These include $F = 3$ systems of $^{135,137,139,141}\text{Cs}$, and $F = 4$ systems of ^{119}Cs and $^{207,209,211,213}\text{Fr}$. These gases would allow for increasing the hyperfine spin f , while keeping $j = 1/2$ and therefore a negligible dipole moments. However, we do not rule out the use of atoms with large dipole moments such as $F = 3$ ^{52}Cr or $F = 7, 8$ ^{164}Dy , since techniques for tuning both their scattering lengths [178, 184–189] and their effective DDIs [190–192] have been developed to some extent.

Furthermore, producing a tunable scattering length through optical Feshbach resonance may introduce other perturbative corrections to the effective model of Eq. 3.19. These include inelastic scattering losses and tensor light shifts—both arising from the presence of the photoassociation laser. The inelastic scattering losses may be captured in our model by modifying $U\delta_{\text{PA}} \rightarrow U\delta_{\text{PA}} + i\hbar\Gamma$, where Γ is the natural linewidth of the molecular state. Furthermore, the scattering rate $\Gamma_{\text{scatter}} \propto \Gamma/\delta_{\text{PA}}^2$ [54], and so if the detuning is large compared to the natural linewidth, this type of molecular decay can be neglected. Typical values for the detuning are $\sim\text{GHz}$ while the linewidth ~ 100 MHz [160], and so this condition is met we may safely ignore this effect. However, a drawback of using a large detuning is that to appreciably change the scattering lengths (Eq. 3.29), a high intensity laser is required, and higher-order terms in the AC stark shift—known as tensor light shifts—may be present. However, these have been calculated following Ref. [193] and remain extremely small compared to other relevant energy scales (see Tab. 3.6). These shifts are further minimized if the laser detuning is larger than atomic hyperfine splitting [111]. Finally, there are prospects of tuning these quadratic shifts—including the possibility of cancelling them

completely—through the use of auxiliary microwave fields [193, 194]. Therefore, we do not feel that inelastic scattering or tensor light shifts are needed for an accurate description of our system as a Feshbach-tuned spin model (Eq. 3.19), and that this model captures only the energetically relevant physics in a valid way.

3.5 The phase diagram predicted by spinor mean field theory

We now conclude this chapter by examining the Hamiltonian of interest, Eq. 3.19, using a common variational approach, where the trial states are spinor Bose-Einstein condensate states of various symmetry. This method applies the techniques used for BEC with spin-dependent interactions to a system of spinful bosons on a lattice. In these cases, one assumes that the ground state wavefunction is a product state of the spin states on each site—where the order parameter for the spin on each site is a vector, known as a spinor, which spans the hyperfine projection space. This method is able to capture ferromagnetic, antiferromagnetic, nematic, and higher-order generalizations of the nematic states [104, 145, 195, 196]. However, this method does not capture entangled states such as dimer phases or spin liquids, which are competitive ground states on these lattices [70, 72] and which we show to be present in Chaps. 4 and 5 over a specific range of scattering lengths. However, it is instructive to first determine the nature of the spinor condensates which appear in the absence of these exotic phases, and to help understand the nature of the underlying interactions as a function of scattering length.

We begin with a spinor condensate wavefunction of the form

$$|\psi\rangle = \prod_i \sum_{m_i} \xi_{m_i} \hat{b}_{i,m_i}^\dagger |0\rangle. \quad (3.32)$$

Here, ξ_{m_i} represents the coefficient of each hyperfine component in the single-particle wavefunction. We require that this single-particle wavefunction is normalized, and so we have $\sum_m |\xi_m|^2 = 1$, which will also normalize the entire product state. Using Eq. 3.32 as a variational wave function for Eq. 3.19 gives us a trial energy of

$$E_{\text{var}} = -J \sum_{\langle i,j \rangle} \sum_{F,M} \frac{1}{g_F} \langle \psi | \hat{A}_{i,j}^{\dagger FM} \hat{A}_{i,j}^{FM} | \psi \rangle = -2JN \sum_{F,M} \frac{1}{g_F} |\xi^\dagger \cdot C^{FM} \cdot \xi|^2, \quad (3.33)$$

where $\xi = (\xi_f, \dots, \xi_{-f})^T$ is the spinor order parameter, and is a vector in spin space, while C^{FM} is a matrix in spin space with elements equal to the Clebsch-Gordon Coefficients $C_{m,m'}^{FM} = \langle f, m; f, m' | F, M \rangle$.

In the interest of comparing these results with the results of Chap. 4 we focus on a square lattice—however, generalizations to other lattices are straightforward. Due to the bipartite nature of the square lattice we allow for two different spinors ξ_i and ξ_j on sublattice i and j respectively. Furthermore, we may consider the application of a uniform magnetic field \mathbf{B} directed along the quantization axis (in this case the z -axis), which couples to each spin through a Zeeman term of the form $\hat{H}_{\text{Zeeman}} = -\hat{\mu}_z B = \mu B \hat{S}_z$. While we will not be applying a magnetic field during our study of exotic phases during later chapters, we do so here mainly to provide an additional axis to the phase diagram. With these considerations, we write the variational energy as

$$\frac{E_{\text{var}}}{JN} = -2 \sum_{FM} \frac{1}{g_F} \left| \xi_i^\dagger \cdot C^{FM} \cdot \xi_j \right|^2 - B_{\text{eff}} (\xi_i^\dagger \cdot \hat{S}_z \cdot \xi_i + \xi_j^\dagger \cdot \hat{S}_z \cdot \xi_j), \quad (3.34)$$

where $B_{\text{eff}} \equiv \frac{\mu B}{2J}$. We then minimize Eq. 3.34 with respect to the ξ_i and ξ_j spinors, while maintaining the normalization conditions $|\xi_i|^2 = |\xi_j|^2 = 1$. In doing so we find the variational ground state wavefunction and energy, for which we know sets an upper bound on the true ground state energy ($E_{\text{GS}} \leq E_{\text{var}}$).

We characterize the resulting spinors by calculating the expectation values of spherical tensor operators $\langle \hat{T}^{k,q} \rangle = \xi^\dagger \cdot \hat{T}^{k,q} \cdot \xi$, which at each rank k gives $\langle \hat{T}^k \rangle \equiv$

Spinor phase diagram, $f = 1$

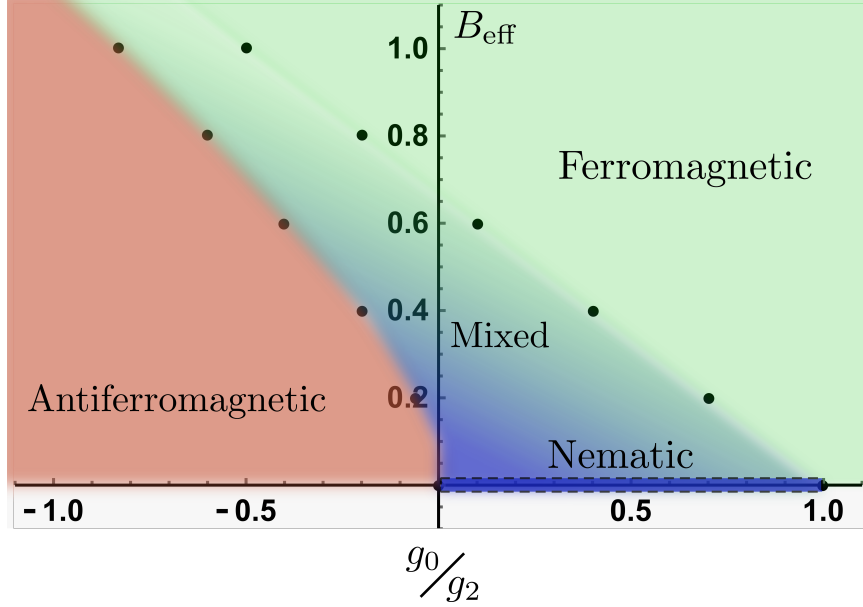


Figure 3.7: Phase diagram for an $f = 1$ spinor condensate (such as ^{23}Na) in an external magnetic field $B_{\text{eff}} = \mu B/2J$. The ratio of the scattering lengths g_0/g_2 and may be tuned with an optical Feshbach resonance as described in Sec. 3.3. For zero magnetic field ($B_{\text{eff}} = 0$) the system is a spin nematic for $g_0/g_2 = (0, 1)$, which corresponds to the spinor condensate ground states found in Chap. 4, while for $g_0/g_2 = (-\infty, 0)$ and $g_0/g_2 = (1, \infty)$ the system is antiferromagnetic and ferromagnetic respectively. The application of a magnetic field expands the ferromagnetic region, and induces a small magnetization in the nematic state which points along the field axis. In this way, the phase contains aspects of both the nematic and ferromagnetic phases, and so we elect to call it the “mixed” phase. However, this phase is not to be confused with the mixed phase of the QDM.

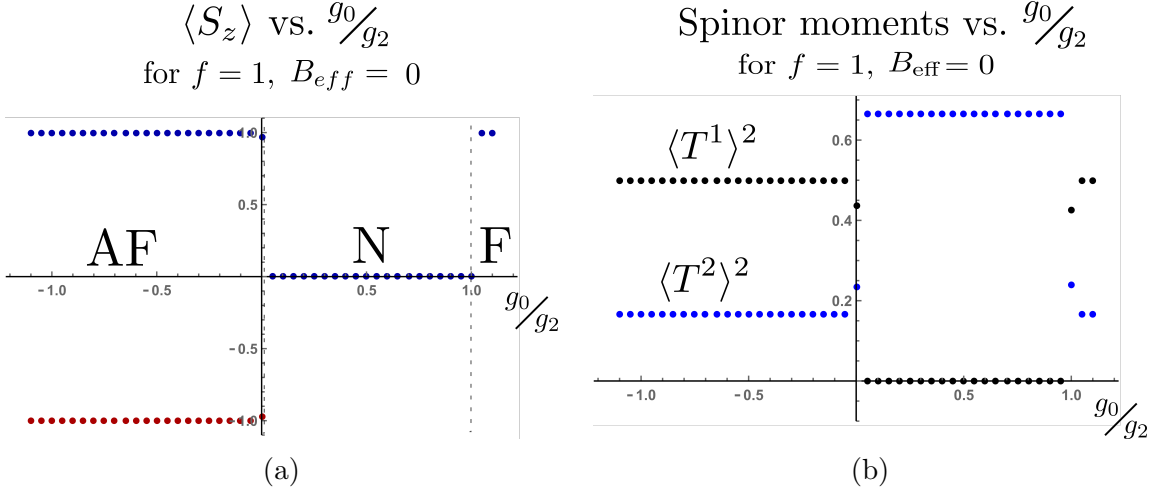


Figure 3.8: Characterization of the spinor wavefunction for $B_{\text{eff}} = 0$. (a) Shows the expectation value of the spin projection along the quantization axis for spins on sublattice i (blue) and j (red). AF, N, and F denote the antiferromagnetic, nematic, and ferromagnetic phases respectively. (b) Shows the expectation values of the $k = 1$ (black) and $k = 2$ (blue) spherical tensor operators. It is seen that for $g_0/g_2 = (0, 1)$, where $\langle \hat{S}_z \rangle = 0$ the $k = 2$ component becomes large, while the $k = 1$ component goes to zero, indicating nematic order in this region.

$\sum_q \langle \hat{T}^{k,q} \rangle^2$. This is equivalent to calculating expectation values of common spin order parameters. For example, the rank-1 spherical tensor \hat{T}^1 contains the same information as the spin vector operator, \hat{S} , while the rank-2 spherical tensors \hat{T}^2 are equivalent to the spin nematic order parameter $\hat{Q}_{a,b} = \hat{S}_a \hat{S}_b + \hat{S}_b \hat{S}_a - \hat{S}^2 \delta_{a,b}$, where $a, b = x, y, z$. The advantage of the spherical tensor operators is that they are much simpler to construct at higher order, which is necessary for the phases at large spin. We may employ this procedure to characterize the spinor condensate phase diagram for Eq. 3.19.

The phase diagram for a spin-1 system is shown in Fig. 3.7. While the features as a function of B_{eff} are interesting, we primarily point out the behavior at $B_{\text{eff}} = 0$ for use in Chap. 4. Namely, when g_0 and g_2 are both positive (as is the case for the alkali atoms discussed throughout this chapter) the possible spinor phases are nematic and ferromagnetic. Since Tab. 3.2 indicates that the background scattering lengths are roughly equal, we begin near the $g_0/g_2 \simeq 1$ point. The OFR discussed in Sec. 3.3 is

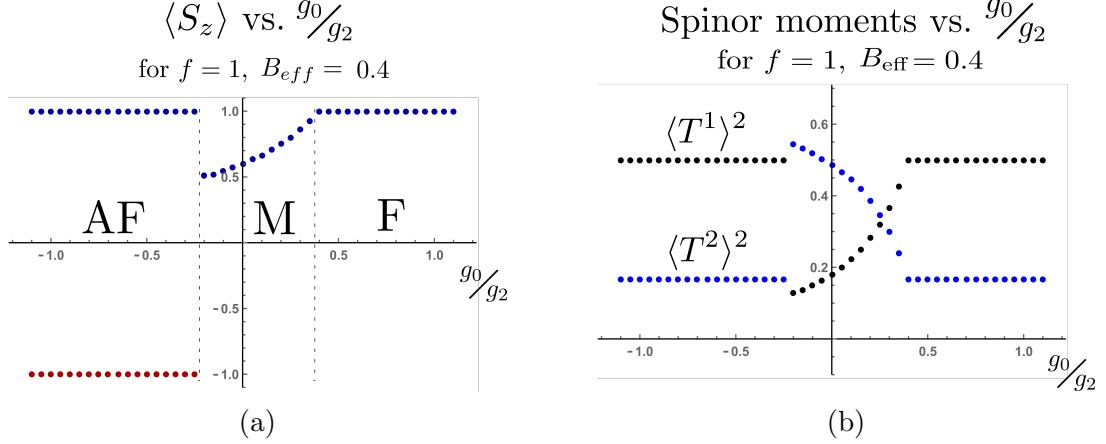


Figure 3.9: Characterization of the spinor wavefunction for $B_{\text{eff}} = 0.4$. (a) Shows the expectation value of the spin projection along the quantization axis for spins on sublattice i (blue) and j (red). AF, M, and F denote the antiferromagnetic, “mixed”, and ferromagnetic phases respectively. (b) Shows the expectation values of the $k = 1$ (black) and $k = 2$ (blue) spherical tensor operators. It is seen that within the mixed phase the $k = 2$ component becomes large, while the $k = 1$ component becomes small, and that both continuously approach their values in the ferromagnetic phase as g_0/g_2 is increased. This indicates that the “mixed” phase is a nematic state which is being biased in the applied field direction, hence the non-zero magnetization but large nematic-character to the spinor in this region.

then used to reduce g_0 relative to the higher- F scattering channels, taking $g_0/g_2 \simeq 0$ in the limit which yields Eq. 3.31. Thus, throughout the entire analysis of Chap. 4 and Chap. 5 the competing spinor condensate phase has nematic symmetry.

Chapter 4: Quantum Spin Liquids

In this chapter, we perform a mean field theory for spin- f bosons on a square optical lattice, tightly confined to the Mott insulating state. We choose to include only the fundamental low-energy scattering interactions [104], described by the set of s-wave scattering lengths, a_F , and tuned via microwave and optical Feshbach resonances [179, 197–199], as outlined for a single-photon OFR in Sec. 3.3. We then show that our model supports the existence of a short-range resonating valence bond ground state, for certain values of g_F and f . Throughout this treatment, we omit the possibility of magnetic dipole-dipole interactions, though we briefly discuss their effects in Sec. 4.5. The results of this chapter indicate that whole-atom exchange may melt magnetic order and stabilize spin liquid phases in Mott insulating large-spin ultracold atoms. Furthermore, these results lead naturally to the description of our system in terms of quantum dimers, which is the subject of Chap. 5. Material supplemental to the contents of this chapter are presented in App. D.

4.1 Spin liquid mean field theory

To solve our Hamiltonian (Eq. 3.19) with mean field theory, we first expand the pairing operators $\hat{A}_{i,j}^{FM}$ about their ground state expectation values $Q_{i,j}^{FM} \equiv \langle \hat{A}_{i,j}^{FM} \rangle$, and then drop terms of second order in the fluctuations $\delta \hat{A}_{i,j}^{FM}$. Here, this is achieved by sending $\hat{A}_{i,j}^{FM} \rightarrow Q_{i,j}^{FM} + \delta \hat{A}_{i,j}^{FM}$, but the result is equivalent to performing a formal Hubbard-Stratonovich transformation on the action \mathcal{S} , as demonstrated in App. C. This process reduces the Hamiltonian to a quadratic form in the $\hat{b}_{i,m}$ operators, and

is given by

$$\hat{H}_{\text{MF}} = - \sum_{\langle i,j \rangle} \sum_{F,M} \frac{J}{\bar{g}_F} (Q_{i,j}^{FM} \hat{A}_{i,j}^{FM\dagger} + Q_{i,j}^{FM*} \hat{A}_{i,j}^{FM} - |Q_{i,j}^{FM}|^2) + \sum_i \lambda_i (\hat{n}_i - 1), \quad (4.1)$$

where $\bar{g}_F = g_F/g_0$ denotes the scattering length of the F channel relative to the singlet channel ($F = 0$). As our interest lies in the translationally invariant states of this Hamiltonian, we consider bond-independent mean fields, such that $Q_{i,j}^{FM} = Q^{FM}$. Furthermore, we only consider monotonically increasing repulsive interactions, such that $g_F > 0$ for all F , and $g_{F'} \geq g_F$ for $F' > F$. This is a reasonable assumption, as g_F increases with F for most alkali atoms [180]. In this case, spin singlets ($F=0$) have the lowest two-particle energy, resulting in the antiferromagnetic interactions needed to form spin liquid states.

The second term of Eq. 4.1, which contains the site- and time-dependent Lagrange multiplier λ_i , is introduced to enforce the one-particle-per-site constraint [20]. This constraint is necessary because \hat{H}_{MF} connects to states outside of the physical one-particle-per-site Hilbert space. We can see this from the non-zero commutator

$$[\hat{H}_{\text{MF}}, \hat{n}_i] = \sum_{FM} \frac{J}{g_F} \sum_{\langle (i)j \rangle} (Q_{ij}^{FM*} \hat{A}_{ij}^{FM} - Q_{ij}^{FM} \hat{A}_{ij}^{FM\dagger}), \quad (4.2)$$

where the number operator $\hat{n}_i = \sum_m \hat{b}_{i,m}^\dagger \hat{b}_{i,m}$ is the total number of bosons on site i , and $\langle (i)j \rangle$ denotes a sum over the Z nearest neighbors j of site i . This nonzero commutation implies that eigenstates of \hat{H}_{MF} are not simultaneously eigenstates of \hat{n}_i with fixed particle number. However, minimizing the mean field energy $E_{\text{MF}} = \langle \hat{H}_{\text{MF}} \rangle$ with respect to λ_i fixes the average particle number to be 1, which we believe is a sufficient first approximation. Fluctuations away from the physical one-particle-per-site Hilbert space are calculated in Subsec. 4.2.4, and will lead us towards a description in terms of a quantum dimer model discussed in Chap. 5. We therefore proceed

with the understanding that the methods of this chapter do not rigorously prove the existence of a spin liquid phase with cold atoms, but are rather used to illustrate the general behavior of the quantum spin fluctuations for large-spin ultracold bosons on a lattice. Particularly, that large-spin bosons have large spin fluctuations, allowing them to overcome the tendency towards condensed magnetic order. Furthermore, that these strong spin fluctuations can be observed through mean field theory, which averages out fluctuations by definition, is quite striking, and indicates just how influential whole-atom exchange can be in determining the ground state of large-spin systems.

We note that our choice of decoupling the $\hat{A}_{i,j}^{FM}$ operators themselves provides more versatility than standard mean field decouplings of Eq. 3.19, which assume a spinor BEC through the use of a vector order parameter [103, 104], or through the single-mode approximation [195], which is known to be invalid for the antiferromagnetic interactions that we exclusively consider in this work [200]. In contrast, our MF decoupled Hamiltonian (Eq. 4.1) allows direct competition between exotic paired states described by the $Q_{i,j}^{FM}$ fields—including spin liquid phases and atomic superconductors with both trivial ($F = 0$ singlet) and non-trivial ($F > 0$) Cooper pairing [201]—and the spinor BEC phases described by the boson field $\langle \hat{b}_{i,m} \rangle$. In this way, our theory may reproduce the results of the well-studied spinor BEC mean field theories over the target parameter space, while also allowing for spin liquid ground states. The outcome of this competition depends fundamentally on the strength of magnetic fluctuations, as a spin liquid state will only appear when sufficiently large spin fluctuations have melted the magnetic order of the spinor condensate phase.

To find the ground state of \hat{H}_{MF} , we solve the self-consistent mean field equations,

$$Q^{FM}(\lambda, Q^{FM}) = \frac{1}{N_{\text{bonds}}} \sum_{\langle i,j \rangle} \langle \hat{A}_{i,j}^{FM} \rangle = \frac{1}{N_{\text{bonds}}} \sum_{\langle i,j \rangle} \sum_{m,n} C_{m,n}^{FM} \langle \hat{b}_{i,m} \hat{b}_{j,n} \rangle \quad (4.3)$$

and

$$n_{\text{avg}}(\lambda, Q^{FM}) = \frac{1}{N_{\text{sites}}} \sum_i \langle \hat{n} \rangle = \frac{1}{N_{\text{sites}}} \sum_{i,m} \langle \hat{b}_{i,m}^\dagger \hat{b}_{i,m} \rangle = 1, \quad (4.4)$$

where we have explicitly indicated the dependence of these quantities on λ and Q^{FM} . In particular, since Q^{FM} is a function of itself (i.e., a transcendental equation) there is no closed-form solution. Rather, these equations must be solved iteratively until self-consistency is reached. This is done by first picking initial values $Q_{(i)}^{FM}$, and then solving for a $\lambda^{(i)}$ which satisfies the constraint, $n_{\text{avg}}(\lambda^{(i)}, Q_{(i)}^{FM}) = 1$. We then calculate a new set $Q_{(i+1)}^{FM}(\lambda^{(i)}, Q_{(i)}^{FM})$, which is used to start the next iteration. When these quantities remain unchanged through several iterations such that $\lambda^{(i)} \simeq \lambda^{(i+1)}$ and $Q_{(i)}^{FM} \simeq Q_{(i+1)}^{FM}$, they have converged to their self-consistent values, and the ground state becomes fully specified. We note that the mean field equations Eq. 4.3 and Eq. 4.4 are equivalent to performing the steepest-descent approximation around the saddle point of the action \mathcal{S} , which is outlined in App. C.

The mean field energy $E_{MF} = \langle \hat{H}_{MF} \rangle$ is determined by taking the expectation value of the Hamiltonian with respect to the self-consistent ground state. The energy per site is then

$$\frac{E_{MF}}{N_{\text{sites}}} = -\gamma \sum_{FM} \frac{J}{g_F} |Q^{FM}|^2 \quad (4.5)$$

where $\gamma = N_{\text{bonds}}/N_{\text{sites}}$ is the ratio of the number of bonds to the number of sites, and is a purely dependent on the lattice geometry. For example, on a square lattice $\gamma = 2$. Although the energy function is unbounded from below, the actual ground state energy is finite, and the self-consistency conditions prevent $|Q^{FM}| \rightarrow \infty$.

While it is possible to allow for spatial variation of the order parameter $Q_{i,j}^{FM}$ and to approach the mean field theory in real space, our target states are translationally invariant. We may therefore take advantage of the imposed translational invariance ($Q_{i,j}^{FM} = Q^{FM}$ and $\lambda_i = \lambda$) by assuming periodic boundary conditions and Fourier transforming Eq. 4.1. We utilize the Fourier transformation (FT)

$\hat{b}_{i,m} = \sum_k \hat{b}_{k,m} e^{ik \cdot R_i} / \sqrt{N}$, where the sum runs over all wavevectors k in the first Brillouin zone (BZ), R_i denotes the Bravais lattice vector of site i , and N is total number of sites in the lattice. We may then write Eq. 4.1 with $Q_{i,j}^{FM} = Q^{FM}$ and $\lambda_i = \lambda$ in reciprocal space as

$$\begin{aligned} \hat{H}_{\text{MF}} = & - \sum_k \sum_{m,m'} \left(\sum_{FM} \frac{\epsilon_k}{g_F} C_{m,m'}^{FM} \left(Q^{FM} \hat{b}_{k,m}^\dagger \hat{b}_{-k,m'}^\dagger + Q^{FM*} \hat{b}_{k,m} \hat{b}_{-k,m'} \right) \dots \right. \\ & \left. \dots + \delta_{m,m'} \frac{\lambda}{2} \left(\hat{b}_{km}^\dagger \hat{b}_{km'} + \hat{b}_{-k,-m}^\dagger \hat{b}_{-k,-m'} \right) \right) + \sum_{FM} \frac{N_{\text{bonds}}}{g_F} |Q^{FM}|^2 - \lambda N_{\text{sites}}, \quad (4.6) \end{aligned}$$

where the details of this transformation are given in App. D.2. We note that the lattice contribution of the FT is $\epsilon_k = \sum_{\langle(i)j\rangle} e^{ik \cdot (R_j - R_i)}$, which for a square lattice with a lattice spacing of unity gives $\epsilon_k = \cos[k_x] + \cos[k_y]$.

The method of solving this self-consistent mean field for a general set of Q^{FM} fields is outlined in App. D.3, and follows the method of SU(N) mean field theories for Heisenberg antiferromagnets [202–213]. These methods decompose a spin-1/2 electron into N flavors of bosonic partons—as is done with slave-particle methods [214]—and in doing so introduce an artificial SU(N) symmetry. The action \mathcal{S} then contains a prefactor of N^{-1} , and so this perturbative analysis becomes exact in the large- N limit. Methods to effectively produce SU(N) magnetism in cold atom systems have been proposed [83, 84], and it has been shown that large-spin fermi gases possess hidden symmetries smaller than SU(N), but larger than SU(2). This is certainly a promising avenue from which to study these systems, and a majority of the community’s focus has been in this area.

Our approach is unique in that we only require physical SU(2) spin-rotational symmetry to be present, as will be shown in Subsec. 4.1.1. Additionally, in the one-particle-per-site Hilbert space, the bosonic $\hat{b}_{i,m}^\dagger$ operators of our theory correspond to physical spin- f atoms. This is in contrast to the mathematically-introduced partons of typical slave-particle MF theories, which do not necessarily carry any physical

significance on their own. This correspondence can greatly assist in the interpretation of observables and operators, when expressed in the boson variables. Quite amazingly, the SU(2) symmetry naturally introduces prefactors of $(2f + 1)^{-1}$, making certain regimes of our theory exact in the large- f limit. The ability for experimentalists to approach this limit by simply using larger-spin atoms is a major motivation for our study.

4.1.1 Symmetry of the mean field Hamiltonian

Before solving our mean field theory for various ansatz, it is instructive to first examine the spin rotational symmetry of the \hat{H}_{MF} (Eq. 4.1) for given set of Q^{FM} fields. This characterization will assist us in determining the symmetry of our mean field phases, by simply inspecting which of the Q^{FM} are zero for a given state. To do so, we write the real-space Hamiltonian Eq. 4.1 in matrix form,

$$\hat{H}_{\text{MF}} = \sum_{\langle i,j \rangle} (\Delta_{m,m'} \hat{b}_{i,m}^\dagger \hat{b}_{j,m'}^\dagger + \text{H.c.}) + \lambda \sum_{i,m} \hat{b}_{i,m}^\dagger \hat{b}_{i,m} + \text{constants}, \quad (4.7)$$

where Δ is a $(2f + 1) \times (2f + 1)$ dimensional with elements

$$\Delta_{m,m'} = - \sum_{FM} Q^{FM} C_{m,m'}^{FM} / g_F.$$

Now we consider a global unitary transformation of the boson operators, $\hat{b}_{i,m} \rightarrow U_{m,m'} \hat{b}_{i,m'}$ and $\hat{b}_{i,m}^\dagger \rightarrow U_{m,m'}^* \hat{b}_{i,m'}^\dagger$. The constraint term $\hat{b}_{i,m}^\dagger \hat{b}_{i,m}$ will be trivially invariant since $U^\dagger U = I$ for a unitary operator, while invariance of the interaction term $\hat{b}_{i,m}^\dagger \hat{b}_{j,m'}^\dagger$ requires that $\Delta = U^\dagger \Delta U^*$. If we consider small transformations parametrized by θ_a then we may Taylor expand the unitary operators to first order, which gives $U = e^{i\theta_a T_a} \rightarrow I + i\theta_a T_a + \mathcal{O}(\theta_a^2)$, where T_a are the Hermitian generators of the transformation (see App. B.3). For example, if we are considering SU(2) spin rotations,

these would be proportional to the spin- f representation of the Pauli spin matrices for the three spatial dimensions. The condition for invariance $\Delta = U^\dagger \Delta U^*$ under an infinitesimal rotation $d\theta_a$ becomes $\Delta T_a + T_a^T \Delta = 0$. By examining which generators satisfy this condition we may determine the symmetry of the Hamiltonian for a given set of mean fields Q^{FM} .

As a result, we find that a completely general set $\{Q^{FM}\}$ breaks all rotational symmetries, and therefore may describe arbitrary symmetry-broken states. For a set which contain only $M = 0$ pairings $\{Q^{F0}\}$, we find the \hat{H}_{MF} is symmetric under rotations about the quantization axis, but no other directions. This set therefore describes spin nematic states (see Sec. 4.3). Finally, a state which contains Q^{00} only has the full $\text{SU}(2)$ spin rotational symmetry of our original Hamiltonian (Eq. 3.19). A Q^{00} -only phase describes a phase of spin singlets (see Sec. 4.2). We find no $\text{SU}(N)$ symmetric points in our parameter space, in contrast to Eq. 3.19, which contains an $\text{SU}(N)$ point when g_F were all equal. However, we again emphasize that enhanced symmetry is not required for our approach, and we believe this to be a significant advantage of our theory.

4.2 The short-ranged resonating valence bond ansatz

To directly uncover a spin liquid phase in our model, Eq. 4.1, we retain only the order parameter of the short-range resonating valence bond (s-RVB) state—namely, an isotropic nearest-neighbor pairing amplitude through the singlet channel—in what we call the s-RVB ansatz. In a pure s-RVB spin liquid state, all $F > 0$ pairing channels have zero amplitude, and the spins exist in an equal superposition of nearest-neighbor singlets. A ground state of this type preserves spin rotational and translational symmetry, making it one of the simplest spin liquid mean field theories possible for this

model. Furthermore, we may reach this s-RVB limit by taking $g_0 \rightarrow 0$ with $g_{F \neq 0}$ fixed, which from Eq. 4.1 we see will result in the Q^{00} pairing term dominating, and a suppression of the higher-order pairings. The ability to access this limit by tuning a single parameter (g_0) is extremely advantageous, and may prove crucial in the eventual realization of this phase experimentally.

We employ the s-RVB ansatz in our formalism explicitly by substituting $\langle \hat{A}_{i,j}^{FM} \rangle = Q^{00} \delta_{F,0}$ in Eq. 4.1, where the bond-independent complex number Q^{00} represents the s-RVB order parameter. Then, by introducing the column vector spinor $\hat{\Psi}_{k,m} = (\hat{b}_{k,m}, \hat{b}_{-k,-m}^\dagger)^T$ we may compactly write the FT Hamiltonian as

$$\hat{H} = \sum_{k,m} \hat{\Psi}_{k,m}^\dagger h_{k,m} \hat{\Psi}_{k,m} - \lambda N_{\text{sites}} \frac{(2f+3)}{2} + \frac{Z N_{\text{sites}} |Q^{00}|^2}{2g_0}, \quad (4.8)$$

where we have defined the 2×2 matrix

$$h_{k,m} = \begin{pmatrix} \lambda/2 & -\epsilon_k Q^{00} C_{m,-m}^{00}/g_0 \\ -\epsilon_k Q^{00} C_{m,-m}^{00}/g_0 & \lambda/2 \end{pmatrix}, \quad (4.9)$$

and where we have fixed the gauge of the bosons $\hat{b}_{i,m} = e^{i\theta} \hat{b}_{i,m}$ such that Q^{00} is real. Again, throughout this chapter we explicitly consider a 2-dimensional square lattice with a lattice spacing of unity, and so $Z = 4$ and $\epsilon_k = \cos[k_x] + \cos[k_y]$. The approach for other lattices follows similarly. In particular, we looked at the triangular lattice, since the geometric frustration of this lattice is known to assist in the formation of spin liquid phases. However, the results on a triangular lattice were qualitatively similar to the square in all cases examined, and are therefore omitted for to avoid redundancy.

In contrast to other methods of studying Eq. 3.19 which focus on a single spin- f at a time [62, 70, 72, 144], our study of the $g_0 \ll g_{F \neq 0}$ limit—which results in the Q^{00} -only Hamiltonian of Eq. 4.8—allows us to fluidly describe systems with different

spin. This feature comes directly from the Clebsch-Gordan coefficients, which appear in Eq. 4.9 due to the physical $SU(2)$ spin rotational symmetry. Essentially, the condition on the CG-coefficients that $C_{m,n}^{FM} = 0$ unless $m + n = M$ implies that the s-RVB state, which requires $M = 0$, retains only terms in which $n = -m$. In other words, the matrix elements of our s-RVB Hamiltonian only ever connect a spin state m with the state of opposite spin polarization $-m$; a fact which leads to the chosen form of the spinor $\Psi_{k,m}^T$ and a single 2×2 matrix representation for the Hamiltonian at all f . Compared to the general Q^{FM} -case of Eq. 4.1, where we would need a $2(2f + 1) \times 2(2f + 1)$ -dimensional matrix at each f , the s-RVB ansatz produces a dramatic mathematical simplification. Additionally, the $C_{m,-m}^{0,0}$ CG-coefficients are of order $(2f + 1)^{-1/2}$, allowing for a perturbative expansion in $1/f$, as described in Subsec. 4.2.2. This makes the Q^{00} -only limit a remarkable limit in which to study the magnetic phases of ultra-cold atoms.

We now seek the ground state of the s-RVB Hamiltonian (Eq. 4.8) in the presence of the one particle-per-site constraint. As outlined in App. D.4, we move to the basis of collective excitations $\hat{\gamma}_{k,\mu}$ by finding a linear transformation $M_{k,m}$ which diagonalizes the matrix $h_{k,m}$ while preserving the bosonic commutation relations, $[\hat{\gamma}_{k,\mu}, \hat{\gamma}_{k',\mu'}^\dagger] = \delta_{k,k'}\delta_{\mu,\mu'}$ and $[\hat{\gamma}_{k,\mu}, \hat{\gamma}_{k',\mu'}] = 0$. We may write this transformation as $\Psi_{k,m} = M_{k,m}\Gamma_{k,m}$, where $\Gamma_{k,m} = (\hat{\gamma}_{k,m}, \hat{\gamma}_{-k,-m}^\dagger)^T$ is the corresponding spinor of quasi-particles. Explicitly, this becomes

$$\begin{pmatrix} \hat{b}_{k,m} \\ \hat{b}_{-k,-m}^\dagger \end{pmatrix} = \begin{pmatrix} U_{k,m} & V_{k,m} \\ V_{-k,-m}^* & U_{-k,-m}^* \end{pmatrix} \begin{pmatrix} \hat{\gamma}_{k,m} \\ \hat{\gamma}_{-k,-m}^\dagger \end{pmatrix}, \quad (4.10)$$

where the Bogoliubov factors $U_{k,m}$ and $V_{k,m}$ are found in App. D.4 to be

$$\begin{aligned} U_{k,m} &= \sqrt{\frac{1}{2} \left(\frac{\lambda/2}{\omega_{k,m}} + 1 \right)} \\ V_{k,m} &= (-1)^m \sqrt{\frac{1}{2} \left(\frac{\lambda/2}{\omega_{k,m}} - 1 \right)}, \end{aligned} \quad (4.11)$$

and obey the condition $|U_{k,m}|^2 - |V_{k,m}|^2 = 1$ to ensure bosonic statistics for the quasiparticles $\hat{\gamma}_{k,m}$. These $\hat{\gamma}_{k,m}$ possess a dispersion $\omega_{k,m}$ given by

$$\omega_{k,m} = \sqrt{(\lambda/2)^2 - |\epsilon_k Q^{00} C_{m,-m}^{00}/g_0|^2}, \quad (4.12)$$

for the band corresponding to magnetic sublevel m , and we note that the m -independence of $|C_{m,-m}^{00}| = 1/\sqrt{2f+1}$ forces complete degeneracy of all $2f+1$ bands. Furthermore, these bands are all dispersive (i.e., no flat bands), which as we will see, leads to maximal fluctuations.

On a square lattice, Eq. 4.12 takes a minimum value at $k = (0,0)$ and $k = (\pi,\pi)$. The value of $\omega_{k,m}$ at these points defines the energy gap $\Delta = \sqrt{(\lambda/2)^2 - 4|Q^{00}/g_0|^2/(2f+1)}$ for the excitations of our system. This gap will play a crucial role in the thermodynamic ground-state analysis to come. We also note that since $\omega_{k,m}$ is symmetric with respect to both k and m , that $U_{k,m}$ and $V_{k,m}$ are real and symmetric in those indices as well—a property used frequently in calculations to follow.

Performing the transformation given by Eq. 4.10 takes us to the quasiparticle basis, where Hamiltonian is written

$$\hat{H}_\gamma = 2 \sum_{k,m} \omega_{k,m} \left(\hat{\gamma}_{k,m}^\dagger \hat{\gamma}_{k,m} + 1/2 \right) + \left(N_{\text{bonds}} \sum_{FM} \frac{|Q_{FM}|^2}{g_F} - N_{\text{sites}} \lambda \left(\frac{2f+3}{2} \right) \right). \quad (4.13)$$

We see that the Hamiltonian is diagonal in this basis, from which it follows that

$[\hat{H}_\gamma, \hat{n}_{k,m}^\gamma] = 0$, and so the quasiparticle numbers are well-defined (conserved) for the eigenstates of \hat{H} . When the gap is non-zero ($\Delta > 0$) the system will minimize the energy by having zero quasiparticles in the ground state, and thus $\gamma_{k,m} |\Psi_{\text{MF}}\rangle = 0$ for all k and m .

4.2.1 Results of the s-RVB ansatz

To determine the self-consistent ground state of the s-RVB Hamiltonian in the thermodynamic limit ($N_{\text{sites}} \rightarrow \infty$) we solve Eqs. 4.3 and 4.4. Expanding in the quasiparticle basis we obtain

$$Q^{00} = \frac{\sqrt{2f+1}}{4} \int \frac{d^2k}{(2\pi)^2} \epsilon_k \sqrt{(\bar{\omega}_{k,m})^{-2} - 1}, \quad (4.14)$$

and

$$\langle \hat{n}_i \rangle = n_\Delta^\gamma + (2f+1) \int \frac{d^2k}{(2\pi)^2} \frac{1 - \bar{\omega}_k^2}{2(\bar{\omega}_k^2 + \bar{\omega}_k)} = 1, \quad (4.15)$$

where we have defined $\bar{\omega}_k = 2\omega_{k,m}/\lambda$ to clean up the notation a bit. Here, n_Δ^γ denotes the occupation of collective excitations in states with energy Δ . With gapped excitations ($\Delta > 0$), we have $n_\Delta^\gamma = 0$.

By numerically solving these constraints (Eqs. 4.14 and 4.15), we find the two scenarios shown in Fig. 4.1. The first occurs for $f \geq 3$, where one may satisfy the constraint with $\Delta > 0$. The gapped excitations imply that the condensate fraction is zero, and so the Q^{00} field characterizes the state completely. It is shown in Subsec. 4.2.5 that in the large- f limit this corresponds to a pure s-RVB spin liquid when projected into the one-particle-per-site Hilbert space. On the other hand, for $f \leq 2$ one cannot satisfy the constraint with a gap, implying $\Delta = 0$ at $k = (0, 0)$ and $k = (\pi, \pi)$. The collective excitations may condense at these points, making $n_\Delta^\gamma \neq 0$ to restore the validity of the constraint. In particular, if $\Delta = 0$ then $U_{k,m}$ and $V_{k,m}$ are undefined and our transformation breaks down. This indicates the presence of a spinor condensate, where one must now describe the state with a set of parameters

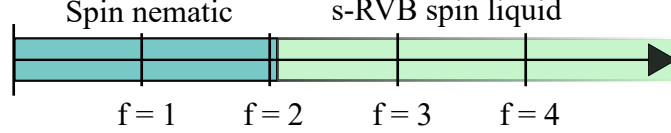


Figure 4.1: Phase diagram of the s-RVB ansatz ($\alpha_{F \neq 0} \rightarrow \infty$) as a function of f . For $f \leq 2$ the ground state is a spin nematic with $\langle \mathbf{S} \rangle = 0$ and $\langle S_x^2 \rangle = \langle S_y^2 \rangle \neq \langle S_z^2 \rangle$ on each site. For $f > 2$, degeneracy of the magnetic sublevels enhances fluctuations, and the ground state becomes a short-range resonating valence bond (s-RVB) spin liquid.

$\langle \hat{b}_{k,m} \rangle$, in addition to the Q^{00} field. A spinor of this type breaks spin rotational symmetry, implying a magnetically ordered ground state for $f \leq 2$. A more thorough description of the condensate symmetry is discussed in Sec. 4.4.

The fact that for small spin we have a magnetically ordered spin nematic ground state, while for large spin we have a disordered spin liquid phase, results directly from the increasing number of magnetic sublevels as one moves to large f . We understand this by noting that the integral in Eq. 4.15,

$$\langle \hat{n}_{i,m} \rangle = \int \frac{d^2k}{(2\pi)^2} \frac{1 - \bar{\omega}_k^2}{2(\bar{\omega}_k^2 + \bar{\omega}_k)} \leq 0.19 \dots,$$

corresponds to the contribution from the non-condensed bosons of the m band, $\langle n_{i,m} \rangle$, and has a maximum value $\simeq 0.19$, which occurs when $\Delta = 0$. Degeneracy of the $2f+1$ bands then implies that for $\Delta > 0$ we can write $\langle \hat{n}_i \rangle < 0.19 * (2f+1)$, and so to satisfy $\langle \hat{n}_i \rangle = 1$ for finite Δ , we must have $f > 2$. Again, we emphasize that the increasing spin-fluctuations in our large-spin states result directly from the increasing number of magnetic sublevels as one moves to larger spin. The enlarged space through which the spins may interact enhances the fluctuations, melting magnetic order and driving the system into an s-RVB spin liquid phase.

4.2.2 The large- f limit

A remarkable feature of the s-RVB ansatz is that it possesses a straightforward expansion in $1/f$. With current experiments able to use atoms with hyperfine spins as

large as $f = 8$ [102], we are hopeful that the $g_0 \ll g_{F \neq 0}$ and large- f limit—where our theory becomes exact—may soon be physically accessible. For this reason, we study several properties directly in the large- f limit, such as the spin fluctuations and ground state wavefunction.

For the quasiparticle dispersion $\omega_{k,m}$, we find to sub-leading order that

$$\omega_{k,m} = \frac{\lambda}{2} \left(1 - \frac{1}{2(2f+1)} \left(\frac{2\epsilon_k Q^{00}}{\lambda} \right)^2 \right) + \mathcal{O} \left(\frac{1}{f^2} \right). \quad (4.16)$$

Similarly, the Bogoliubov factors $U_{k,m}$ and $V_{k,m}$ (defined in Eq. 4.11) become

$$\begin{aligned} U_{k,m} &= 1 + \mathcal{O} \left(\frac{1}{f} \right), \\ V_{k,m} &= \frac{(-1)^m}{\sqrt{2f+1}} \frac{\epsilon_k Q^{00}}{\lambda} + \mathcal{O} \left(\frac{1}{f} \right). \end{aligned} \quad (4.17)$$

We now use these expressions to simplify the self-consistent equations. For the constraint (Eq. 4.15) we find

$$\langle n_i \rangle = (2f+1) \int \frac{d^2k}{(2\pi)^2} \frac{1}{4(2f+1)} \left(\frac{2\epsilon_k Q^{00}}{\lambda} \right)^2 = \frac{Q^2}{\lambda^2} = 1. \quad (4.18)$$

From this we determine that $\lambda = \pm Q^{00}$, but since E_{MF} (Eq. 4.5) is proportional to $|Q^{00}|^2$ we can take $\lambda = +Q^{00}$ without loss of generality. Now looking at Eq. 4.14 we obtain

$$Q^{00} = \frac{Q^{00}}{2\lambda} \int \frac{d^2k}{(2\pi)^2} \epsilon_k^2 = \frac{Q^{00}}{2\lambda} + \mathcal{O} \left(\frac{1}{f} \right), \quad (4.19)$$

from which we can determine that in the large- f limit,

$$\lambda = Q^{00} = \frac{1}{2}, \quad (4.20)$$

which specifies the self-consistent ground state. We may now use this to calculate ground state properties of our system in the large- f limit.

4.2.3 Spin fluctuations in the large- f limit

A primary goal of this study is to explicitly show that quantum spin fluctuations increase as one moves to larger spins. This follows the general argument made by Wu for large-spin fermi gases [68], and is central towards our belief that large-spin bose gases should contain exotic fluctuation-driven many-body phases, such as spin liquids and dimerized valence bond crystals. While this argument can be made from a “cartoon” understanding of the exchange interactions (as described in Fig. 2.18), and is supported by the existence of a mean field spin liquid for large- f , it is worthwhile to calculate the spin uncertainty and verify explicitly that this is the case.

We calculate the spin uncertainty on an arbitrary site i , and in a particular direction $\alpha = x, y, z$, which is given by $\Delta\hat{S}_i^\alpha = \sqrt{\langle(\hat{S}_i^\alpha)^2\rangle - \langle\hat{S}_i^\alpha\rangle^2}$. With Q^{00} -only, the expectation value of each spin component is zero, $\langle\hat{S}_i^\alpha\rangle = 0$, and so we only have to calculate $\langle(\hat{S}_i^\alpha)^2\rangle$. In terms of our boson operators we have

$$\langle(\hat{S}^\alpha)^2\rangle = \sum_{m,m'} \sum_{n,n'} \langle\hat{b}_m^\dagger \hat{S}_{m,m'}^\alpha \hat{b}_{m'} \hat{b}_n^\dagger \hat{S}_{n,n'}^\alpha \hat{b}_n\rangle, \quad (4.21)$$

where we have suppressed the site index i which is common to each operator. Now, we transform to the quasiparticle basis, expand to 2nd order in f^{-1} , and use Eq. 4.20 to determine that the squared-uncertainty of a single spin component is

$$(\Delta S^\alpha)^2 = \frac{1}{2f+1} \left(1 + \frac{1}{2f+1}\right) \sum_{m=-f}^f m^2, \quad (4.22)$$

and is identical for all three spatial components. This quantity is plotted in Fig. 4.2, where we can clearly see that the spin fluctuations grow in the large- f limit. Deviations from the trend for small- f may be ignored, since our expansion is only valid at large- f . Furthermore, we find the total uncertainty relative to the spin magnitude, $\Delta\mathbf{S}/S = \sqrt{(\Delta S_x^2 + \Delta S_y^2 + \Delta S_z^2)/(f(f+1))}$, approaches a constant value

Spin uncertainty vs. quantum number f

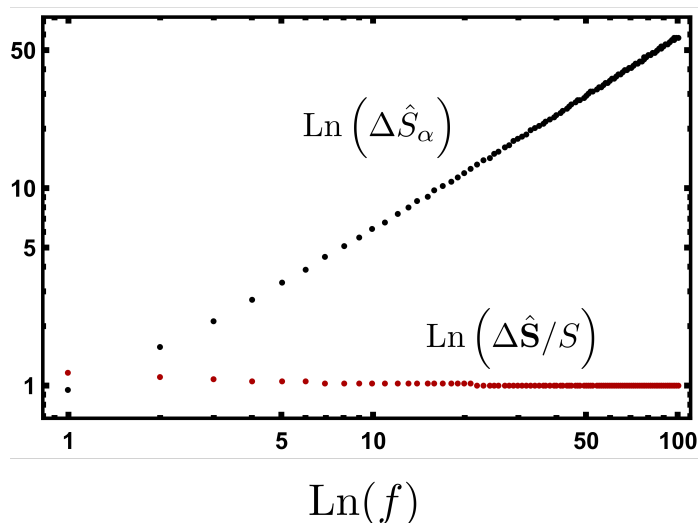


Figure 4.2: Spin uncertainty vs. spin quantum number f on a log-log plot, calculated using the Q^{00} only large- f limit expansion. The uncertainty of each component $\Delta \hat{S}_\alpha$, where $\alpha = \{x, y, z\}$, is given by Eq. 4.21, is seen to grow with increasing spin f . The uncertainty relative to the spin magnitude $S = \sqrt{f(f+1)}$ goes to a constant value of 1, indicating maximum spin uncertainty (and hence quantum fluctuations) in the large- f limit. This is in contrast to solid-state spin models, where electron mediated exchange interactions cause the relative magnitude of the spin fluctuations to decrease with increasing f , and so the spins behave more classically in the large-spin limit.

of 1 in the large- f limit. This indicates that the Q^{00} -only spin liquid phase at large- f possess the maximum possible spin fluctuations.

4.2.4 Fluctuations of the mean fields in the large- f limit

We may also calculate uncertainty of the \hat{A}_{ij}^{00} and \hat{n}_i operators, to test the validity of our mean field approximations. The results will determine whether these operators are well approximated by their average value, and that fluctuations were negligible as we assumed during the mean field decoupling of Sec. 4.1. If the fluctuations of these quantities are zero in the mean field ground state, then there is a reasonable chance that the approximation of static fields was good, and the predicted phases may be stable. On the other hand, if the fluctuations are large in the mean field ground state, then it likely indicates that the system would prefer to be in a different phase, but is

too constrained by the mean field ansatz to relax into the true ground state. In this way, the mean field approximation is able to test its own validity.

For the uncertainty in singlet operator \hat{A}_{ij}^{00} , we find

$$\langle (\hat{A}_{ij}^{00})^2 \rangle - \langle \hat{A}_{ij}^{00} \rangle^2 = \frac{1}{4(2f+1)} + \mathcal{O}(f^{-2}), \quad (4.23)$$

which goes to zero in the large- f limit. We therefore believe that our choice of decoupling through the \hat{A}_{ij}^{00} operators was reasonably correct, and because of that, the large- f behavior of our system is described by states with well defined $\langle \hat{A}_{i,j} \rangle$. This observation motivates a description of Eq. 3.19 where singlet bonds are the fundamental object. This results in a quantum dimer model, as implemented in Chap. 5.

When we look at the fluctuations in the particle number \hat{n}_i , we find

$$\langle \hat{n}_i^2 \rangle - \langle \hat{n}_i \rangle^2 = 1 + \frac{1}{2f+1} + \mathcal{O}(f^{-2}). \quad (4.24)$$

We see that while the fluctuations decrease, they do not completely die out for large f . This indicates that our approximation of a static and uniform Lagrange multiplier $\lambda_i(t) = \lambda$, and of a fixed-phase Q^{00} , is insufficient to properly maintain the one-particle-per-site constraint. While they can enforce the correct density on average, our theory fails to completely suppress density fluctuations. This is due to the broken U(1) phase symmetry of the boson operators in our mean field theory. From Noether's theorem, we know that the continuous U(1) phase symmetry ($\hat{b}_{i,m} \rightarrow e^{-i\phi} \hat{b}_{i,m}$) of our nearest-neighbor spin Hamiltonian (Eq. 3.19), is associated with conservation of boson number. Therefore, by fixing the gauge and breaking this symmetry, we expect to induce fluctuations in the particle number, which Eq. 4.24 confirms.

To more formally treat the constraint we may proceed in several ways—two of which we discuss here. One possibility is to allow phase fluctuations of the Q^{FM} fields

and amplitude fluctuations of λ and formulate a $U(1)$ lattice gauge theory in $2 + 1$ -dimensions [16, 214]. In our case, one may expect to utilize the factors of $(2f + 1)^2$ to expand the bosonic Green functions and all other relevant quantities as a converging series, as is formulated in App. C. Furthermore, on bipartite lattices—such as the square lattice currently under consideration—gauge fluctuations may make the mean field spin liquid phase unstable towards dimerization [16, 20, 208, 215]. Frustrated lattices such as triangular and kagome are more likely to possess stable spin liquid phases [31, 202], and are stronger candidates on which to observe QSL physics in cold atoms. Although, these arguments are made for $S = 1/2$ Heisenberg models, and so a square lattice spin liquid phase with ultracold atoms cannot be ruled on by analogy alone. Especially since additional interactions may be enough to sufficiently frustrate spins on the square lattice, as is the case for the $J_1 - J_2 - J_3$ Heisenberg model [204]. In Chap. 5 we discuss how the higher-order scattering channels ($F = 2, 4, \dots, 2f$) may be used to move our system to the s-RVB point of the quantum dimer model, and so we believe that there may in fact be a multitude of ways to stabilize the square lattice spin liquid predicted by our mean field theory.

While the aforementioned method has its merits, the most straightforward way of enforcing the constraint is to project our mean field ground state wavefunction into the physical one-particle-per-site Hilbert space, via a Gutzwiller projection for bosons [216]. After a discussion of the mean field ground state in the next section, we show that this projection produces an effectively dimerized ground state. Again, we use these results to guide our reformulation of the Hamiltonian for $g_0 \ll g_{F \neq 0}$ into the dimer basis, which we rigorously present in Chap. 5.

4.2.5 The mean field ground state

Now we proceed to calculate the mean field ground state. We require that the ground state is the vacuum of Bogoliubons, and so satisfies

$$\hat{\gamma}_{k,m} |\Psi_{\text{MF}}\rangle = \left(u_{k,m} \hat{b}_{k,m} + v_{k,m} \hat{b}_{-k,-m}^\dagger \right) |\Psi_{\text{MF}}\rangle = 0 \quad , \quad (4.25)$$

for all k and m . We may construct a state which satisfies the relation in Eq. 4.25, and without regards for normalization is given by

$$|\Psi_{\text{MF}}\rangle \propto \text{Exp} \left[- \sum_{k,m} \frac{v_{k,m}}{u_{k,m}} \hat{b}_{k,m}^\dagger \hat{b}_{-k,-m}^\dagger \right] |0\rangle, \quad (4.26)$$

where $|0\rangle$ is the vacuum of atoms. In real space, the exponent may be written as

$$- \sum_{k,m} \frac{v_{k,m}}{u_{k,m}} \hat{b}_{k,m}^\dagger \hat{b}_{-k,-m}^\dagger = \sum_{i,j,m} t_{i,j}^m \hat{b}_{i,m}^\dagger \hat{b}_{j,-m}^\dagger, \quad (4.27)$$

where we define

$$t_{i,j}^m \equiv - \int \frac{d^2 k}{(2\pi)^2} e^{-ik \cdot (r_i - r_j)} \sqrt{\frac{1 - \bar{\omega}_{k,m}}{1 + \bar{\omega}_{k,m}}}. \quad (4.28)$$

We find that t_{ij}^m may link sites which are separated by more than one lattice constant. Therefore, the general ground state involves spin singlets over long-range bonds, the characteristic length of which decreases with f . Furthermore, since these terms appear in the exponent, the ground state will contain terms of all possible particle number $n = 0, 1, 2, \dots, \infty$, as may be seen by expanding the exponential as a series. This property is illustrated in Fig. 4.3a.

The mean field ground state simplifies for large f when using the expansions from

Subsec. 4.2.2. In this limit we find

$$\sum_{i,j,m} t_{ij}^m \hat{b}_{i,m}^\dagger \hat{b}_{j,-m}^\dagger \propto \sum_{\langle i,j \rangle} \hat{A}_{ij}^{00\dagger}. \quad (4.29)$$

The mean field ground state for large f is then

$$|\Psi_{\text{MF}}\rangle \propto \text{Exp} \left[\sum_{\langle i,j \rangle} \hat{A}_{ij}^{00\dagger} \right] |0\rangle. \quad (4.30)$$

This allows us to visualize the ground state, which is shown in Fig. 4.3a. We see that the ground state is a superposition of all possible nearest-neighbor singlet states with even total particle number. To determine the contribution from terms with a chosen total particle number N_{atoms} , we sum over all configurations which contain $N_{\text{atoms}}/2$ spin-singlets on nearest-neighbor bonds.

If we project $|\Psi_{\text{MF}}\rangle$ into the physical one-particle-per-site Hilbert space, we find that in the large- f limit, then $|\Psi_{\text{proj.}}\rangle$ corresponds to an equal amplitude s-RVB. In general however, the we find that $|\Psi_{\text{proj.}}\rangle$ represents a more general RVB spin liquid, which contains long-ranged valence bonds as well. In the following chapter, we will use these factors to motivate the formulation of our theory as a QDM in the large- f limit. However, before moving on to this reformulation, it is instructive to look at what happens to our mean field theory when other scattering channels are allowed.

4.3 The spin nematic ansatz

To better describe the atomic species used in cold atom experiments we must study the most general case \hat{H}_{MF} (see Eq. 4.1), which allows scattering through all total angular momentum channels, $F = 0, 2, \dots, 2f$. However, with all Q^{FM} fields allowed, the increasing size of the interaction space at large f makes the MF Hamiltonian increasingly cumbersome to solve numerically. Specifically, to efficiently probe the

$$\begin{aligned}
|\Psi_{\text{MF}}\rangle = & \begin{array}{c} \bullet \quad \bullet \\ \bullet \quad \bullet \end{array} + \left(\begin{array}{c} \bullet \\ | \\ \bullet \end{array} \begin{array}{c} \bullet \\ | \\ \bullet \end{array} + \begin{array}{c} \bullet \\ | \\ \bullet \end{array} \begin{array}{c} \bullet \\ | \\ \bullet \end{array} + \begin{array}{c} \bullet \quad \bullet \\ \text{---} \\ \bullet \quad \bullet \end{array} + \begin{array}{c} \bullet \quad \bullet \\ \text{---} \\ \bullet \quad \bullet \end{array} \right) \\
& n_{\text{tot}} = 0 \qquad n_{\text{tot}} = 2 \\
+ & \left(\begin{array}{c} \bullet \\ | \\ \bullet \end{array} \begin{array}{c} \bullet \\ | \\ \bullet \end{array} + \begin{array}{c} \bullet \quad \bullet \\ \text{---} \\ \bullet \quad \bullet \end{array} + \begin{array}{c} \bullet \quad \bullet \\ | \\ \bullet \quad \bullet \end{array} + \begin{array}{c} \bullet \quad \bullet \\ | \\ \bullet \quad \bullet \end{array} + \begin{array}{c} \bullet \quad \bullet \\ \text{---} \\ \bullet \quad \bullet \end{array} + \begin{array}{c} \bullet \quad \bullet \\ \text{---} \\ \bullet \quad \bullet \end{array} \right) \\
& n_{\text{tot}} = 4 \\
+ & \left(\begin{array}{c} \bullet \\ | \\ \bullet \end{array} \begin{array}{c} \bullet \\ | \\ \bullet \end{array} + \begin{array}{c} \bullet \\ | \\ \bullet \end{array} \begin{array}{c} \bullet \\ | \\ \bullet \end{array} + \begin{array}{c} \bullet \quad \bullet \\ \text{---} \\ \bullet \quad \bullet \end{array} + \begin{array}{c} \bullet \quad \bullet \\ \text{---} \\ \bullet \quad \bullet \end{array} \right) + \left(\begin{array}{c} \bullet \quad \bullet \\ \text{---} \\ \bullet \quad \bullet \end{array} + \dots \right) \\
& n_{\text{tot}} = 4 \qquad n_{\text{tot}} = 6, 8, \dots
\end{aligned}$$

(a) Mean field ground state, ignoring weights and overall normalization

$$|\Psi_{\text{proj.}}\rangle = \hat{P}(n_i = 1 : \forall i) |\Psi_{\text{MF}}\rangle = \begin{array}{c} \bullet \\ | \\ \bullet \end{array} \begin{array}{c} \bullet \\ | \\ \bullet \end{array} + \begin{array}{c} \bullet \quad \bullet \\ \text{---} \\ \bullet \quad \bullet \end{array}$$

(b) Physical mean field ground state, with one particle per site

Figure 4.3: The mean field ground state is shown in Fig. 4.3a, and the ground state projected onto the physical one-particle-per-site Hilbert space is shown in Fig. 4.3b. Black dots represent sites on a 2×2 lattice. Blue lines represent a singlet between two atoms at sites i and j , created by $\hat{A}_{ij}^{00\dagger}$, and a double bond is created by $(\hat{A}_{ij}^{00\dagger})^2$. Atoms exist only at the end of the bonds, and so a disconnected site is empty, a site which is a part of two bonds has two atoms, etc.

large- f behavior as a function of the scattering lengths a_F , we retain only the order parameter of the spin nematic state, given by $\langle \hat{A}_{i,j}^{FM} \rangle = Q^{F0} \delta_{M,0}$. With this set of mean fields each site will have $\langle \hat{\mathbf{S}} \rangle = 0$ and $\langle \hat{S}_x^2 \rangle = \langle \hat{S}_y^2 \rangle \neq \langle \hat{S}_z^2 \rangle$ —the symmetry of a spin nematic, as seen from Subsec. 4.1.1. Since this ansatz retains only the $M = 0$ pairing, we may write the MF Hamiltonian with the 2-dimensional spinor $\hat{\Psi}_{k,m} = (\hat{b}_{k,m}, \hat{b}_{-k,-m}^\dagger)^T$, as was done in Sec. 4.2. This allows us to diagonalize in a similar way, and the result is to effectively take $Q^{00} C_{m,-m}^{00}/g_0 \rightarrow \sum_F Q^{F0} C_{m,-m}^{F0}/g_F$ in the formulas for $U_{k,m}$ and $V_{k,m}$ from Sec. 4.2.

We motivate this ansatz by extending our results from the s-RVB ansatz, as shown in Fig. 4.1, and by looking to the phase diagram for the spin 1, 2, and 3 spinor Bose-Einstein condensates [62, 71, 103, 104, 144, 154, 217–220], as well our own work from Sec. 3.5. We find that our region of interest, parametrized by $g_F > 0$ for all F and $g_{F'} \geq g_F$ for $F' > F$, lies entirely within the nematic sector of these phase diagrams. Additionally, our ansatz consists of a linear combination of the uniaxial and biaxial spin nematic states (see App. D.5), which are known to possess an accidental degeneracy at mean field level [221, 222]. Thus, it provides a suitable trial state for our specific parameter regime, capable of describing both a nematic spinor condensate and a Q^{00} -only s-RVB spin liquid phase. We note that, in all cases tested, the numerical solutions to the general Q^{FM} mean field theory (see App. D.3) were degenerate with the results of this section. We therefore proceed with this ansatz with the belief that our results describe the physically accessible states of the general Q^{FM} model (Eq. 4.1).

While this approach simplifies the determination of the ground state for a general set of scattering lengths, a difficulty remains in how to best present these results graphically. This is because the number of scattering lengths grows as $f + 1$, which on a phase diagram would require the introduction of an additional axis at each f . To avoid this, we seek an approximation which describes the various scattering lengths

with a single parameter. One possibility is to use the laser intensity Ω , which was introduced in Sec. 3.3, however, this introduces a set of recursive equations to solve at every f , and therefore does not simplify the large- f limit as we intend. Rather, guided by the s-RVB case where we found that $g_0 \rightarrow 0$ favors the singlet pairing and induces an s-RVB spin liquid, we shall use the following approximation for the relative scattering lengths $\bar{g}_F = g_F/g_0$,

$$\bar{g}_F = \begin{cases} \alpha & \text{for } F > 0 \\ 1 & \text{for } F = 0 \end{cases}, \quad (4.31)$$

where scattering lengths through non-zero angular momentum channels have equal magnitude, and differ from g_0 through the proportionality factor α . Varying α from 1 to ∞ covers our original range of the scattering lengths— $g_F > 0$ and $\bar{g}_F \geq 1$ for all F —while the $\alpha \rightarrow \infty$ limit recovers Eq. 4.8 directly. While in real atomic systems the $\bar{g}_{F \neq 0}$ are not generically equal, they effectively appear so when compared to g_0 in the $\alpha \rightarrow \infty$ limit, making this approximation especially useful for describing the spin liquid phase. Most importantly, we may now construct a phase diagram as a function of f and α , since α is a parameter common to all spin f .

We note that applying Eq. 4.31 takes us to an enhanced symmetry point of the original spin Hamiltonian (Eq. 3.19)—namely, the bosonic analog to Wu’s hidden symmetry found in large-spin Fermi gases [119, 223]. Our results do not depend on this symmetry however, and we may show this by using the alternate approximation, $\bar{g}_F = \alpha'F + 1$, where the scattering lengths have a linear relationship with slope α' . This approximation does not generically possess symmetry higher than $SU(2)$, yet the results obtained coincide qualitatively with the results outlined in the next section using Eq. 4.31. The qualitative similarity stems from the fact that in each case, increasing α or α' effectively takes $g_0 \rightarrow 0$, and so the singlet pairing dominates—the

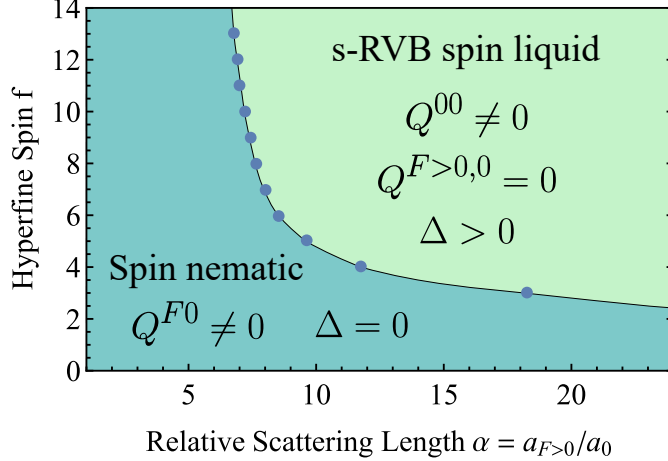


Figure 4.4: Phase diagram on the square lattice of the nematic ansatz as a function of f and α , where $\alpha = g_{F \neq 0}/g_0$ parametrizes the relative scattering lengths, as introduced by Eq. 4.31. The fluctuations responsible for the spin liquid state are enhanced by the increasing number of magnetic sublevels as one moves to large f , and by increased scattering through the singlet channel ($F = 0$) as one moves to large α . For $f \leq 2$ the system is nematic for all α , while for $\alpha = 1$ the spin liquid phase is not accessed at any f . The phase diagram for the triangular lattice is qualitatively similar in that the s-RVB region expands to smaller values of α , but condensate order still occurs for $f \leq 2$ at all interaction strengths.

crucial condition for obtaining a spin liquid phase in this model.

4.3.1 Results of the nematic ansatz

Fig. 4.4 shows the phase diagram for $\alpha = [1, \infty)$ and $f = 1, 2, \dots, 13$. For $f \leq 2$ the system always form a nematic condensate, in agreement with our s-RVB solution in the $\alpha \rightarrow \infty$ limit. On the other hand, for $f > 2$ the system moves into the spin liquid phase for α greater than some critical value α_C . As we move to large f , we find that α_C decreases and the spin liquid region grows in size. Again, decreasing g_0 relative to the other scattering lengths increases α , and so by tuning a single parameter one may access the spin liquid phase for $f > 2$ atoms.

We describe the behavior of the spin liquid region as follows. Increasing α (or α') biases the system towards singlet pairing through Feshbach tuning, which causes equal occupation of the Zeeman sublevels and maximizes magnetic fluctuations. Ad-

ditionally, moving to large f increases the number of available magnetic sublevels, also enhancing fluctuations.[68] The shape of the spin liquid region as shown in Fig. 4.4 results from the cumulative effect of these two scenarios. For $f \leq 2$, too few sublevels contribute to produce the necessary fluctuations, regardless of any tuning towards the singlet channel. With $f > 2$ but still small, the system requires strong tuning to reach the spin liquid phase. While at large f , the multitude of participating sublevels allows access to the spin liquid phase with only a small tuning. In light of this, large-spin atoms such as Dysprosium ($f = 7$) would theoretically require only minimal tuning to obtain the long sought-after spin liquid phase.

4.4 Bose-Einstein condensate ground states

In this section we consider two aspects of the spinor BEC phase, which we find preferred to the s-RVB QSL for small spin and tuning. First, we discuss the scaling of the gap as a function of system size, and how this may determine the behavior of the ground state (being gapped or gapless) in the thermodynamic limit. This is relevant, because the absence of a gap is used throughout this chapter as an indication of magnetic ordering, as well as determining the nature of the fundamental excitations of the system. Second, we discuss which types of magnetic ordering appear in the spinor BEC phase, by analyzing the symmetry of the spinor order parameter.

4.4.1 Behavior of the energy gap in the thermodynamic limit

In the case when $\omega_{k,m} = 0$ for some set of \bar{k} and \bar{m} , then we will have a condensate in the thermodynamic limit ($N \rightarrow \infty$). We can see this by looking at our number constraint term, Eq. 4.15, as discussed in Subsec. 4.2.1. However, some care is needed in taking the thermodynamic limit if the system is headed towards condensation. Specifically, we find that to smoothly approach a BEC in the thermodynamic limit, we

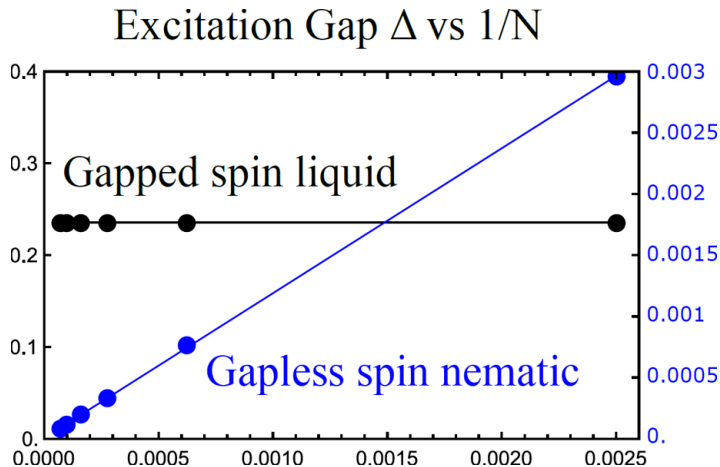


Figure 4.5: The excitation gap as a function of inverse system size. For the spin liquid phase, the gap remains constant as the system is taken to large system sizes. For the spin nematic phase, the gap is roughly 2 orders of magnitude smaller, and decreases in a clear linear trend as the system size is increase. It is therefore clear that the phases are either a gapped spin liquid, or a gapless spinor condensate which possesses nematic symmetry.

must have $(|U_{\vec{k}\vec{m}}|^2 + |V_{\vec{k}\vec{m}}|^2) \simeq N$. Expanding these functions gives the condition that we must have $\bar{\omega}_{\vec{k},\vec{m}} = 2\Delta/\lambda \propto N^{-1}$, such that the gap relative to the bandwidth goes to zero inversely with N . We may understand this from the need to have $\bar{\omega}_{\vec{k},\vec{m}} \rightarrow 0$ as $N \rightarrow \infty$. Mainly, if ω goes faster than $1/N$ then there will be some finite system size for which the gap is zero, and we will have divergent number of particles-per-site. While if it goes slower than $1/N$, there will be a gap in the thermodynamic limit and the constraint equation won't be satisfied. Therefore, we may analyze the behavior of the gap versus the system size to determine if the system will condense in the thermodynamic limit. Furthermore, we can see this behavior clearly in our numerical analysis of the finite-sized Q^{F0} -only system, shown in Fig. 4.5. We also note that λ converges fairly quickly with system size, and so the behavior of $\Delta/\lambda \rightarrow 0$ is from the gap shrinking and not λ growing. This approach was utilized in the determination of the phase diagram of Fig. 4.4.

4.4.2 Symmetry properties of the spinor condensate

There are many ways to determine the symmetry of the condensate, and many ways to include it into the theory—although some are more useful than others. The most straightforward method was presented in Sec. 3.5, where a spinor condensate order parameter is assumed to exist, before the mean field decoupling is applied. From this approach, we find a spin nematic phase over the entire region of parameter space being considered, which agrees with the theoretical and experimental evidence found for spinor gases [62, 71, 103, 104, 144, 154, 217–220]. Another straightforward method is to look at the symmetry of the MF Hamiltonian, as was done in Subsec. 4.1.1. For all cases of finite α , we have a MF ground state described by Q^{F0} fields, which by construction gives rise to a condensate with nematic symmetry.

We may also calculate the expectation values of the spin and nematic tensor operators, and the spin uncertainty. For Q^{F0} states moving towards a condensate in the thermodynamic limit, we find that the z -component has zero uncertainty, while the x and y are each split a half of the total uncertainty. This indicates that there will be magnetic ordering in the thermodynamic limit, as would be the case with well-defined m states. Additionally, the spin expectation value vanishes ($\langle \hat{\mathbf{S}}_i \rangle = 0$), while the nematic tensor operator has non-zero elements ($\langle \hat{\mathcal{N}}_{a,b} \rangle \neq 0$), further indicating of nematic order.

Two methods which are not utilized in this study, but are mentioned for sake of completeness, include utilizing an alternative transformation on the $\hat{b}_{i,m}$ operators, which is well defined for the gapless condensate. This approach is described in Ref. [210] for fermions, and then extended in Ref. [209] to apply to bosons. These cases only consider two flavors of slave particles however, and the approach for $2f + 1$ -flavors of bosons would require a much more complicated transformation in general. Alternatively, we could introduce a condensate order parameter $\langle \hat{b}_{i,m} \rangle$ directly into

the MF Hamiltonian, treat it as an additional self-consistent parameter [48, 202], and solve for it iteratively along with the Q^{FM} and λ . However, introducing additional mean fields—the number of which grows as $2f + 1$ —does not assist us in producing an efficient description of the large- f limit. Therefore, we are content to characterize our state by the presence or absence of an energy gap in the thermodynamic limit, and then by utilizing symmetry arguments or an explicit condensate trial wavefunction to determine the type of condensate present for gapless phases.

4.5 The experimental accessibility of quantum spin liquids

This chapter is now concluded with a discussion of experimental considerations for our proposal. First, we note that the regarding the natural (“un-tuned”) scattering lengths, as compiled in Tab. 3.2 for several commonly used atoms (^{87}Rb and ^{23}Na with $f = 1, 2$, and ^{52}Cr with $f = 3$), we see that a_0 and the next smallest $a_{F \neq 0}$ are roughly the same order of magnitude. For each of these atoms, these natural parameters place them near the $\alpha = 1$ region of Fig. 4.4, and predicts a spin nematic ground state, in agreement with previous theoretical work on these atoms [62, 71, 103, 104, 144, 154, 217–220, 222]. However, upon tuning g_0 to be sufficiently small via optical Feshbach resonance, a transition to the spin liquid phase may occur. We note that this transition may even occur for $f \leq 2$ atoms as well, since fluctuations beyond mean field theory would likely enlarge the spin liquid region.

A potential order parameter for the spin liquid-to-spin nematic phase transition in these systems could be the relative contribution from the $F > 0$ pairing channels, as given by

$$Q_R = \frac{\sum_{F>0} |Q^{F0}|^2}{\sum_{F \geq 0} |Q^{F0}|^2}. \quad (4.32)$$

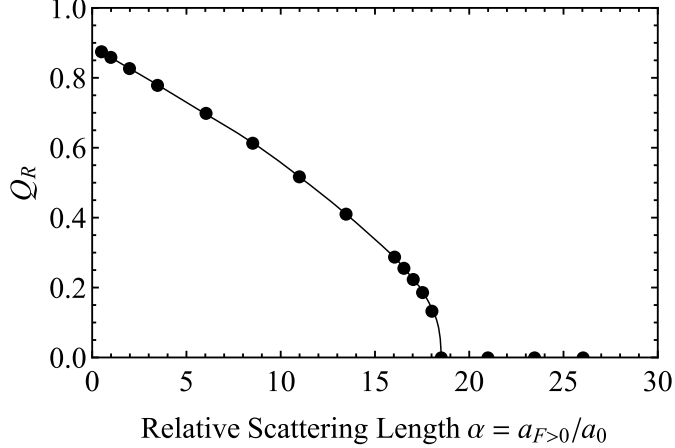


Figure 4.6: Relative contribution from the higher-order scattering channels ($F > 0$) for an $f = 3$ system, as captured by the Q_R parameter defined in Eq. 4.32. In the spin liquid phase ($\alpha \gtrsim 18$) all pairings except the singlet pairing Q^{00} are negligible, while in the spin nematic phase ($\alpha \lesssim 18$) pairing through the non-zero angular momentum channels becomes relevant. Measurement of this parameter could allow observation of the quantum phase transition associated with the tuning of the scattering lengths.

This quantity is similar to the singlet-fraction measured in Ref. [224], and may allow the observation of a spin liquid phase experimentally. Fig. 4.6 shows the behavior of this quantity for an $f = 3$ system when α is tuned, moving the system from spin liquid to spin nematic. Additionally, by spatially resolving vortices in the $Q_{i,j}^{FM}$ fields via photoassociation intensity experiments [148, 181, 182, 225, 226], one may investigate vison excitations in the system, in a similar manner to the vison experiment performed on the high- T_C cuprate superconductors [227]. Overall, the increasingly varied techniques used to prepare and characterize cold atomic systems should provide several avenues by which to observe of these exotic phases.

We note that the interplay between gauge fluctuations and lattice frustration could play a key role when determining the observed phases. This belief originates from studies which go beyond mean field theory, such as those for similar large- N models on square, triangular, and kagome lattices [202, 203]. Particularly, these studies found that on a square lattice, the gauge fluctuations make the spin liquid phase unstable to forming a dimer phase. However, on frustrated lattices such as triangular and

kagome, the spin liquid phase will be stable against these fluctuations. We therefore expect lattice frustration to play a crucial role in the experimental realization of the QSL phase. However, the proximity of the dimer phase to the quantum spin liquid means that even the observation of static dimers, as discussed in Chap. 5, could provide a wealth of information regarding the physics of spin liquid groundstates.

Finally, we expect that the primary challenge remaining in the quest to observe large- f spin liquids will be to overcome the anisotropic dipole-dipole interactions. These interactions grow with the spin as f^2 [228], making them particularly problematic for large spin, where we expect spin liquid phases to be competitive ground states. For example, several recently trapped isotopes of Dysprosium have an extremely large spin of $f = 7$ and 8 , and the DDI in these systems are believed to affect the ground-state physics in a non-perturbative way [102]. Essentially, the dipole-dipole energy sets a lower bound on the allowed tuning of g_0 , below which our approximation breaks down and we must account for these interactions explicitly [192]. Fortunately, for $f = 3$ Chromium, the DDI do not significantly affect the ground-state physics [104], allowing use of our mean field description (Eq. 4.1). Also, recent proposals to tune the dipole-dipole interaction [190], including reducing its effective strength, may hopefully bypass these concerns when using large-spin atoms. However, as presented in Chap. 3 and summarized in Tab. 3.4, for $f = 3$ and below, configurations of lattice parameters and tuning do exist to create an interacting spin system governed by the Hamiltonian Eq. 3.31, without reaching the energy scales of the dipole-dipole interaction. Since the results in this chapter indicate spin liquid behavior for $f > 2$, we suggest that $f = 3$ could provide the optimal balance between large-spin physics and prohibitively large dipole-dipole interactions.

Chapter 5: Quantum Dimer Models

In this chapter, we show that quantum dimer models effectively describe the low-energy interactions of large-spin Mott insulating bosonic atoms in a unit-filled optical lattice, when the spin-dependent interactions are dominated by scattering processes through the spin-singlet channel. After numerically demonstrating nearest-neighbor dimer behavior to the ground state, we derive an effective dimer model on several lattices, discuss the phase diagram of these models, propose a way to explore this phase diagram with our system, and discuss novel measurement techniques only possible in cold atoms which could potentially be used to measure dimer-dimer correlations.

5.1 The singlet basis and the dimer basis

We consider the singlet Hamiltonian from Eq. 3.31, where the Feshbach tunings have been chosen so that only the $F = 0$ scattering channel remains appreciable, and the interaction favors the formation of nearest-neighbor spin singlets. This is given by

$$\hat{H}_{00} = -\frac{J}{g_0} \sum_{\langle ij \rangle} \hat{A}_{ij}^{00\dagger} \hat{A}_{ij}^{00}, \quad (5.1)$$

where as before, $\hat{A}_{ij}^{00} = \sum_m C_{m,-m}^{00} \hat{b}_{i,m} \hat{b}_{j,-m}$ annihilates a pair of bosonic atoms at sites i and j in a hyperfine spin singlet. Throughout this chapter, we often drop the superscripts which denote the total spin variables F and M since they are now both zero, and refer to this pair operator simply as \hat{A}_{ij} . Additionally, we will make

frequent use of the commutation relation

$$\left[\hat{A}_{ij}, \hat{A}_{ij'}^\dagger \right] = \delta_{jj'} \left(1 + \frac{\hat{n}_i + \hat{n}_j}{2f + 1} \right) + \frac{1 - \delta_{jj'}}{2f + 1} \sum_m \hat{b}_{j',-m}^\dagger \hat{b}_{j,m}$$

to calculate expectation values and other operator products. Also, we note that in the one-particle-per-site Hilbert space and in the large- f limit this reduces to bosonic commutation relations $[\hat{A}_{i,j}, \hat{A}_{k,l}^\dagger] = \delta_{i,j} \delta_{k,l}$, and so the \hat{A} singlet pair operators are a convenient fundamental object to work with in this limit. We therefore seek to describe the entire Hilbert space in terms of singlet pairs.

The eigenstates of Eq. 5.1 can be written as a superposition of singlet coverings, with each singlet covering being constructed from the pair operators \hat{A}_{ij} . When acting on the empty state, the $\hat{A}_{i,j}$ operator creates a state where the bosons on sites i and j are paired in a spin singlet, which we may denote as $|i-j\rangle \equiv \hat{A}_{i,j} |0\rangle$. These sites do not necessarily have to be nearest neighbors. The full set of singlet coverings are the states given by

$$|a\rangle = \prod_{(i,j) \in a} \hat{A}_{ij}^\dagger |0\rangle, \quad (5.2)$$

where each lattice site appears exactly once in the product over bonds. This Hilbert space contains no states with unpaired spins (monomers), or multi-paired spins (trimers). Some examples of singlet coverings are and how they are related to the $\hat{A}_{i,j}$ operator are illustrated in Fig. 5.1, and typically, the pictorial representations of these states are more convenient than listing out the paired sites explicitly.

To be used as a valid Hilbert space, the space of singlet coverings must be closed under the operation of \hat{H} . We can see this directly by using the commutation relations (Eq. 5.1) to calculate how terms from \hat{H}_{00} of the form $\hat{A}_{ij}^\dagger \hat{A}_{ij}$ act on states in the

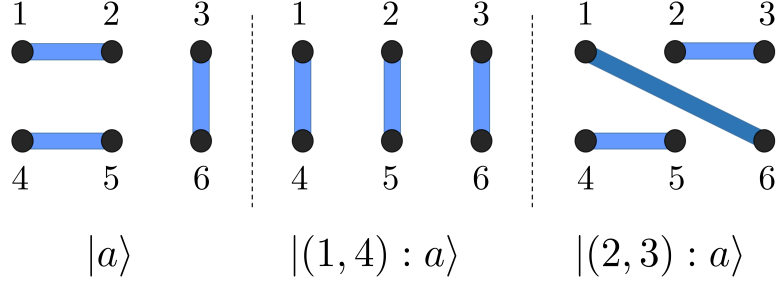


Figure 5.1: Examples of singlet cover states. The numbers label the lattice sites, while connected sites represent a spin singlet between the atoms on those sites. In this example, $|a\rangle = \hat{A}_{1,2}^\dagger \hat{A}_{4,5}^\dagger \hat{A}_{3,6}^\dagger |0\rangle$. The notation $|(i, j) : a\rangle$ denotes a state where sites i and j are paired in a singlet, the original partners of i and j in $|a\rangle$ are paired in another singlet, and all the other bonds in $|a\rangle$ are left unchanged. This notation is used in the supplementary materials to derive an effective dimer model (Eq. 5.18).

singlet covering space. We find

$$\begin{aligned}
 A_{i,j}^\dagger A_{i,j} |i-j; i'-j'\rangle &= |i-j; i'-j'\rangle \\
 A_{i,j}^\dagger A_{i,j} |i-i'; j-j'\rangle &= \frac{1}{2f+1} |i-j; i'-j'\rangle,
 \end{aligned}
 \tag{5.3}$$

and so if sites i and j are already paired then nothing happens, while if i and j are initially unpaired this operator pairs them, and then pairs their old partners i' and j' . The Clebsch-Gordan coefficients from the commutation relations give this process an amplitude of $(2f+1)^{-1}$. When extended to general states in the Hilbert space $|a\rangle$ we write

$$\hat{A}_{ij}^\dagger \hat{A}_{ij} |a\rangle = \begin{cases} |a\rangle, & \text{for } (i, j) \in a \\ (2f+1)^{-1} |(i, j) : a\rangle, & \text{for } (i, j) \notin a, \end{cases}
 \tag{5.4}$$

where the we have introduced the notation $|(i, j) : a\rangle$ to denote a state in which i and j are paired, and the original partners of i and j from $|a\rangle$ are paired, while all the other bonds in $|a\rangle$ are left unchanged. An example of a singlet covering $|a\rangle$ and a few of the related states $|(i, j) : a\rangle$ are illustrated in Fig. 5.1.

A difficulty of using the singlet coverings as defined in Eq. 5.2 is that they are

not orthogonal. Their overlap matrix $S_{a,b} = \langle a|b \rangle$ may be calculated directly with the commutation relations Eq. 5.1, or through their so-called transition graph, as shown in Fig. 5.2. We find that the overlap between two singlet coverings $|a\rangle$ and $|b\rangle$ is

$$S_{ab} = (2f + 1)^{N_{\text{loops}}} \left(\frac{1}{\sqrt{2f + 1}} \right)^{L_{\text{loops}}}, \quad (5.5)$$

where N_{loops} is the total number of closed loops in the transition graph formed by the dimers not common to $|a\rangle$ and $|b\rangle$, while L_{loops} is the total number of sites involved in all loops. This overlap matrix element is pictorially represented by a transition graph, shown in Fig. 5.2. For large f , we may expand S_{ab} in powers of $(2f + 1)^{-1}$ to obtain

$$S_{ab} = \delta_{ab} + \frac{\square_{ab}}{2f + 1} + \frac{\square_{ab}^{(2)}}{(2f + 1)^2} + \mathcal{O}(f^{-3}). \quad (5.6)$$

Here, $\square_{ab} = 1$ if $|a\rangle$ and $|b\rangle$ differ by a 4-site loop in their transition graph, and is zero otherwise. The symbol $\square_{ab}^{(2)} = 1$ if $|a\rangle$ and $|b\rangle$ differ by either a single 6-site loop, or two distinct 4-site loops in their transition graph, and is zero otherwise.

Despite derivations of QDM for spin-1/2 Heisenberg models in solid state systems, clear valence-bond crystal order or short-ranged RVB behavior have not been experimentally observed in these systems. We believe that non-orthogonality plays an role in this apparent discrepancy between theory and experiment. Typically, it is argued that since any two randomly chosen coverings likely have long loops in their transition graphs, that these singlet coverings can just be taken to be orthogonal. However, the ground states of these models are typically described by a superposition of very similar states, which have small loops and therefore large overlaps between them. Other times, an expansion similar to Eq. 5.6 is used, and they neglect higher order terms despite $(2f + 1)^{-1} = 1/2$ not being small. We feel that since the singlet states arising from cold atoms become truly orthogonal in the $f \rightarrow \infty$ limit, that these systems are much more likely to physically realize the predictions of these models, even at large

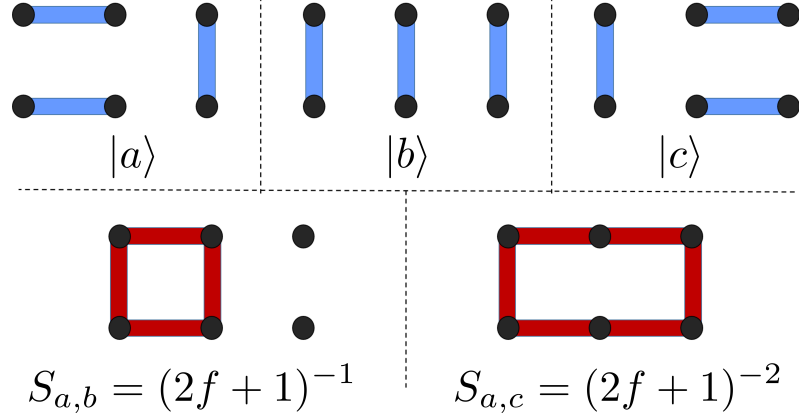


Figure 5.2: Examples of transition graphs between non-orthogonal singlet coverings. The magnitude of the overlap is given by Eq. 5.5 and is shown in the figure for the two cases. The overlap S_{ab} comes from a single 4-site loop, and represents the largest possible overlap in magnitude. The overlap S_{ac} comes from a single 6-site loop, and is down in magnitude by a factor of $(2f + 1)^{-1}$. In the large- f limit, all singlet coverings become orthogonal as the overlaps approach zero.

but finite f .

To construct an orthogonal basis set from the non-orthogonal singlet coverings, we could generally use the Gram-Schmidt procedure, however, this procedure is typically impractical for large sets of abstract vectors, especially since each vector is treated uniquely in the procedure. Rather, as pointed out by Ref. [42], there turns out to be a much simpler way to construct an orthogonal basis from the singlet coverings, and it applies uniformly to all basis vectors, making it much easier to write down in a general way.

We first note that the overlap matrix from Eq. 5.6 is real, symmetric, and positive definite (meaning all the eigenvalues are real and positive, and hence it is invertible). These conditions imply that there is a unique matrix $S^{1/2}$ called the principle square root, such that $S = S^{1/2}S^{1/2}$. The principle square root is also positive definite and invertible, which means that $S^{1/2}$ and its inverse $S^{-1/2}$ can be expanded as a series in $(2f + 1)^{-1}$. We now use $S^{-1/2}$ to construct from the singlet basis $|a\rangle$ an orthogonal

$$\text{Diagram} = \text{Diagram} - \frac{1}{2(2f+1)} \left(\text{Diagram} + \text{Diagram} + \text{Diagram} \right) + \mathcal{O}(f^{-2})$$

Figure 5.3: Pictorial representation of an orthogonal dimer state constructed from non-orthogonal singlet coverings, as expressed in Eq. 5.7. A dimer state $|\bar{a}\rangle$ has an associated $\mathcal{O}(1)$ singlet covering $|a\rangle$, which is used to label the state. At $\mathcal{O}(f^{-1})$ and higher, it contains contributions from all coverings $|b\rangle$ which differ from $|a\rangle$ by a 4-site loop in their transition graph, including those which lie outside the nearest-neighbor-only Hilbert space.

basis $|\bar{a}\rangle$, defined

$$|\bar{a}\rangle = \sum_b (S^{-1/2})_{a,b} |b\rangle, \quad (5.7)$$

which we call the dimer basis. States in the dimer basis $|\bar{a}\rangle$ are orthonormal, which can be seen directly by calculating $\langle \bar{a} | \bar{b} \rangle = (S^{-1/2} . S . S^{-1/2})_{a,b} = \delta_{a,b}$.

While the transformation from physical singlet pairings to an orthonormal basis set may seem abstract, we can see that the states in many ways retain their character, and are still most readily imagined in terms of the pictorial representation of singlet pairs. We see this by expanding $|\bar{a}\rangle$ for large f to obtain

$$|\bar{a}\rangle = |a\rangle - \sum_b \left(\frac{\square_{ab}}{2(2f+1)} + \frac{\square_{ab}^{(2)}}{2(2f+1)^2} - \frac{3}{8(2f+1)^2} \sum_c \square_{ac} \square_{cb} \right) |b\rangle + \mathcal{O}(f^{-3}), \quad (5.8)$$

to 2nd order. We see that a given dimer state contains an $\mathcal{O}(1)$ contribution from a particular singlet covering, which we may use to label the dimer state. In fact, in the $f \rightarrow \infty$ limit $|\bar{a}\rangle = |a\rangle$, and so the labelling is one-to-one and the deformation from the singlet set is continuous as f becomes finite. This allows us to think of dimer states in almost exactly the same way as we were thinking of the physical spin-singlet coverings. Higher-order contributions come from singlet coverings which differ from the labeling cover by successively longer loops in their transition graph. A pictorial example of singlet covers being used to construct an orthogonal dimer state is shown to first order in Fig. 5.3.

Since our Hamiltonian is defined in terms of its action on the singlet states, as in

Eq. 5.4, we may write this as

$$\hat{H} |a\rangle = \sum_b h_{a,b} |b\rangle, \quad (5.9)$$

where the matrix $h_{a,b}$ relates vectors in this non-orthogonal space under the action of \hat{H} . In terms of the orthogonal basis, we find $\langle \bar{a} | \hat{H} | \bar{b} \rangle = H_{a,b} = (S^{-1/2} \cdot h \cdot S^{1/2})_{a,b}$, such that the eigenvalues of $H_{a,b}$ and $h_{a,b}$ are identical, and that the eigenvectors can be transformed between bases with $S_{a,b}$. This equivalence allows us to find the ground state in either basis, depending on which is convenient. For numerical diagonalization, the non-orthogonal basis is simpler, while for the application of formal perturbation theory, the orthogonal basis is much more transparent. In the following sections we utilize both approaches where they are most convenient.

5.2 Exact diagonalization with small systems

Now that we have defined the singlet and dimer Hilbert spaces, we find the ground state of Eq. 3.31 numerically. For this calculation, we utilize the non-orthogonal singlet basis, since the action of the singlet Hamiltonian on these basis states is known from Eq. 5.4, and so we may calculate $h_{a,b}$ from Eq. 5.9 in a straightforward manner. We seek to show that the ground state of this Hamiltonian lies in the nearest-neighbor-only subspace, and that the ground state possess dimer-like correlations.

In our numerics, we do not rely on the large- f approximation, nor do we restrict ourselves to states with only nearest-neighbor dimer bonds. However, we limited ourselves to a small systems with no more than 16 lattice sites. By exact diagonalization of $h_{a,b}$, as constructed from the \hat{H}_{00} , we compute the ground state and the dimer-dimer correlation functions $\langle \hat{A}_{ij}^\dagger \hat{A}_{ij} \hat{A}_{kl}^\dagger \hat{A}_{kl} \rangle$, which are used extensively to characterize the ground state of QDMs on various lattices [47, 229–231]. Furthermore, in Sec. 5.6 we propose a method of directly imaging singlet bonds to calculate these correlations

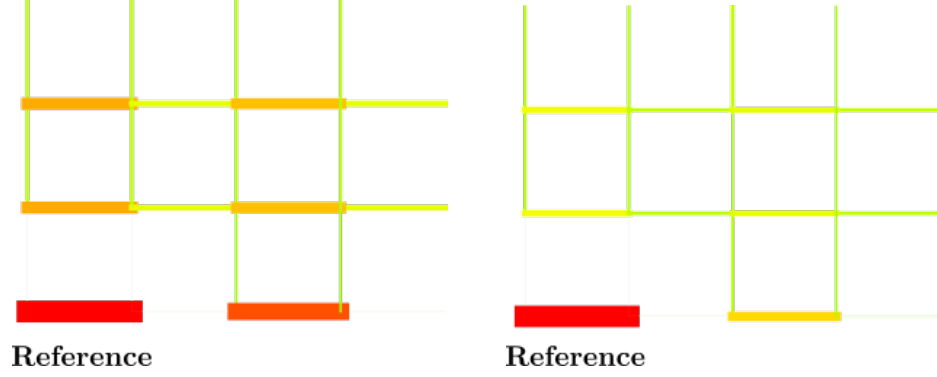


Figure 5.4: Dimer-dimer correlations on a square lattice with periodic boundary conditions. The thicknesses of each bond represents the probability of measuring a dimer on that bond, relative to the reference dimer. (a) The large- f limit, with $f = 100$, shows a mixing of the columnar and plaquette orders. (b) For accessible spin values, such as $f = 3$ shown, the correlations weaken, but remain mixed.

in real space. Here, we calculate the ground state dimer-dimer correlations for a 4×4 square.

Fig. 5.4 shows the calculated correlations between a bond (i, j) and a bond (k, l) on a square lattice for two different values of f , where the bond (i, j) is fixed, and the bond (k, l) is varied. For large f we find correlations which appear to be a mixture of the columnar and plaquette phases. For $f = 3$, which corresponds to the typical atomic species ^{52}Cr , the correlations are weaker but still indicative of a mixed columnar/plaquette phase.

We may look at the excitation energy as a function of spin very simply using these numerical techniques, which is shown in Fig. 5.5. We may also investigate the stability of our system against small perturbations, such as off-site dipole-dipole interactions. We calculate the matrix element of this perturbation V_{01} between the grounds state and first excited state. Using parameters appropriate for Rubidium, we find $V_{01} \sim 0.008$ Hz, which is small compared to the lowest energy plaquette-flip excitation $\sim 0.9J/g_0 \sim 4.5$ Hz.

Excitation energy vs. spin- f

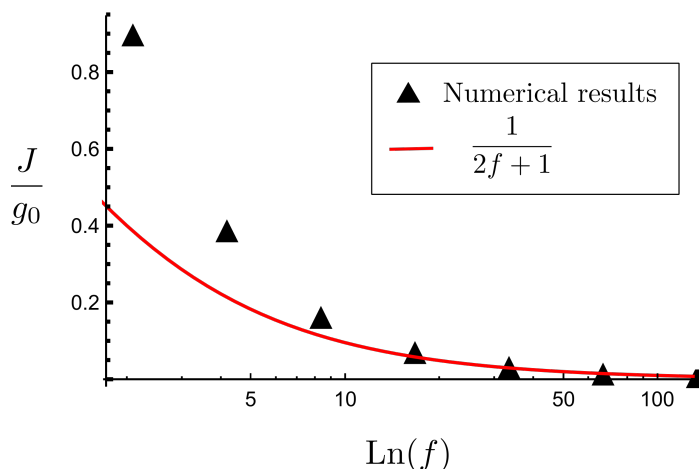


Figure 5.5: Excitation energy as a function of the spin f . We find that the energy gap decreases as $(2f + 1)^{-1}$ in the large- f limit. For the experimentally accessible spins ($f = 1, \dots, 8$) we find the excitation energy ranges between roughly 0.16–0.9 (J/g_0). For an $f = 2$ system of ^{87}Rb , we may use Tab. 3.6 to determine that $\Delta E \simeq 0.9J/g_0 \simeq 7.5$ Hz. In this case, the nearest-neighbor DDI of $\sim 1.8\text{Hz}$ does *not* take the system outside of the nearest-neighbor dimer subspace spanned by our QDM.

5.3 Deriving a quantum dimer model for ultracold bosons

The numerical calculations indicate nearest-neighbor dimer correlations to the ground state of our singlet Hamiltonian (Eq. 5.1), however, at this point we are unsure if this result holds for larger system sizes, and we have no information regarding the parameters of the model, or exactly what types of dimer dynamics occur. To answer these questions we seek an effective description of our Hamiltonian in the nearest-neighbor only sector of the Hilbert space.

We follow the method of Raleigh-Schrödinger perturbation theory described in App. E. First, we define a bare Hamiltonian \hat{H}_0 which contains the nearest-neighbor only dimer subspace as the low energy sector, and of which we know the eigenvalues of in the whole dimer space. Then, we define our perturbing interaction \hat{V} which takes

us out of the nearest-neighbor sector. \hat{V} should be scaled by some small parameter, to justify a truncation of the perturbative expansion to some reasonable order. Finally, we derive an effective Hamiltonian \hat{H}_{QDM} which acts only in the nearest-neighbor subspace.

To formally define the nearest-neighbor only sector we introduce the operator \hat{N}_{nn} , which counts the number of nearest-neighbor in a state $\hat{N}_{nn} |\bar{a}\rangle = N_a |\bar{a}\rangle$, where N_a is the number of nearest-neighbor dimers in dimer covering $|a\rangle$. This may range from $N_a = 0$ for a state with completely long-range dimers, to $N_a = N/2$ for a state in the nearest-neighbor-only subspace. Here, N is the number of lattice sites in the system, and $N/2$ is the maximum since each site is paired, and each pair contains two distinct sites. Using this \hat{N}_{nn} operator, we trivially rewrite the Hamiltonian in Eq. 5.1 as

$$\frac{\hat{H}}{J/g_0} = -\hat{N}_{nn} - \left(\sum_{\langle ij \rangle} \hat{A}_{ij}^\dagger \hat{A}_{ij} - \hat{N}_{nn} \right), \quad (5.10)$$

where we take the first term, $\hat{H}_0 = -\hat{N}_{nn}$, to be our unperturbed Hamiltonian. This term is diagonal in the entire dimer basis, and its completely degenerate low-energy eigenspace is spanned by the set of all nearest-neighbor-only dimer coverings with eigenvalue of $-N/2$. This low-energy subspace is separated from all higher-energy subspaces by at least J/g_0 . Also, since all states in our subspace are degenerate, we will subtract $-N/2$ from the final result since it is just a constant, making $\hat{H}_{\text{eff}} = \hat{V}_{\text{eff}}$.

The second term in Eq. 5.10 is our perturbation, $\hat{V} = - \left(\sum_{\langle ij \rangle} \hat{A}_{ij}^\dagger \hat{A}_{ij} - \hat{N}_{nn} \right)$, which has matrix elements of $\mathcal{O}(f^{-1})$, as will be illustrated shortly. We use completely degenerate perturbation theory to expand \hat{V} as a series in $(2f+1)^{-1}$, restricted to the low-energy subspace of nearest-neighbor-only dimer coverings. We obtain

$$\hat{H}_{\text{eff}} = \sum_{ab} |\bar{a}\rangle \langle \bar{b}| \left(\langle \bar{a} | \hat{V} | \bar{b} \rangle + \sum_c \left\langle \bar{a} \left| \frac{\hat{V}}{\hat{N}_{nn} - N/2} \right| \bar{c} \right\rangle \langle \bar{c} | \hat{V} | \bar{b} \rangle \right). \quad (5.11)$$

Here, $|\bar{a}\rangle$ and $|\bar{b}\rangle$ lie in the nearest-neighbor-only subspace, while $|\bar{c}\rangle$ lies in the higher-energy subspace, and contains at least one long-ranged dimer. The matrix element for \hat{V} between any two dimer states $|\bar{a}\rangle$ and $|\bar{b}\rangle$ is given by

$$\langle \bar{a} | \hat{V} | \bar{b} \rangle = N_b \delta_{ab} - \sum_{d,e} (S^{-1/2})_{ae} \left(N_d S_{de} + \frac{1}{2f+1} \sum_{\langle ij \rangle \notin d} S_{e,(ij):d} \right) (S^{-1/2})_{db}, \quad (5.12)$$

where d and e include all dimer states, and $\langle ij \rangle \notin d$ indicates a sum over all empty bonds, i.e. nearest-neighbor pairs from state d which do not together form a dimer.

Substituting Eqs. 5.6 and 5.12 into Eq. 5.11 and restoring the factor J/g_0 , we find that the matrix elements of the effective Hamiltonian in the nearest-neighbor subspace are

$$\hat{H}_{a,b} = \frac{J}{g_0} \left(-\frac{1}{2f+1} \sum_{\langle ij \rangle \notin b} \delta_{a,(ij):b} - \frac{1}{(2f+1)^2} \sum_c \sum_{\langle ij \rangle \notin c} \sum_{\langle i'j' \rangle \notin b} \delta_{a,(ij):c} \delta_{c,(i'j'):b} \right), \quad (5.13)$$

to second order in $(2f+1)^{-1}$. This is an extremely general result, independent of the system size, the lattice geometry, and boundary conditions of the problem. However, in this form it may not be exactly clear how this model relates to the traditional QDMs, but as the following section will show, when put onto specific lattices, the familiar quantum dimer dynamics emerge.

5.4 The quantum dimer model on different lattices

To simplify Eq. 5.13 further, and to determine the coefficients t , t' , and v which appear in Tab. 5.2, we must evaluate explicitly for different lattices, to express each term using the lengths of loops in the transition graphs between two states. In this section we focus on a square lattice, but a similar procedure can be done for other lattices as well. Pictorial examples of these terms are shown in Tab. 5.1.

For a square lattice, the first term from Eq. 5.13 becomes

$$\sum_{\langle i,j \rangle \notin b} \delta_{a,(i,j):b} = 2\Box_{a,b}. \quad (5.14)$$

This says that $|\bar{a}\rangle$ must be related to $|\bar{b}\rangle$ by applying the $\hat{A}_{i,j}^\dagger \hat{A}_{i,j}$ operator to an empty bond in $|\bar{b}\rangle$. If the empty bond in $|\bar{b}\rangle$ corresponds to the open side of a flippable plaquette, as illustrated in Tab. 5.1, then the plaquette will be flipped and so $|\bar{a}\rangle$ must be a state related to $|\bar{b}\rangle$ by a 4-site loop in the transition graph, and the term is equal to 2 (since there are two empty bonds on each flippable plaquette and the sum $\sum_{\langle i,j \rangle \notin b}$ is over all empty bonds). If the empty bond in $|\bar{b}\rangle$ is not the open side of a plaquette, then $|(i,j) : \bar{b}\rangle$ will contain a long-range bond, and therefore cannot be equal to $|\bar{a}\rangle$, and so the term gives zero. Therefore, the behavior of this term is captured by the symbol $\Box_{a,b}$, defined in Sec. 5.1.

The second order term from Eq. 5.13 is a bit more complicated to simplify. This term comes from second order processes which takes the system out of the nearest-neighbor Hilbert space and then back into it, through two applications of $\hat{A}_{i,j}^\dagger \hat{A}_{i,j}$ operators for two different bonds. There are two scenarios which produce non-zero matrix elements. These result in

$$\sum_{c \notin n} \sum_{\langle i,j \rangle \notin c} \sum_{\langle i',j' \rangle \notin b} \delta_{a,(i,j):c} \delta_{c,(i',j'):b} = \begin{cases} 2(N_{- -} + N_{- \cdot} + N_{\cdot -}), & \text{for } a = b \\ 4\Box_{a,b}, & \text{for } a \neq b. \end{cases} \quad (5.15)$$

The first case $a = b$ is shown in Tab. 5.1. In these cases, the $\hat{A}_{i,j}^\dagger \hat{A}_{i,j}$ acts on an empty bond which is not part of a flippable plaquette. This results in the creation of a single long-range bond in the intermediate state $|\bar{c}\rangle$. Then, we require that the second $\hat{A}_{i,j}^\dagger \hat{A}_{i,j}$ acts on an empty bond in $|\bar{c}\rangle$ and returns it to the original state. The numbers $N_{- -}$, $N_{- \cdot}$, and $N_{\cdot -}$ count how many times these three types of empty bonds which contribute to these processes appear in the dimer covering. For example,

	$ b\rangle$	$ c\rangle$	$ a\rangle$	Multiplicity
t		N/A		2
t'				4
V			$ b\rangle$	2
V			$ b\rangle$	2
V			$ b\rangle$	2

Table 5.1: Pictorial derivation of the t and t' terms of the quantum dimer model on a square lattice. Blue lines indicate dimer bonds, while yellow lines indicate the empty bonds which $\hat{A}^\dagger \hat{A}$ act upon to move the system from $|b\rangle$ to $|c\rangle$ to $|a\rangle$. The multiplicity is the total number of terms in the Hamiltonian which produce identical dimer resonances, and is the product of the number of yellow lines in one single row. The kinetic resonances result in $t : 2\beta \square_{a,b}$ and $t' : 4\beta^2 \square \square_{a,b}$, while, the effective potential becomes $V : 2\beta^2(N_{--} + N_{-|} + N_{-}) \propto -4\beta^2 N_{\text{flip}} \delta_{a,b}$.

$N_{_ _}$ counts the number of empty bonds which are sandwiched between two parallel dimers, all along the same line. Additionally, all possible rotations and reflections of these patterns are considered to be counted, so for example, $N_{_ _}$ also counts all vertical arrangements of this type. Tab. 5.1 shows that there are two ways each of these processes occur, and so we include a factor of two. The second case, when $a \neq b$, (term t'), and comes from a similar process, except that now the final state is a nearest-neighbor-only that differs from the original state by a 6-site loop in the transition graph, which may be represented $\square\square_{a,b}$ as defined in Sec. 5.1. In this case, there are 2 ways of getting into the intermediate state, and 2 ways of getting back, resulting in a factor of 4.

Before substituting these terms back into Eq. 5.13, we make use of the relation $N_{\text{empty}} = N_{_ _} + N_{_ _} + N_{_ _} + N_{_ _}$, where $N_{_ _}$ is the number of empty bonds which are part of a flippable plaquette, and N_{empty} is the total number of empty bonds. These four types of empty bonds are the only types allowed on the square lattice, and so the sum of them is simply the total number of empty bonds. Furthermore, $N_{\text{empty}} = (N_{\text{bonds}} - N_{nn}) = (2N - N/2) = \frac{3}{2}N$ and is constant for the nearest-neighbor only subspace. Finally, each flippable plaquette contains 2 empty bonds, so $N_{_ _} = 2N_{\text{flip}}$. With these considerations we find that we may write

$$N_{_ _} + N_{_ _} + N_{_ _} = \frac{3}{2}N - 2N_{\text{flip}}, \quad (5.16)$$

which by putting things in terms of N_{flip} allows for easy identification of the traditional quantum dimer terms.

Using Eqs. 5.14, 5.15, and 5.16 we now rewrite the quantum dimer Hamiltonian (Eq. 5.13), on the square lattice as

$$\hat{H}_{a,b} = \frac{J}{g_0} \left(-\frac{2}{2f+1} \square_{ab} - \frac{4}{(2f+1)^2} \square\square_{ab} + \frac{4}{(2f+1)^2} N_{\text{flip}} \delta_{ab} \right), \quad (5.17)$$

where we have dropped the constant factor depending on N . The first term—containing \square_{ab} —gives the two-bond resonance term with an amplitude $t = \frac{2}{2f+1} \frac{J}{g_0}$. The second term—containing $\square\square_{ab}$ —gives the three-bond resonance term with an amplitude $t' = \frac{4}{(2f+1)^2} \frac{J}{g_0}$. While the third term—containing $N_{\text{flip}}\delta_{ab}$ —gives an effective interaction $V = \frac{4}{(2f+1)^2} \frac{J}{g_0}$ between the two parallel bonds around a flippable four-site plaquette. We can then put in into the standard notation,

$$\hat{H}_{\text{QDM}} = \sum_{\text{plaquettes}} \left[-t \left(\left| \begin{array}{c} \text{---} \\ \text{---} \end{array} \right\rangle \langle \text{---} \text{---} | + \text{H.c.} \right) + V \left(\left| \begin{array}{c} \text{---} \\ \text{---} \end{array} \right\rangle \langle \text{---} \text{---} | + \left| \text{---} \text{---} \right\rangle \langle \text{---} \text{---} | \right) \right] \\ + t' \sum_{\text{6-site plaquettes}} \left[\left| \begin{array}{c} \text{---} \\ \text{---} \\ \text{---} \end{array} \right\rangle \langle \text{---} \text{---} \text{---} | + \left| \begin{array}{c} \text{---} \\ \text{---} \\ \text{---} \end{array} \right\rangle \langle \text{---} \text{---} \text{---} | + \text{H.c.} \right]. \quad (5.18)$$

where first sum now runs over all 4-site plaquettes, and the second sum runs over all 6-site plaquettes. In this notation t and t' represent the kinetic dimer resonances, while the V term represents the interaction energy between parallel bonds.

We then use the procedure outlined in this chapter to calculate a similar effective model on different lattice geometries, where the amplitudes of the various terms (t , t' , and V) are given in Tab. 5.2. The ground state of these QDMs strongly depends on the lattice geometry. For example, on a triangular lattice we find from Sec. 5.2 the $\sqrt{12} \times \sqrt{12}$, as in Ref. [229]. However, the ground states for the 2D square and 3D cubic lattices are in general a matter of contention [48, 231, 232], which an experimental realization of our proposal could resolve.

5.5 The phase diagram of the quantum dimer model

The effective model for our system from Eq. 5.18 has a rich phase diagram, which has been well explored along $t' = 0$ in a number of geometries [43, 44, 47, 48, 229–237].

Lattice geometry	$\frac{t}{J/g_0}$	$\frac{V}{J/g_0}$	$\frac{t'}{J/g_0}$	Large-f ground state
Square	$\frac{2}{2f+1}$	$\frac{4}{(2f+1)^2}$	$\frac{4}{(2f+1)^2}$	columnar/mixed
Triangular	$\frac{4(f+1)}{(2f+1)^2}$	$\frac{4}{(2f+1)^2}$	$\frac{4}{(2f+1)^2}$	$\sqrt{12} \times \sqrt{12}$
Honeycomb	$\mathcal{O}(1/f^4)$	$\mathcal{O}(1/f^4)$	$\frac{6}{(2f+1)^2}$	plaquette
Kagome	$\mathcal{O}(1/f^4)$	$\mathcal{O}(1/f^4)$	$\frac{6}{(2f+1)^2}$	

Table 5.2: Coefficients of the quantum dimer model on different lattice geometries, determined from the method demonstrated pictorially for a square lattice in Tabs. 5.1 and 5.1. The large-f ground states on square and triangular lattices are determined by numerical diagonalization as discussed in section 5.2. The appearance of the second-order, three bond resonance t' is unique to the quantum dimer model as derived from the singlet Hamiltonian, Eq. 5.1.

For 2D bipartite lattices with $t' = 0$, one finds only valence bond solid phases, while on 3D and non-bipartite 2D lattices dimer liquids may be found. The phase diagram at finite t' is less explored [238].

Expanding our singlet Hamiltonian into the nearest-neighbor dimer basis (Eq. 5.18) has the tremendous advantage of reducing the size of our Hilbert space. This allows us to easily diagonalize the model for small system sizes. In particular, we seek to show that the energies and ground states obtained agree with those predicted by the numerical approach, and to determine where the experimentally realizable phases lie with respect to the complete phase diagram. The results are shown in Fig. 5.6 for a 4×4 square lattice.

From Fig. 5.6 we see that that increasing f only samples a small portion of the complete phase diagram. In particular, the RK point ($v/t = 1$), where the equal superposition RVB wavefunction is the ground state, appears to be inaccessible. However, we expect that by tuning the Feshbach parameters, one could explore a larger region of the model's phase diagram. If we tune the coupling and detuning such that $g_{F \neq 0,2} \gg g_2 > g_0 \gg J$, then the effective spin Hamiltonian at second order

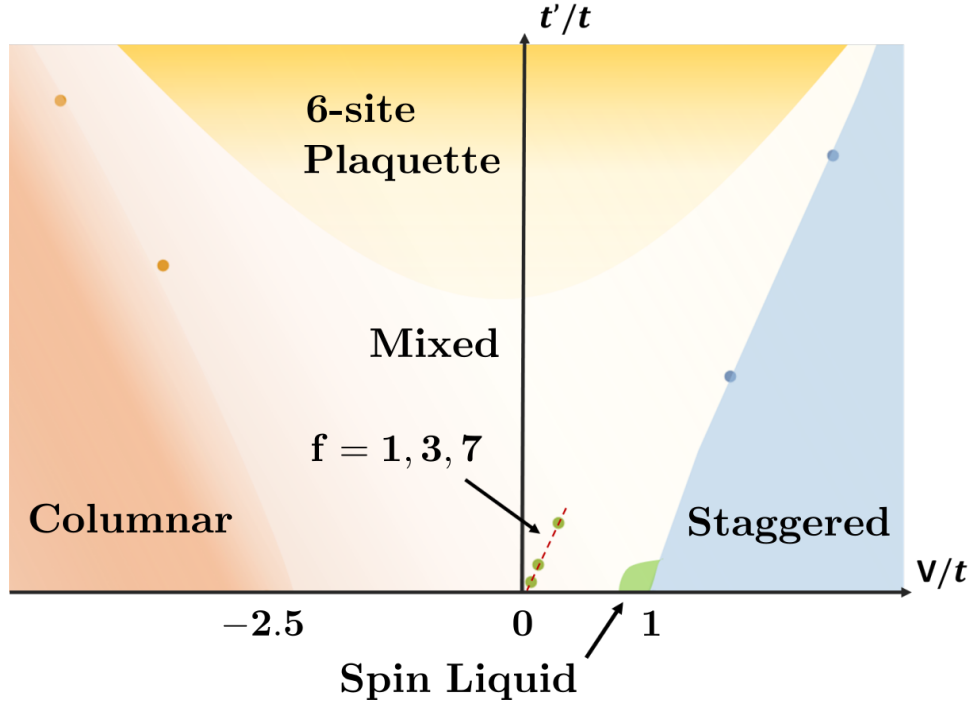


Figure 5.6: The phase diagram for the quantum dimer model on a 4×4 square lattice, obtained by exact diagonalization of Eq. 5.18. We find columnar and staggered phases as shown in Fig. 2.10, as well as a mixed phase which contains components of both the columnar and plaquette phase. We discover that the region accessible by using atoms of different hyperfine spin f lies along a line approaching $V/t = 0$ as $f \rightarrow \infty$. Notably, the RK point at $V/t = 1$ is not accessed directly by increasing the spin. Furthermore, we find that the presence of the unique 3-bond resonance t' widens the disordered region between the columnar and staggered phases by increasing dimer fluctuations, induces a 6-site plaquette phase at large t' , which is not present in QDMs derived from electron superexchange. The dimer-dimer correlations used to distinguish these phases are shown in Figs. 5.7 and 5.8.

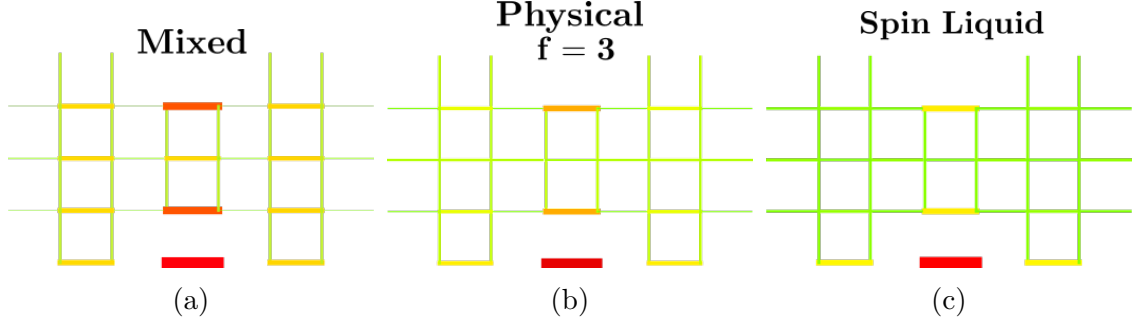


Figure 5.7: Dimer-dimer correlations for three phases of the quantum dimer model on a 4×4 square lattice with periodic boundary conditions (Eq. 5.18 and Fig. 5.6). Reflection symmetry is utilized to enhance the readability of these correlations, by doubling the visual size of the lattice in each figure. (a) The “mixed” phase contains a linear superposition of the columnar and 4-site plaquette phases. (b) The physical state realized by using $f = 3$ atoms (^{52}Cr for example) contains weak correlations which fall off rapidly with distance, and we note good agreement with the numerical results shown in Fig. 5.4. (c) The RVB spin liquid phase is located at the RK point ($V/t = 1$ and $t' = 0$), and shows static correlations beyond nearest-neighbors, as all possible dimer coverings are present in the superposition.

in the tunneling strength is

$$\hat{H} = -\frac{J}{g_0} \sum_{\langle ij \rangle} \hat{A}_{ij}^{00\dagger} \hat{A}_{ij}^{00} - \frac{J}{g_2} \sum_{\langle ij \rangle M} \hat{A}_{ij}^{2M\dagger} \hat{A}_{ij}^{2M}, \quad (5.19)$$

where $\hat{A}_{ij}^{2M\dagger} = \sum_m C_{m, M-m}^{2M} \hat{b}_{i,m} \hat{b}_{j, M-m}$ creates a neighboring boson pair with total spin $F = 2$ and azimuthal spin M . By applying the same large- f perturbation techniques, we expect to obtain a dimer model (Eq. 5.18), where V and t' now depend on $(g_2 - g_0)^{-1}$. The amplitude t could also develop corrections at $\mathcal{O}(f^{-2})$. By tuning $g_2 - g_0$ via the Feshbach laser intensity and detuning, we expect that V/t and t'/t could be controlled to move the system into different regions of the phase diagram.

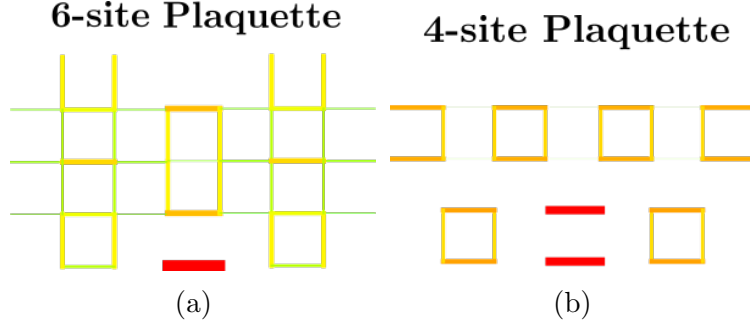


Figure 5.8: Dimer-dimer correlations for the plaquette phases of the quantum dimer model on a 4×4 square lattice with periodic boundary conditions (Eq. 5.18). (a) Due to the presence of a non-zero 3-bond resonance ($t' \neq 0$) we find a 6-site plaquette phase, which is unique to the QDM as derived from whole-atom exchange. (b) The 4-site plaquette phase found with QDMs derived from electron superexchange is not found in our model, but is present as a component in the mixed phase.

5.6 The experimental accessibility of the quantum dimer model

We consider a gas of atoms, with electronic orbital angular momentum, $l = 0$, relatively large hyperfine spin f , but relatively weak dipole-dipole interactions. Alkali metals such as ^{87}Rb with $f = 2$, or ^{40}K with $f = 9/2$ are ideal. Large spin atoms such as ^{52}Cr with $f = 3$ or ^{164}Dy with $f = 8$ could be used if the DDI was tuned to be small. To image the singlet bonds we propose shining a weak near-resonant photoassociation laser on the system, tuned near a molecular state with angular momenta $L = 1$ and $S = 0$. Then, when virtual hopping brings two atoms forming an $S = 0, L = 0$ dimer onto the same lattice site, the near-resonant light drives these atoms into the molecular state. The excited molecule has a short lifetime and so those atoms are lost from the trap. The probability of losing adjacent atoms which do not form a dimer is proportional to $\frac{1}{(2f+1)^2}$, and so at large f , adjacent atoms which do not form a dimer have a much smaller probability of being lost in this manner. In light of this, we propose to image the system with a quantum gas microscope [239, 240], after the gas has been probed with the photoassociation laser.

From these images the fraction of dimer bonds in the system can be determined, since all empty sites in the image were likely occupied by atoms previously entangled in a dimer. Dimer-dimer correlations could then be extracted by analyzing data from multiple realizations of this imaging process. We emphasize that the ability to directly image the valence-bond correlations is one of the greatest strengths of this system, and will allow unambiguous identification of the various valence-bond ordered phases. Spin liquid phases will be characterized by the absence of long-range valence bond order.

Chapter 6: Conclusions

In this thesis, we have developed a proposal to use ultracold gases trapped in optical lattices to study quantum spin liquid phases and quantum dimer models. This study was motivated by the nature of the whole-atom exchange mechanism present in these systems, which allows for magnetic spin fluctuations which grow with the magnitude of the constituent spins through the increasing number of Zeeman sublevels, $(2f + 1)$. This mechanism, along with several other properties unique to cold atoms, provides numerous advantages compared to similar studies derived from solid state spin models. These include experimental control over the magnitude of spin fluctuations and the ability to tune the interaction strengths through different scattering channels.

To investigate the possibility of a cold atomic spin liquid, we considered an isotropic mean field theory which captures the competition between a spin liquid and magnetically ordered Bose-Einstein condensates. With this approach we determined that a gapped spin liquid phase is favored for large spin ($f > 2$) and small singlet scattering ($a_0 \ll a_{F \neq 0}$). It also remarkably produced an analytic solution in the case of ($a_0 \rightarrow 0$), which allowed us to derive the field ground state wavefunction in a closed form. We observed that although spin fluctuations increase, the amplitude of nearest-neighbor singlet pairing becomes static in the large-spin limit, leading to the recasting of our problem in terms of a quantum dimer model.

We then rigorously derived the quantum dimer model for a system of ultracold bosons to second order in f^{-1} using Rayleigh-Schödinger perturbation theory. This mapping becomes exact in the $f \rightarrow \infty$ limit, and the possibility of physically accessing the large- f limit through judicious choice of atoms gives our approach an advantage

over QDMs derived from the Heisenberg model. We also find the appearance of an additional kinetic 3-bond (6-site) resonance, which is absent in solid state QDMs. When this resonance is large, we find new QDM ground states, such as the 6-site plaquette phase. Since the ground state of the traditional QDM is unknown in certain parameter regimes, a cold atom QDM system could be used to experimentally resolve these theoretical questions. Finally, we anticipate that the ease at which cold atomic systems can be created with different geometries provides a significant incentive to engineer these phases using cold atoms. For example, by stabilizing a QDM or QSL phase on a topologically non-trivial lattice—such as a disk with a hole in the center, or a torus—one can envision using these systems to create and manipulate fractionalized excitations in a quantum computer someday.

To conclude, Mott insulating ultracold bosonic systems provide a rich environment in which to study, and someday create, quantum dimer models and spin liquid phases. The theoretical study of such phases has been critical in developing our understanding of how constraints lead to new emergent physics, and they have been used as a theoretical foundation when attempting to understand phenomena ranging from high-temperature superconductivity to quantum computing. The physical realization of QDMs and QSLs using ultracold atoms, as proposed in this thesis, would revolutionize our understanding of exotic magnetic phases, and would further shape the landscape of condensed matter physics in the post-Landau era. As the experimental manipulation of large-spin atoms in optical lattices steadily improves, we believe it is only a matter of time before the elusive spin liquid phase may finally be captured.

Appendix A: Calculations of atomic and lattice energy scales

This appendix collects several formula used to calculate various atomic and lattice energy scales, used to produce Tab. 3.6. Primarily, it provides the trapping frequency ω_{trap} in Eq. A.1, the recoil energy E_{recoil} in Eq. A.2, the scale of the quadratic Zeeman shift q_{Zeeman} in Eq. A.3, the dipole-dipole interaction energy E_{dip} in Eq. A.4, the scale of the quadratic AC Stark shift q_{Stark} in Eq. A.5, and the lattice scattering rate Γ_{scatter} in Eq. A.6.

The trapping frequency of the optical lattice is found by Taylor expanding the optical lattice potential $V(x) = V_{\text{trap}} \sin^2(kx) \simeq V_{\text{trap}} k^2 x^2$ and writing this in the common oscillator potential form,

$$\frac{1}{2} M \omega_{\text{trap}}^2 x^2 = V_{\text{trap}} k^2 x^2 \longrightarrow \omega_{\text{trap}} = \sqrt{\frac{2k^2 V_{\text{trap}}}{M}} = \sqrt{\frac{8\pi^2 V_{\text{trap}}}{\lambda^2 M}}, \quad (\text{A.1})$$

where λ is the wavelength of the optical lattice, M is the mass of the trapped atoms, and ω_{trap} is the fundamental frequency of the trap. This fundamental frequency sets the scale of the oscillator modes within the optical lattice minima, and provided it is less than thermal energy $k_B T$ we may assume that the atoms reside in the ground state oscillator mode of each site.

The recoil energy is given by

$$E_{\text{recoil}} = \frac{\hbar^2 k^2}{2M} = \frac{2\pi^2 \hbar^2}{M \lambda^2}, \quad (\text{A.2})$$

where M is the mass of the atom, while k and λ are the wavevector and wavelength of the optical lattice laser. The recoil energy is the natural energy scale used to measure properties of the optical lattice, and represents the kinetic energy of an atom initially at rest, after it has emitted a photon with a wavelength equal to the optical lattice wavelength.

The second-order quadratic shift from a static external magnetic field B is given by Ref. [127] as

$$q_{\text{Zeeman}} = \frac{(g_j\mu_B - g_i\mu_N/i)^2}{\Delta E_{\text{HF}}(1 + 2i)^2} B^2 \simeq \frac{\mu_B^2 B^2}{\Delta E_{\text{HF}}}, \quad (\text{A.3})$$

where ΔE_{HF} is the hyperfine splitting of the $^nS_{1/2}$ manifold, g_j and g_i are the electronic and nuclear Landé g-factors respectively, and i is the nuclear spin. Since $\mu_B/\mu_N \approx 2000$, where the Bohr magneton μ_B sets the scale for the electric magnetic moment and the nuclear magneton μ_N sets the scale for the nuclear moment, we may neglect the nuclear contribution to this term.

The maximum of the dipole-dipole interaction energy is given by

$$E_{\text{dip}}(\mathbf{r}) = -\frac{\mu_0\mu^2}{2\pi|\mathbf{r}|^3}, \quad (\text{A.4})$$

depends on the magnetic moment of the interacting atoms μ , where $\mathbf{r} = \mathbf{r}_1 - \mathbf{r}_2$ is the separation between the two atoms. Again, due to the large size of the electronic moment relative to the nuclear moment we may retain only the contribution from the electronic moment. We therefore only consider the dipolar interaction between the total electronic magnetic moments $\mu \simeq \mu_j$.

The quadratic portion of the AC Stark shift, induced by the oscillating electric field from incident light near resonant to the atomic D-line transition ($^nS_{1/2} \rightarrow ^n P_{1/2,3/2}$), results in energy shifts which depend on the hyperfine projection m as $\propto q_{\text{Stark}}m^2$.

For ^{87}Rb in the $F = 2$ ground state manifold, following Ref. [193] we find

$$q_{\text{Stark}} \simeq \frac{I}{8\pi^2 c} \left(\frac{\lambda^3 \Gamma A_{P_{1/2}}}{\delta(\delta - 2 A_{P_{1/2}})} \right), \quad (\text{A.5})$$

for these shifts, which are also called tensor light shifts. Here, I is the laser intensity, λ is the D-line transition wavelength, Γ is the natural linewidth of the excited $^n P_{1/2}$ state, δ is the laser detuning from the D-line transition, and $A_{P_{1/2}}$ is the hyperfine splitting in the excited state. For the calculations which appear in Tab. 3.6 we have used a rather strong laser intensity of $I = 5000 \text{ W/cm}^2$, since intense photoassociation lasers may be needed to reach our required amount of Feshbach tuning.

Finally, the scattering rate from a blue detuned lattice (defined by $\delta_{\text{trap}} > 0$ with $\delta_{\text{trap}} \equiv 2\pi\hbar c/\lambda - E_{\text{D-line}} > 0$) is given by Ref. [54] as

$$\Gamma_{\text{scatter}} = \Gamma \frac{\hbar\omega_{\text{trap}}}{4\delta_{\text{trap}}}, \quad (\text{A.6})$$

where the D-line corresponds to a transition from the $^n S_{1/2} \rightarrow ^n P_{1/2,3/2}$, and Γ is the natural linewidth (excited state lifetime) of this transition.

Appendix B: Rotational symmetry and related properties

B.1 The Clebsch-Gordan coefficients

The Clebsch-Gordan coefficients are a set of numbers used in quantum mechanics when adding two uncoupled angular momenta into a total angular momentum. These may be used for example in the coupling of the electronic and nuclear spins to determine the total angular momentum of an atom, or the coupling the total angular momentum for two atoms into the total angular momentum of a diatomic molecule. They may be defined by the projection of a two-particle product state $|f_1, m_1; f_2, m_2\rangle$ into a total angular momentum state $|F, M\rangle$, as in

$$|f_1, m_1; f_2, m_2\rangle = \sum_{F, M} |F, M\rangle \langle F, M | f_1, m_1; f_2, m_2\rangle, \quad (\text{B.1})$$

where the expansion coefficients $\langle F, M | f_1, m_1; f_2, m_2\rangle$ are known as the Clebsch-Gordan coefficients. These may be determined through a set of recurrence relations by using the formal definitions of the angular momentum operators $\hat{\mathbf{F}}^2$, \hat{F}_z and \hat{F}_\pm , or by explicit formulas derived from these relations.

Several properties of these coefficients greatly simplify our calculations. Additionally, throughout this work we restrict ourselves to indistinguishable bosonic atoms, for which $f_1 = f_2 = 1, 2, 3, \dots = \text{integer}$. Furthermore, the interaction between these identical bosons occurs only through even total-spin channels as described in Chap. 3, such that $F = 0, 2, 4, \dots = \text{even}$. For clarity, we first present these properties in

their general form, and then explicitly show how they further reduce with our specific assumptions.

In the most common phase convention, the Clebsch-Gordan coefficients can be chosen to be real, and so

$$\langle F, M | f_1, m_1; f_2, m_2 \rangle = \langle f_1, m_1; f_2, m_2 | F, M \rangle. \quad (\text{B.2})$$

Furthermore, since we have $f_1 = f_2 = f$, we introduce a compact notation which suppresses this index, giving

$$C_{m_1, m_2}^{FM} \equiv \langle f, m_1; f, m_2 | F, M \rangle = \langle F, M | f, m_1; f, m_2 \rangle. \quad (\text{B.3})$$

The f index is then left as an arbitrary parameter, or specified before specific calculations are carried out. For a given F and M this notation expresses the matrix elements of a matrix in m_1, m_2 -space. This is particularly useful when writing the Hamiltonian in spinor form, as is frequently done throughout Chaps. 3 and 4.

To switch the labels for atoms 1 and 2 we have the relation

$$\langle f_1, m_1; f_2, m_2 | F, M \rangle = (-1)^{F-f_1-f_2} \langle f_2, m_2; f_1, m_1 | F, M \rangle, \quad (\text{B.4})$$

which for $f_1 = f_2 = f$ and $F = \text{even}$ we find

$$C_{m_1, m_2}^{FM} = C_{m_2, m_1}^{FM}, \quad (\text{B.5})$$

and so the Clebsch-Gordan coefficient matrix C_{m_1, m_2}^{FM} is both real and symmetric in spin space.

To relate a Clebsch-Gordan coefficient for a given spin state, to the spin state which is polarized in the opposite direction along the quantization axis, we may use

the relation

$$\langle f_1, m_1; f_2, m_2 | F, M \rangle = (-1)^{F-f_1-f_2} \langle f_1, -m_1; f_2, -m_2 | F, -M \rangle, \quad (\text{B.6})$$

which for $f_1 = f_2 = f$ and $F =$ even gives

$$C_{m_1, m_2}^{FM} = C_{-m_1, -m_2}^{F, -M}, \quad (\text{B.7})$$

and so the sign of all projection indices may be flipped and leave the Clebsch-Gordan coefficient unchanged.

A useful condition to determine when some Clebsch-Gordan coefficients are zero is that the sum of the two individual spin projections must be equal to the total spin projection, such that $m_1 + m_2 = M$. This allows us to frequently use the condition

$$\langle f_1, m_1; f_2, m_2 | F, M \rangle = C_{m_1, m_2}^{FM} = 0 \text{ if } m_1 + m_2 \neq M, \quad (\text{B.8})$$

to reduce the number of terms in the Clebsch-Gordan matrix.

Finally, an explicit form of the Clebsch-Gordan coefficients for $F = 0$ are used extensively throughout Chaps. 4 and 5. Since $M = -F, \dots, F$, in this case we also have $M = 0$. This gives

$$\langle f_1, m_1; f_2, m_2 | 0, 0 \rangle = \delta_{f_1, f_2} \delta_{m_1, -m_2} \frac{(-1)^{f_1 - m_1}}{\sqrt{2f_1 + 1}}, \quad (\text{B.9})$$

or when written in terms of our identical bosons

$$C_{m, -m}^{00} = \frac{(-1)^m}{\sqrt{2f + 1}}. \quad (\text{B.10})$$

The magnitude of this expression is independent of m , and contains the factor of $1/\sqrt{2f + 1}$, which is crucial for the $1/f$ expansions used throughout this work.

B.2 Spherical tensor operators

The characterization of spin model ground states—specifically those involving large-spin spinor gases—often includes an analysis of the rotational properties of the spin wavefunction. These properties are captured most readily by taking expectation values of the spin wavefunction with respect to operators expressed in the spherical basis—a complex orthogonal basis constructed from the Cartesian basis. Operators written in the spherical basis, which are called spherical tensor operators, are classified directly by their rotational properties, such as whether they rotate like a quantum object with angular momentum $k = 0, 1, 2, \dots$, etc. This index k is called the rank of the spherical tensor.

For example, a scalar operator such as the potential energy $U(\mathbf{r})$ is rotationally invariant under all rotations. This would be trivially rewritten as a spherical tensor operator of rank $k = 0$. On the other hand, the total spin operator $\hat{\mathbf{J}} = \hat{J}_x \mathbf{e}_x + \hat{J}_y \mathbf{e}_y + \hat{J}_z \mathbf{e}_z$ is a vector operator, which rotates like an object with angular momentum $k = 1$. Note that this characterizes how the operator itself rotates, and so there is no dependence on the angular momentum j of the particle being operated on. The spherical basis vectors for a rank $k = 1$ spherical tensor are written in terms of the Cartesian basis as

$$\mathbf{e}_z \equiv \mathbf{e}_z \tag{B.11}$$

$$\mathbf{e}_\pm \equiv \frac{1}{\sqrt{2}}(\mathbf{e}_x \pm i\mathbf{e}_y), \tag{B.12}$$

which when applied to the spin vector operator turns the three Cartesian components \hat{J}_x , \hat{J}_y , and \hat{J}_z into three operators \hat{J}_z , \hat{J}_+ , and \hat{J}_- , where \hat{J}_+ and \hat{J}_- are the spin raising and lowering operators. Note that for a $k = 1$ operator there are three components, which correspond to the three possible values of the secondary quantum

number for a spin-1 object, $q = -1, 0, +1$. In general, a spherical tensor of rank k is denoted by $\hat{\mathbf{T}}^k$, and has $2k + 1$ components labelled by $q = -k, \dots, k$ and denoted by $\hat{T}^{k,q}$. We again emphasize that in the case of the spin operator $\hat{\mathbf{J}}$, the angular momentum j will determine the size of the Hilbert space, and therefore the size of the matrices used to represent each component \hat{J}_z , \hat{J}_+ , and \hat{J}_- , but it will not change the fact that this vector operator behaves like a rank $k = 1$ spherical tensor.

Tensor operators of higher rank are also of great interest to the characterization of quantum systems. For example, the electronic quadrupole moment and the spin nematic tensor operators are both represented by rank $k = 2$ spherical tensors. Higher-order terms in a multi-pole expansion are represented by spherical tensors of increasing rank. Therefore, a systematic way to determine the components $\hat{T}^{k,q}$ are needed, as the approach of defining \mathbf{e}_z , \mathbf{e}_+ , and \mathbf{e}_- are valid only for $k = 1$. Instead, the components of higher-rank spherical tensors are either defined by their commutation relations with the rank $k = 1$ operators, given by

$$[\hat{J}_\pm, \hat{T}^{k,q}] = \hbar\sqrt{(k \mp q)(k \pm q + 1)} \hat{T}^{k,q\pm 1} \quad (\text{B.13})$$

and

$$[\hat{J}_z, \hat{T}^{k,q}] = \hbar q \hat{T}^{k,q}, \quad (\text{B.14})$$

or by their rotational properties under a unitary operator U , given by

$$U^\dagger \hat{T}^{k,q} U = \sum_{q'=-k}^k U_{q,q'}^k \hat{T}^{k,q'}, \quad (\text{B.15})$$

where U corresponds to a physical rotation of the Cartesian axes. It is therefore seen that under a physical rotation, the rank of a spherical tensor remains unchanged, but the projections along the spherical bases do change, and hence the description of the rank k as an effective angular momentum quantum number for the operator itself.

B.3 The SU(2) and SU(N) Lie groups

Rotating the Cartesian axes of a physical system in classical mechanics is equivalent to operating on the position vector $\mathbf{r} = (x, y, z)$ with a time-independent 3×3 Cartesian matrix R . To correspond to a physical rotation, the matrix R must leave the origin invariant, the chirality of the coordinate system unchanged (such as right- or left-handedness), and preserve the distance between all points in the space. Mathematically these requirements imply that R must be orthogonal, such that $R^T.R = I$ where R^T is the transpose of matrix R , and with determinant $\det(R) = +1$. Since the total effect of successive coordinate rotations can be described in terms of a single coordinate rotation, R possess the properties of a mathematical group—specifically, the group known as SO(3), which stands for Special ($\det(R) = +1$) Orthogonal ($R^T.R = I$) matrices of rank 3.

Implementing a rotation in a quantum mechanical description is a bit different however, since the state vectors may have complex values and the state space may have any number of dimensions. Therefore, the matrices U which describe the rotations are not members of the SO(3) group, but instead are members of SU(N). For this group, the orthogonality condition of SO(3) is replaced by a unitarity condition $U^\dagger U = I$, where U^\dagger is the Hermitian conjugate or adjoint of matrix U , and N is the dimensionality.

In the case of continuous groups (as with those corresponding to physical rotations), which are known as Lie Groups, we may express the group elements as exponential of a related set of matrices called a Lie Algebra. This gives elements the form

$$U = \text{Exp} \left[i \sum_{\alpha} c_{\alpha} \hat{T}^{\alpha} \right] = 1 + i \sum_{\alpha} c_{\alpha} \hat{T}^{\alpha} + \dots, \quad (\text{B.16})$$

where the Lie Algebra elements T^{α} are known as the generators of the transformation and are Hermitian (such that $\hat{T}^{\dagger} = \hat{T}$), c_{α} is a vector which spans the space of the

Lie Algebra and defines the specific rotation, and α ranges over the dimensionality of the Lie Algebra space. The dimensionality of a Lie Algebra for the $SU(N)$ groups is finite and equal to $N^2 - 1$. This makes them easier to deal with in principle than the infinite number of continuous elements in a Lie Group. Therefore, as conditions on U arise through our physical analysis, we often consider infinitesimal rotations such that c_α is small, and we retain only the first two terms in the Taylor expansion.

For a quantum mechanical Hamiltonian \hat{H} to be invariant under some set of rotations, we require that if the states are rotated by a unitary operator $|a\rangle \rightarrow U|a\rangle$ that the Hamiltonian remain unchanged. This typically requires

$$U^\dagger \hat{H} U = \hat{H}. \quad (\text{B.17})$$

Since the continuous group U has an infinite number of elements, this is a cumbersome condition to verify. However, since all elements of U may be obtained by compounding an infinite number of infinitesimal rotations $U = dU_1 dU_2 \dots$, it is sufficient to study this condition for an infinitesimal rotation about single axis α . In that case we may use $U = 1 + i c_\alpha \hat{T}^\alpha$ to expand Eq. B.17 to obtain

$$\begin{aligned} \hat{H} - i c_\alpha \hat{T}^\alpha \hat{H} + i c_\alpha \hat{H} \hat{T}^\alpha + \mathcal{O}(c_\alpha^2) &= \hat{H} \\ \hat{H}, \hat{T}^\alpha - \hat{T}^\alpha \hat{H} &= 0 \\ \left[\hat{H}, \hat{T}^\alpha \right] &= 0, \end{aligned} \quad (\text{B.18})$$

where $[A, B] = AB - BA$ is the commutator. In this way, we determine the invariance of the system under some set of rotations U by checking that the generators for those rotations commute with the Hamiltonian.

When discussing the rotational symmetry of spin systems, the rotation group must be able to rotate the states about the three distinct Cartesian axes. This requires that the Lie Algebra consist of three elements, and so we find $N^2 - 1 = 3 \rightarrow N = 2$.

This means that when a quantum system is rotated in three-dimensional space, the spin state must be rotated by a corresponding element of the $SU(2)$ Lie Group, where the three generators of rotation are proportional to the Pauli spin matrices σ_x , σ_y , and σ_z . For a spin-1/2 system, the spin Hilbert space has a dimension of 2, and so the generators are proportional to the usual 2×2 representation of the Pauli matrices, given by

$$\sigma_x = \begin{pmatrix} 0 & 1 \\ 1 & 0 \end{pmatrix}, \quad \sigma_y = \begin{pmatrix} 0 & -i \\ i & 0 \end{pmatrix}, \quad \text{and } \sigma_z = \begin{pmatrix} 1 & 0 \\ 0 & -1 \end{pmatrix}. \quad (\text{B.19})$$

For a spin-1 system, the spin Hilbert space has a dimension of 3 and so the 3×3 generalizations of the Pauli matrices are used, such as

$$\sigma_x = \frac{1}{\sqrt{2}} \begin{pmatrix} 0 & 1 & 0 \\ 1 & 0 & 1 \\ 0 & 1 & 0 \end{pmatrix}, \quad \sigma_y = \frac{1}{\sqrt{2}} \begin{pmatrix} 0 & -i & 0 \\ i & 0 & -i \\ 0 & i & 0 \end{pmatrix}, \quad \text{and } \sigma_z = \begin{pmatrix} 1 & 0 & 0 \\ 0 & 0 & 0 \\ 0 & 0 & -1 \end{pmatrix}. \quad (\text{B.20})$$

For an arbitrary spin f , the $(2f + 1) \times (2f + 1)$ dimensional representation of the Pauli matrices are used as the generators for the group of continuous rotations.

In some scenarios, a Hamiltonian may be invariant under spin rotations with $N > 2$. The largest symmetry group possible comes when a spin f Hamiltonian is invariant under $SU(2f + 1)$ rotations. These rotations do not correspond to a physical rotation of the system, as the number of orthogonal axes is greater than the 3 physical Cartesian axes. Rather, a system with such a high spin symmetry reflects a lack of spin-dependence to Hamiltonian, as is the case with the nuclear spin of Alkali earth atoms. Enhanced $SU(N)$ symmetry spin models and expansions in $1/N$ have long been used as a tool for calculating magnetic ground states, and the symmetry is believed to introduce additional frustration and therefore long-range entanglement and topological order. These properties are characteristic of many interesting phases

such as quantum spin liquids and toric code models. More fundamentally, $SU(N)$ symmetry appears directly in Quantum Chromodynamics (QCD), which successfully describes intranuclear interactions.

An explicit example is given here for the $SU(3)$ Lie Group. The generators of $SU(3)$ are commonly written in terms of the eight Gell-Mann matrices, given by

$$T_1 = \begin{pmatrix} 0 & 1 & 0 \\ 1 & 0 & 0 \\ 0 & 0 & 0 \end{pmatrix}, \quad T_2 = \begin{pmatrix} 0 & -i & 0 \\ i & 0 & 0 \\ 0 & 0 & 0 \end{pmatrix}, \quad T_3 = \begin{pmatrix} 0 & 0 & 1 \\ 0 & 0 & 0 \\ 1 & 0 & 0 \end{pmatrix}, \quad (\text{B.21})$$

$$T_4 = \begin{pmatrix} 0 & 0 & -i \\ 0 & 0 & 0 \\ i & 0 & 0 \end{pmatrix}, \quad T_5 = \begin{pmatrix} 0 & 0 & 0 \\ 0 & 0 & 1 \\ 0 & 1 & 0 \end{pmatrix}, \quad T_6 = \begin{pmatrix} 0 & 0 & 0 \\ 0 & 0 & -i \\ 0 & i & 0 \end{pmatrix}, \quad (\text{B.22})$$

$$T_7 = \begin{pmatrix} 1 & 0 & 0 \\ 0 & -1 & 0 \\ 0 & 0 & 0 \end{pmatrix}, \quad \text{and} \quad T_8 = \frac{1}{\sqrt{3}} \begin{pmatrix} 1 & 0 & 0 \\ 0 & 1 & 0 \\ 0 & 0 & -2 \end{pmatrix}. \quad (\text{B.23})$$

Similarly, representations of the $SU(N)$ Lie Algebra matrices can be generated for all N , allowing straightforward determination of $SU(N)$ symmetry in any particular Hamiltonian.

Appendix C: Path Integral Formulation of the QSL MF Theory

This appendix reformulates the Hamiltonian description of Eq. 3.19 in terms of a path integral over the Lagrangian density. This allows us to apply the Hubbard-Stratonovich transformation—a means of formally reducing our action to the quadratic form of Eq. 4.1—and deriving the mean field equations (Eqs. 4.3 and 4.4) as saddle-point equations of that action.

C.1 Deriving a suitable path integral

First, from our starting Hamiltonian, Eq. 3.19, we can construct the coherent state slave boson path integral Z . This depends on the action $S(b_{i,m}^*, b_{i,m}) = i \int dt \mathcal{L}(t)$, and is given by

$$Z = \int \mathcal{D}[b_{i,m}^*] \mathcal{D}[b_{i,m}] e^{i \int dt \mathcal{L}(t)}, \quad (\text{C.1})$$

where the time-independent boson operators $\hat{b}_{i,m}^\dagger$ and $\hat{b}_{i,m}$ of the Hamiltonian description are now complex (c-number) functions of time $b_{i,m}^*(t)$ and $b_{i,m}(t)$, however we will suppress their time index t in all work that follows. The Lagrangian $\mathcal{L}(t)$ is found from the Hamiltonian by a Legendre transformation, given by

$$\mathcal{L}(t) = i \sum_{i,m} b_{i,m}^* \partial_t b_{i,m} - H(b_{i,m}^*, b_{i,m}), \quad (\text{C.2})$$

where $H(b_{i,m}^*, b_{i,m})$ is the Hamiltonian function written in terms of the boson fields. The path integral measures $\mathcal{D}[b_{i,m}^*]$ and $\mathcal{D}[b_{i,m}]$ each represent an integration over all

possible values of the boson fields for each lattice site, spin index, and at each time. In this way, the integration is over all possible configurations or “paths” of the boson fields, with a phase given by the exponential of the action.

Since our Hamiltonian is only valid in the one particle-per-site Hilbert space, we must enforce this constraint directly in the path integral measure. This is because the boson fields are integrated over all possible complex values, including variation in both the magnitude and phase. While the phase variations do not affect the boson density, the magnitude variations will. We implement the one-particle-per-site constraint by inserting

$$\prod_{i,t} \delta\left(\sum_m b_{i,m}^* b_{i,m} - 1\right) = \int \mathcal{D}[\lambda_i(t)] e^{-i \int dt \sum_i \lambda_i(t) (\sum_m b_{i,m}^* b_{i,m} - 1)}, \quad (\text{C.3})$$

into the path integral. Here, Π denotes the product operator and $\delta(x)$ is the Dirac delta function. This then requires that on each lattice site we have $n_b = \sum_m b_{i,m}^* b_{i,m} = 1$ at each moment in time, otherwise the path integral is zero. The right-hand side is obtained by applying a common definition of the delta function,

$$\delta(x) \propto \int_{-\infty}^{\infty} d\lambda e^{-ix\lambda} \quad (\text{C.4})$$

where λ is a variable introduced to be integrated over all possible real numbers. Since we introduce a delta function constraint for each i and t , the integration may be written as a path integral measure $\mathcal{D}[\lambda_i(t)]$ over a new field, $\lambda_i(t)$. This auxiliary field plays the role of a Lagrange multiplier in the Hamiltonian formalism, and so will

be occasionally referred to as such. Finally, by inserting Eq. C.3 into Eq. C.1 we

$$Z = \int \mathcal{D}[b_{i,m}^*, b_{i,m}, \lambda_i] \exp \left[i \int dt \left(\sum_{i,m} b_{i,m}^* (i\partial_t - \lambda_i) b_{i,m} + \sum_{\langle i,j \rangle} \sum_{F,M} \frac{J}{g_F} A_{i,j}^{FM*} A_{i,j}^{FM} + \sum_i \lambda_i \right) \right] \quad (\text{C.5})$$

for the path integral.

Next, we wish to employ a Hubbard-Stratonovich transformation to make our action quadratic in the bosonic field variables. We begin by introducing an generic Gaussian functional integral over an auxiliary complex field $Q_{i,j}^{FM}(t)$,

$$\int \mathcal{D}[Q_{i,j}^{FM}, Q_{i,j}^{FM*}] e^{-i \frac{J}{g_F} Q_{i,j}^{FM*} Q_{i,j}^{FM}} = 2\pi i g_F / J. \quad (\text{C.6})$$

The choice of a Gaussian functional is convenient since the integral can be done exactly, and is equal to a constant. We then perform a change of variables to shift $Q_{i,j}^{FM} \rightarrow Q_{i,j}^{FM} - A_{i,j}^{FM}$, which leaves the measure and the result of the Gaussian integral unchanged. This gives

$$\int \frac{\mathcal{D}[Q_{i,j}^{FM}, Q_{i,j}^{FM*}]}{2\pi i g_F / J} \exp \left[-i \frac{J}{g_F} (Q_{i,j}^{FM*} - A_{i,j}^{FM*})(Q_{i,j}^{FM} - A_{i,j}^{FM}) \right] = 1 \quad (\text{C.7})$$

Now we insert this identity into the path integral of Eq. C.5 at each time t , for each bond $\langle i, j \rangle$, and each total spin state $|F, M\rangle$. The result is

$$Z = \int \frac{\mathcal{D}[Q_{i,j}^{FM}, Q_{i,j}^{FM*}]}{2\pi i g_F / J} \exp \left[-i \frac{J}{g_F} (|Q_{i,j}^{FM}|^2 - Q_{i,j}^{FM} A_{i,j}^{FM*} - Q_{i,j}^{FM*} A_{i,j}^{FM}) \right] \quad (\text{C.8})$$

which effectively removes the interaction term for the addition of two new fields.

After dropping overall constants we have obtained

$$Z = \int \mathcal{D}[b_{i,m}^*, b_{i,m}, Q_{i,j}^{FM}, Q_{i,j}^{FM*}, \lambda_i] \exp \left[i \int dt \left(\sum_{i,m} b_{i,m}^* i \partial_t b_{i,m} - H_{\text{MF}} \right) \right], \quad (\text{C.9})$$

where H_{MF} is just our mean field Hamiltonian, Eq. 4.1. This current formulation is exact, since integrals over the HS fields and the Lagrange multiplier reproduce our spin Hamiltonian exactly (Eq. 3.19).

We note that the functional integration over $\lambda_i(t)$ makes it effectively behave like a quantum field, and in this case that the constraint is exactly obeyed. During the MF treatment of Chap. 4 the Lagrange multiplier λ is approximated to be site- and time-independent, known as the zeroth order mean field theory. We find using this approximation that the density fluctuations $\langle (\delta \hat{n}_i)^2 \rangle = \langle \hat{n}_i^2 \rangle - \langle \hat{n}_i \rangle^2 \neq 0$, and so while the constraint $\langle \hat{n}_i \rangle = 1$ is obeyed, there are still fluctuations out of the physical Hilbert space. The path integral formulation clearly shows that to suppress these fluctuations, we need to restore the dynamics of $\lambda_i(t)$, as is done by the full integration in Eq. C.5. However, due to the extensive mathematical treatment required by this approach and many subtle difficulties encountered during its implementation, we instead derive an effective quantum dimer Hamiltonian in Chap. 5.

C.2 The saddle-point approximation and the Euler-Lagrange equations

We often want to approximate our path integral by power expansion around the saddle points. These saddle points are defined by points where the action is stationary.

$$\begin{aligned} \frac{\partial}{\partial Q_{i,j}^{FM}} \mathcal{L} &= \frac{J}{g_F} (A_{i,j}^{FM*} - Q_{i,j}^{FM*}) = 0 \rightarrow A_{i,j}^{FM*} = Q_{i,j}^{FM*} \\ \frac{\partial}{\partial \lambda_i} \mathcal{L} &= \sum_m b_{i,m}^* b_{i,m} - 1 = 0 \rightarrow \sum_m b_{i,m}^* b_{i,m} = 1 \end{aligned} \quad (\text{C.10})$$

Since the Lagrangian doesn't depend explicitly on the time derivative of these variables, these equations correspond to the Euler-Lagrange equations. Therefore, the action is stationary when the paths follow the conditions above, namely, the self-consistency equation and the constraint equation.

To approximate the functional integral by its value at this saddle point we must have a large parameter multiplying the action. In the case of Sachdev's large-N, by integrating over the boson fields he obtains a prefactor of N, which justifies the saddle point solutions. In this problem, we believe that (at least for the Q^{00} -only limit) the degeneracy of the excitations with respect to the "spin"-index m gives a $2f + 1$ out front. Integrating over the bosons, and then taking the saddle points of the effective action for Q and λ . The saddle point equations are the same in the Hamiltonian formalism, (since the HS fields and the Lagrange multiplier λ contain no dynamic terms in the action), and so we can equivalently use the Hamiltonian formalism to find the bosonic eigenmodes and then solve the resulting saddle point equations.

Appendix D: Spin liquid mean field theory

This appendix provides additional details related to the spin liquid mean field theory presented in Chap. 4, including detailed descriptions of the diagonalization procedure followed to solve the MF Hamiltonian.

D.1 The Born-von Karman boundary conditions

When we impose periodic boundary conditions on the lattice, we must also require that all functions exhibit the same periodicity as the underlying lattice. This requirement is known as Born-von Karman boundary conditions. This is to say, for all functions f we have $f(\mathbf{r}_i + L_\alpha \hat{\alpha}) = f(\mathbf{r}_i)$, where \mathbf{r}_i is a lattice vector and $L_\alpha = a_\alpha N_\alpha$ is the length of the system in the $\hat{\alpha}$ direction. The Fourier decomposition of a function with this periodicity implies that

$$e^{-i\mathbf{k}\cdot(\mathbf{r}_i + L_\alpha \hat{\alpha})} = e^{-i\mathbf{k}\cdot\mathbf{r}_i}.$$

To satisfy this condition, we find that for each lattice direction $\hat{\alpha}$ we must have

$$k_\alpha = \frac{2\pi m_\alpha}{N_\alpha a_\alpha},$$

and so we may index the allowed values of k as

$$\vec{k} = \sum_\alpha \frac{m_\alpha}{N_\alpha} \vec{b}_\alpha,$$

where \vec{b}_α are the reciprocal lattice vectors. Here we have $\vec{a}_\alpha \cdot \vec{b}_\beta = 2\pi\delta_{\alpha,\beta}$ and m_α labels N_α unique values. This is achieved by taking $m_\alpha = 0, \dots, N_\alpha - 1$ or $m_\alpha = -N/2 + 1, \dots, N_\alpha/2$ for $m = \text{even}$, which define a region in k-space known as the 1st Brillouin zone (BZ). The latter is commonly utilized in this work, although both provide identical results. The reciprocal lattice basis vectors \vec{b}_α are defined as $\vec{b}_\alpha = (2\pi) * \vec{a}_\beta \times \vec{a}_\delta / V_c$, where V_c is the volume of the primitive cell and is given by $V_c = (\vec{a}_\beta \times \vec{a}_\delta) \cdot \vec{a}_\alpha$. Integration over the 1st BZ can be done by taking $\sum_{\vec{k}} / N \rightarrow \int d^2k / V_{\text{BZ}}$, and becomes exact in the thermodynamic limit, $N \rightarrow \infty$.

We often utilize fractional coordinates to write vectors within the 1st BZ, such as $\vec{k} = k_1\vec{b}_1 + k_2\vec{b}_2$, where $k_i = \{-1/2 + 1/N, \dots, 1/2 - 1/N, 1/2\}$, for a 2D system, as considered throughout this work. We then obtain specific forms of b_1 and b_2 when we look at particular lattices. Sites on a square lattice are denoted located at real-space lattice vectors $\vec{a}_i = a\hat{x}_i\mathbf{m}$, each of which has four nearest neighbors located at $\vec{\delta} = \{\pm\vec{a}_1, \pm\vec{a}_2\}$. The reciprocal lattice vectors for a square lattice are $\vec{b}_i = 2\pi/a\hat{x}_i$, the volume of the unit cell in real-space is $V_C = a^3$, and the volume of each BZ in k-space is $V_{\text{BZ}} = (2\pi)^2$.

For the triangular lattice, sites are located at $\vec{a}_1 = a\{1, 0\}$ and $\vec{a}_2 = a\{-1/2, \sqrt{3}/2\}$, and each have 6 nearest neighbors at $\vec{\delta} = \{\pm\vec{a}_1, \pm\vec{a}_2, \pm(\vec{a}_1 + \vec{a}_2)\}$. The reciprocal lattice basis vectors are $\vec{b}_1 = (2\pi/a)\{1, 1/\sqrt{3}\}$ and $\vec{b}_2 = (2\pi/a)\{0, 2/\sqrt{3}\}$. The volume of the unit cell is $V_C = \sqrt{3}/2$ and the volume of the first BZ is $V_{\text{BZ}} = 2(2\pi)^2/\sqrt{3}$. We can integrate over the fractional coordinates k_1 and k_2 from $\{-1/2, 1/2\}$, or directly over the Cartesian coordinates. However, in Cartesian coordinates we also need to parametrize the integration over just the 1st BZ. This is more complicated, since for the reciprocal lattice vectors are not parallel to the real-space x and y axes. Therefore, if we want $\vec{k} = k_1\vec{b}_1 + k_2\vec{b}_2$ in the form $\vec{k} = k_x\hat{x} + k_y\hat{y}$, then we find $k_x = 2\pi k_1$ and $k_y = (k_x + 4\pi k_2)\sqrt{3}$, or equivalently, $k_1 = k_x/(2\pi)$ and $k_2 = -(k_x - \sqrt{3}k_y)/(4\pi)$. For integrals on this lattice, we have

$dk_1 dk_2 = \sqrt{3}/(2*(2\pi)^2)$. Lattice vectors and integrals utilize these ranges throughout this work.

D.2 Fourier transform of H_{MF}

We utilize imposed translational symmetries, where the λ_i and $Q_{i,j}$ fields are uniform, to simplify the Fourier transform of our spin liquid MF Hamiltonian (Eq. 4.1). We define our FT by,

$$\hat{b}_{im} = \sum_k \frac{e^{ik \cdot r}}{\sqrt{N}} \hat{b}_{km},$$

where i is one of the N lattice sites, k is summed over vectors in the 1st BZ, and m is the magnetic quantum number of the boson operator. With this, the \hat{A}^{FM} operators become

$$A_{i,j}^{FM} = \sum_{m,m'} \langle m, m' | FM \rangle \hat{b}_{im} \hat{b}_{jm'} = \sum_{m,m'} \langle m, m' | FM \rangle \sum_{k,k'} \frac{1}{N} e^{i(k \cdot r_i + k' \cdot r_j)} \hat{b}_{km} \hat{b}_{k'm'}.$$

We then can expand the sum over nearest neighbors by writing $r_j = r_i + \delta$, so $k \cdot r_i + k' \cdot r_j = (k + k') \cdot r_i + k' \cdot \delta$. Then using the delta function relation

$$\sum_i e^{i(k+k') \cdot r_i} = N \delta_{k,-k'},$$

we obtain for the pairing terms in Eq. 4.1 of the form

$$H_{\text{pair}} = -\frac{1}{\bar{a}_F} C_{m,m'}^{FM} \sum_k (\epsilon_k Q^{FM} \hat{b}_{k,m}^\dagger \hat{b}_{-k,m'}^\dagger + \epsilon_{-k} Q^{FM*} \hat{b}_{k,m} \hat{b}_{-k,m'}),$$

where $\epsilon_k = \sum_\delta e^{-ik \cdot \delta}$ is the lattice contribution of the FT. In most cases, the nearest neighbors are in opposite pairs of $\pm\delta$, and so this term is even in k such that $\epsilon_k = \epsilon_{-k}$. Meanwhile, in the case of a uniform λ , the constraint from Eq. 4.1 becomes diagonal

in k , and is given by

$$H_C = \lambda \left(\sum_{k,m} \hat{b}_{k,m}^\dagger \hat{b}_{k,m} - N n_b \right).$$

Additionally, we often symmetrize the number operator

$$\sum_{k,m} \hat{b}_{km}^\dagger \hat{b}_{km} = \frac{1}{2} \sum_{k,m,m'} \delta_{m,m'} \left(\hat{b}_{km}^\dagger \hat{b}_{km'} + \hat{b}_{-k,-m}^\dagger \hat{b}_{-k,-m'} \right),$$

when writing the Hamiltonian in matrix form, as is done in the following sections.

D.3 The case of general Q^{FM}

Here we describe how to solve the MF Hamiltonian of Eq. 4.1 in its most general form, with all pairings Q^{FM} allowed to be non-zero. We begin by writing the Hamiltonian in spinor form, and making a change of basis to a new set of operators $\hat{\gamma}_{k,m}^\dagger / \hat{\gamma}_{k,m}$, which create/annihilate quasi-particle excitations. To do this, we first write a spinor Ψ_k , which is some column vector of the \hat{b} 's. We chose to define the spinor $\Psi_k = (\hat{b}_{k,f}, \dots, \hat{b}_{k,-f}, \hat{b}_{-k,f}^\dagger, \dots, \hat{b}_{-k,-f}^\dagger)$ during this work. The chosen spinor exists in a $2 * (2f + 1)$ dimensional space, and is therefore twice as large as the physical on-site Hilbert space of each spin, because it contains both the boson operators and their conjugate. We can then write the Hamiltonian as

$$H_{MF} = \sum_k \Psi_k^\dagger \mathcal{D}_k \Psi_k + \left(N_b \sum_{FM} \bar{a}_F |\bar{Q}_{FM}|^2 - N_s \lambda \left(n_b + \frac{2f + 1}{2} \right) \right),$$

where the term containing a factor of $2f + 1$ comes when including the density constraint in the matrix \mathcal{D}_k , since when doing so, one must commute the $2f + 1$ operators in the lower half of the Hamiltonian matrix, and so $2f + 1$ extra constants are picked up. However, the constants can be generally ignored, and the main object of interest is term in the Hamiltonian which contains the operators, and is characterized by a

$2(2f + 1) \times 2(2f + 1)$ non-diagonal matrix \mathcal{D}_k . This matrix is given by

$$\mathcal{D}_k = \begin{pmatrix} \lambda/2 * \mathbf{I}_{2f+1} & -\epsilon_k \bar{Q}^{FM} C^{FM} \\ -\epsilon_k \bar{Q}^{FM} * C^{FM} & \lambda/2 * \mathbf{I}_{2f+1} \end{pmatrix},$$

where \mathbf{I}_{2f+1} is a $(2f + 1) \times (2f + 1)$ identity matrix and C^{FM} is a $(2f + 1) \times (2f + 1)$ dimensional matrix with elements given by the Clebsch-Gordan coefficients, $(C^{FM})_{m,m'} = \langle FM|f, m; f, m'\rangle$. This non-trivial portion of the Hamiltonian is the matrix that we must diagonalize to find the energies and eigenstates of the model.

We require linear transformations of the \hat{b} s which diagonalize the Hamiltonian matrix \mathcal{D}_k , while maintaining the bosonic commutation relations of the operators— $[\hat{b}_{k,m}, \hat{b}_{k',m'}^\dagger] = \delta_{k,k'} \delta_{m,m'}$ and $[\hat{b}_{k,m}, \hat{b}_{k',m'}] = 0$ for both the \hat{b} and $\hat{\gamma}$ operators. The appropriate linear transformation is given by a matrix M^k such that $\Psi_k = M^k \Gamma_k$, where $\Gamma_k = (\hat{\gamma}_{k,f}, \dots, \hat{\gamma}_{k,-f}, \hat{\gamma}_{-k,f}^\dagger, \dots, \hat{\gamma}_{-k,-f}^\dagger)$ is a spinor of quasi-particle excitations. To find a suitable matrix M , we can solve for a matrix with satisfies our requirements. First, our diagonalization condition is $M_k^\dagger \mathcal{D}_k M_k = \omega_k$, where $(\omega_k)_{i,j} = \omega_{k,m} \delta_{i,j}$ is a diagonal matrix of the quasiparticle excitations, and $i = 1, \dots, 2(2f + 1)$ counts over the states in the doubled space. Secondly, the commutation condition can be better understood by introducing the matrix τ^3 whose element are $(\tau^3)_{i,j} = [(\Psi_k)_i, (\Psi_k^\dagger)_j]$, where the i and j run over the whole $2(2f + 1)$ space and pull a particular element from Ψ_k . It is named τ^3 , following Sachdev, due to its similarity in the two component case with the Pauli σ_z matrix. This τ^3 matrix completely characterizes the commutations for the b operators. Furthermore, for the $\hat{\gamma}$ particles to be bosons we should also have $(\tau^3)_{i,j} = [(\Gamma_k)_i, (\Gamma_k^\dagger)_j]$. Using this we can write,

$$(\tau^3)_{i,j} = [\Psi_i, \Psi_j^\dagger] = M_{i,a} M_{b,j}^\dagger [\Gamma_a, \Gamma_b^\dagger] = M_{i,a} M_{b,j}^\dagger \tau_{a,b}^3,$$

where all k subscripts have been dropped because this condition applies independently

at each k point.

So we find that the M matrix must satisfy the relations $M^{k\dagger}\mathcal{D}_kM^k = \omega_k$ and $M^k\tau^3M^{k\dagger} = \tau^3$. These conditions can be combined into a single condition,

$$M^{-1}(\tau^3\mathcal{D})M = \tau^3\omega,$$

where we've again dropped the k indices since this condition holds separately at each k point. From this equation it can be seen that the M matrix needs to diagonalize the matrix $\tau^3\mathcal{D}$. When we find M^k and we use it to change basis in the Hamiltonian so that $\sum_k \Psi_k^\dagger \mathcal{D}_k \Psi_k = \sum_k \Gamma_k^\dagger M_k^\dagger \mathcal{D}_k M_k \Gamma_k = \sum_k \Gamma_k^\dagger \omega_k \Gamma_k = \sum_{k,m} \omega_{k,m} \left(\text{gamma}_{k,m}^\dagger \text{gamma}_{k,m} + \text{gamma}_{-k,m} \text{gamma}_{-k,m}^\dagger \right)$. Applying this transformation gives a Hamiltonian diagonal in the gamma basis, which is given by

$$\hat{H}_{MF} = 2 \sum_{k,m} \omega_{k,m} \left(\hat{\gamma}_{k,m}^\dagger \hat{\gamma}_{k,m} + 1/2 \right) + \left(N_b \sum_{FM} \bar{a}_F |\bar{Q}_{FM}|^2 - N_s \lambda \left(n_b + \frac{2f+1}{2} \right) \right).$$

This Hamiltonian gives a BEC, characterized by a non-zero expectation value of $\langle \hat{\gamma} \rangle \sim \langle \hat{b} \rangle$ in the ground state, when the spectrum is gapless, such that $\omega_{k,m} = 0$ for some k and m . Otherwise, the state is completely specified by the set of Q^{FM} which minimize the MF energy.

D.4 Diagonalization for the nematic ansatz

In the nematic ansatz, where all $Q^{F,M \neq 0} = 0$, we have just a 2-dimensional spinor given by

$$\Psi_{km} = \begin{pmatrix} \hat{b}_{km} \\ \hat{b}_{-k,-m}^\dagger \end{pmatrix},$$

and in this basis, we may write an m -dependent matrix $\mathcal{D}_{k,m}$, in the form

$$D_{k,m} = \begin{pmatrix} \lambda/2 & -\epsilon_k \bar{Q}^{F0} C_{m,-m}^{F0} \\ -\epsilon_k \bar{Q}^{F0*} C_{m,-m}^{F0} & \lambda/2 \end{pmatrix}.$$

Using this 2D spinor, the diagonalization conditions give

$$\tau^3 = \begin{pmatrix} [\hat{b}_{km}, \hat{b}_{km}^\dagger] & [\hat{b}_{k,m}, \hat{b}_{-k,-m}] \\ [\hat{b}_{-k,-m}^\dagger, \hat{b}_{k,m}^\dagger] & [\hat{b}_{-k,-m}^\dagger, \hat{b}_{-k-m}] \end{pmatrix} = \begin{pmatrix} 1 & 0 \\ 0 & -1 \end{pmatrix},$$

and the 2×2 matrix we have to diagonalize is given by

$$\tau^3 D_{km} = \begin{pmatrix} \lambda/2 & -\epsilon_k \bar{Q}^{F0} C_{m,-m}^{F0} \\ \epsilon_k \bar{Q}^{F0*} C_{m,-m}^{F0} & -\lambda/2 \end{pmatrix}.$$

To diagonalize this matrix, we write in terms of two complex numbers a and b , such that

$$\tau^3 D = \begin{pmatrix} a & b \\ -b^* & -a \end{pmatrix}$$

where $a = \lambda/2$ and $b = -\epsilon_k \bar{Q}^{F0} C_{m,-m}^{F0}$. All k and m indices will be suppressed for now, as they can easily be added back in at the end. Therefore, in the most general form, we find two eigenvalues of

$$\Omega_{\pm} = \pm \sqrt{a^2 - |b|^2}.$$

With this, we construct the eigenvectors, $v^{\pm} = \alpha_{\pm}(v_1^{\pm}, v_2^{\pm})$, where α normalizes to

the τ^3 condition. The possible components of these eigenvectors are

$$v_1^\pm = b$$

$$v_2^\pm = (\Omega_\pm - a)$$

and

$$v_1^\pm = (\Omega_\pm + a)$$

$$v_2^\pm = -b^*.$$

We choose among these in a way that ensures proper behavior as $b \rightarrow 0$. In this limit, the Hamiltonian is diagonal, and the eigenvectors should be $v_+ = (1, 0)$ and $v_- = (0, 1)$. So, keeping in mind $\Omega_\pm \rightarrow \pm|a|$ as $b \rightarrow 0$, the correct choices for arbitrary b are

$$v_+ = \alpha_+ \begin{pmatrix} \Omega_+ + a \\ -b^* \end{pmatrix}$$

and

$$v_- = \alpha_- \begin{pmatrix} -b \\ -(\Omega_- - a) \end{pmatrix} = \alpha_- \begin{pmatrix} -b \\ \Omega_+ + a \end{pmatrix},$$

with

$$\alpha_\pm = (|\Omega_\pm \pm a|^2 - |b|^2)^{-1/2} = (|\Omega_+ + a|^2 - |b|^2)^{-1/2},$$

such that both normalizations are the same. This gives us

$$M_{k,m} = \alpha \begin{pmatrix} \Omega_+ + a & -b \\ -b^* & \Omega_+ + a \end{pmatrix} \tag{D.1}$$

$$= \frac{1}{\sqrt{2\omega_{k,m}(\omega_{k,m} + \lambda/2)}} \begin{pmatrix} \lambda/2 + \omega_{k,m} & \epsilon_k \bar{Q}^{F0} C_{m,-m}^{F0} \\ \epsilon_k \bar{Q}^{F0*} C_{m,-m}^{F0} & \lambda/2 + \omega_{k,m} \end{pmatrix}, \tag{D.2}$$

where the dispersion is identified to be the positive eigenvalues

$$\omega_{k,m} = \Omega_+ = \sqrt{(\lambda/2)^2 - (\epsilon_k \bar{Q}^{F0} C_{m,-m}^{F0})^2}.$$

Diagonalizing in this way allows us to write down all observables and expectation values in terms of integrals over elements of the M matrix.

D.5 Uniaxial and biaxial spin nematics

This section briefly discusses the difference between the two types of spin nematic phases, the uniaxial and biaxial nematics. The uniaxial state corresponds to the Q^{F0} states, where pairings with $M \neq 0$ are zero, while the biaxial is complicated to write for general Q^{FM} . This is because different biaxial states can be rotated into each other via spin space rotations [218]. However, the biaxial and uniaxial spin nematics have different symmetries from each other, and are not related by $SU(2)$ spin rotations, though certain $SU(N)$ rotations will connect the phases.

When the Q^{FM} s for a given ground state are expanded in terms of spherical tensor operators, the rank-2 portion can be written as a 3×3 Cartesian matrix. The mapping from the spherical basis to the Cartesian basis can be given by the real form of the spherical harmonics, as related to the complex Y_m^l s. For example, the real spherical harmonic $\sim xy/r^2$ would give the x-y component of the Cartesian matrix. With proper normalization, this matrix is equivalent to the rank-2 nematic order parameter, and may be aligned with the nematic “director” axis via an $SO(3)$ rotation in real space. By comparison of this tensor to the nematic order tensor, we are able to determine the nature of the nematic order apparent in our BEC phases.

Appendix E: Raleigh-Schrödinger perturbation theory

This appendix briefly reviews Raleigh-Schrödinger perturbation theory, as developed in Ref. [241]. This method of fully-degenerate time-independent perturbation theory is used to determine the effective Hamiltonian throughout this work.

First, we assume that the Hamiltonian is time-independent, and may be written $\hat{H} = \hat{H}_0 + \hat{V}$, where \hat{V} is the perturbation applied to a system described by \hat{H}_0 . We assume that the spectrum of \hat{H}_0 is discrete, and that its eigenvalues and eigenvectors are known. For generality we define the eigenvectors of \hat{H}_0 by $\hat{H}_0 |E_n^a\rangle = E_n^a |E_n^a\rangle$, where n labels different energies, and a accounts for any degeneracy. We choose d of these eigenvectors to define our target space, a subspace we define as \mathcal{D} , which is the subspace in which the effective Hamiltonian is valid. In all cases we consider, the subspace \mathcal{D} is defined by the d degenerate eigenvectors which share energy the ground state energy E_0 .

We now define the projection operator

$$\hat{P} \equiv \sum_{a \in \mathcal{D}} |E_0^a\rangle \langle E_0^a|, \quad (\text{E.1})$$

which projects a state of \hat{H}_0 into the target subspace \mathcal{D} , and the resolvent operator

$$\hat{R} = \sum_{(n,a) \notin \mathcal{D}} \frac{|E_n^a\rangle \langle E_n^a|}{E_0 - \hat{H}_0}, \quad (\text{E.2})$$

which projects a state of \hat{H}_0 out of the target subspace, weighted by the inverse of

the energy difference between the projected state and the ground state. With these two operators, an effective operator may be defined,

$$\hat{H}_{\text{eff}} = \hat{P}\hat{H}_0\hat{P} + \hat{P}\hat{V}\hat{R}\hat{V}\hat{P} + \mathcal{O}(\hat{V}) + \dots, \quad (\text{E.3})$$

and provided \hat{V} is small relative to \hat{H}_0 , the series can be approximated to any order desired.

Appendix F: Deriving a quantum dimer model

F.1 Determining the Feshbach coefficients

In this section, we calculate the coefficients α_F that parametrize the interactions U_F through the different spin channels. These properties depend crucially on the angular momentum of the atoms being used, and the quantum numbers for ^{23}Na and ^{87}Rb are shown in Tab. F.1. When laser light is incident upon a diatomic molecule with total orbital electronic momentum $L = 1$ and total spin electronic spin $S = 0$, and the detuning of the laser δ is large compared to hyperfine coupling of the atoms, the effective interaction between atoms to second order becomes

$$\hat{H}_{\text{int}} = \frac{\Omega^2}{\delta + i\Gamma/2} \sum_{jnn'} \left(\frac{\hat{a}_{j\uparrow n}^\dagger \hat{a}_{j\downarrow n'}^\dagger - \hat{a}_{j\downarrow n}^\dagger \hat{a}_{j\uparrow n'}^\dagger}{\sqrt{2}} \right) \left(\frac{\hat{a}_{j\downarrow n'} \hat{a}_{j\uparrow n} - \hat{a}_{j\uparrow n'} \hat{a}_{j\downarrow n}}{\sqrt{2}} \right), \quad (\text{F.1})$$

where $\hat{a}_{j\sigma n}$ annihilates a particle on lattice site j with electronic spin projection $\sigma = \uparrow, \downarrow$ and nuclear spin projection n . The coefficient of this interaction is a ratio of the Rabi frequency Ω , and the detuning δ , however, the a complex component to the detuning $i\Gamma$, where Γ is the linewidth of the hyperfine transition, allows for the loss of atoms through inelastic scattering. This is analogous to the laser coupling with individual atomic states to induce an effective lattice potential, as described in Sec. 2.3.1

In terms of our \hat{A}^{FM} pair operators this interaction can be written in the total

	²³ Na	⁸⁷ Rb
Mass	22.99 amu	86.9 amu
s	1/2	1/2
l	0	0
i	3/2	3/2
f	1, 2	1, 2
$\mu_e/\mu_B = gJ\sqrt{j(j+1)}$	1.73	
μ_{nuc}/μ_N	2.22	2.75

Table F.1: Angular momentum quantum numbers for two commonly used species of alkali atoms. Shown are the electronic spin s , the electronic orbital angular momentum l , the nuclear spin i , and the hyperfine spin $f = i \pm j$, where $j = s + l$ is the total electronic angular momentum. The electronic magnetic moment relative to the Bohr magneton (μ_e/μ_B) and the nuclear magnetic moment relative to the nuclear magneton (μ_{nuc}/μ_N) are shown.

spin basis as

$$\hat{H}_{\text{int}} = \frac{\Omega^2}{\delta + i\Gamma/2} \sum_{jFM} \alpha_F \hat{A}_{jj}^{FM\dagger} \hat{A}_{jj}^{FM}, \quad (\text{F.2})$$

where α_F is independent of M due to $SO(3)$ spin rotation symmetry. Since this interaction is local, we drop the spatial index from the operators in this section. We find from Eqs. F.1 and F.2 that

$$\alpha_F = \langle 0 | \hat{A}^{FM} \sum_{nn'} \left(\frac{\hat{a}_{\uparrow n}^\dagger \hat{a}_{\downarrow n'}^\dagger - \hat{a}_{\downarrow n}^\dagger \hat{a}_{\uparrow n'}^\dagger}{\sqrt{2}} \right) \left(\frac{\hat{a}_{\downarrow n'} \hat{a}_{\uparrow n} - \hat{a}_{\uparrow n'} \hat{a}_{\downarrow n}}{\sqrt{2}} \right) \hat{A}^{FM\dagger} | 0 \rangle. \quad (\text{F.3})$$

Since M is arbitrary, we set $M = 0$ for simplicity, and evaluate this expression by projecting the operators $\hat{a}_{\sigma n}$ into the atomic hyperfine spin, using the relation

$$\hat{a}_{\sigma n} = \sigma \sqrt{\frac{f+1/2-\sigma n}{2i+1}} \hat{b}_{n+\frac{1}{2}\sigma}^{(f=i-1/2)} - \sigma \sqrt{\frac{f+1/2+\sigma n}{2i+1}} \hat{b}_{n+\frac{1}{2}\sigma}^{(f=i+1/2)}, \quad (\text{F.4})$$

where $\sigma = +1(-1)$ corresponds to $\uparrow(\downarrow)$ spins, and the operators $\hat{b}_m^{(f=i\pm 1/2)}$ annihilate particles with hyperfine spin $f = i \pm 1/2$ and projection m . These hyperfine spin manifolds correspond to the ground and excited states, depending on the atom, and

we denote the ground state manifold as simply \hat{b}_m .

We may then derive an expression for α_F which is an explicit function of F , by using Eqs. F.3 and F.4, and several properties of the Clebsch-Gordan coefficients presented in App. B.1. We obtain

$$\alpha_F = \frac{(f+1)(2f+1) - F(F+1)/2}{2(i+1/2)^2}. \quad (\text{F.5})$$

The behavior of this function is shown in Fig. 3.5, and since this function decreases in magnitude with increasing F , our proposed OFR affects the $F = 0$ channel more than any other, and so it becomes possible to tune $U_0 \ll U_{F \neq 0}$, as required for our QDM description to be valid.

F.2 Commutation relations of the $\hat{A}_{i,j}^{00}$

The commutation relations of the \hat{A}^{00} operators are used extensively to calculate expectation values of the spin liquid and dimer order parameters. They are also used extensively in our derivation of the QDM. This section briefly presents relevant properties of these operators, to be used elsewhere in this thesis. These properties follow directly from the definition of the \hat{A}^{00} operators, as well as the bosonic commutation relations for the boson operators $\hat{b}_{i,m}$.

The \hat{A} operators are symmetric under exchange of site labels, such that $\hat{A}_{i,j}^{00} = \hat{A}_{j,i}^{00}$. They possess commutation relations with themselves of

$$\begin{aligned} [\hat{A}_{i,j}^{00}, \hat{A}_{k,l}^{00}] &= 0 \\ [\hat{A}_{i,j}^{00}, \hat{A}_{k,l}^{00\dagger}] &= \begin{cases} 1 + \frac{\hat{n}_i + \hat{n}_j}{2f+1}, & \text{for same bond} \\ \sum_m \frac{\hat{b}_{l,m}^\dagger \hat{b}_{i,m}}{2f+1} \equiv \hat{B}_{l,i}, & \text{for one shared site, in this case, } j = k \\ 0, & \text{for different bonds} \end{cases} \end{aligned} \quad (\text{F.6})$$

and with $\hat{B}_{i,j}$, as defined above in Eq. F.6, and the number operator \hat{n} , we find

$$\begin{aligned} [\hat{n}_i, \hat{A}_{i,j}^{00\dagger}] &= \hat{A}_{i,j}^{00\dagger} \\ [\hat{B}_{i,j}, \hat{A}_{k,l}^{00\dagger}] &= \frac{1}{2f+1}(\delta_{j,l}\hat{A}_{i,k}^{00\dagger} + \delta_{j,k}\hat{A}_{i,l}^{00\dagger}) \\ [\hat{B}_{i,j}, \hat{A}_{k,l}^{00}] &= -\frac{1}{2f+1}(\delta_{i,l}\hat{A}_{j,k}^{00} + \delta_{i,k}\hat{A}_{j,l}^{00}) \end{aligned} \quad (\text{F.7})$$

Importantly, we see from Eq. F.6 that the \hat{A}^{00} operators do not behave as pure bosonic variables, except in the $f \rightarrow \infty$ limit. Furthermore, since Eq. F.7 shows that \hat{n} and \hat{A}^{00} do not commute, the action of our MF Hamiltonian (Eq. 4.1) does not conserve particle number.

F.3 A rigorous derivation of the QDM

This section presents details of the primary result of this thesis. Namely, that when the scattering length tuned to favor singlet interactions, the effective Hamiltonian of bosons in an optical lattice can be written as a quantum dimer model. We also find that this derivation is rigorous in the large- f limit. We begin with the singlet-pair Hamiltonian,

$$\hat{H} = -\frac{J}{g_0} \sum_{\langle i,j \rangle} \hat{A}_{i,j}^\dagger \hat{A}_{i,j}, \quad (\text{F.8})$$

where we set $J/g_0 = 1$ and write $\hat{A}_{i,j} = \hat{A}_{i,j}^{00}$ to simplify expressions, since all $\hat{A}^{FM \neq 0} = 0$ in the limit being studied. The basis states constructed from singlet coverings may be written

$$|a\rangle \equiv \Pi_{(i,j) \in a} \hat{A}_{i,j}^\dagger |0\rangle \quad (\text{F.9})$$

for some state $|a\rangle$. However, these states are not orthogonal, and have an overlap of

$$S_{a,b} \equiv \langle a|b\rangle = \delta_{a,b} + \frac{1}{2f+1} \square_{a,b} + \frac{1}{(2f+1)^2} \square_{a,b}^{(2)} + \mathcal{O}(f^{-3}), \quad (\text{F.10})$$

where

$$\square_{a,b} = \begin{cases} 1, & \text{If } |a\rangle \text{ and } |b\rangle \text{ differ by a 4-site loop} \\ 0, & \text{otherwise,} \end{cases} \quad (\text{F.11})$$

and

$$\square_{a,b}^{(2)} = \begin{cases} 1, & \text{If } |a\rangle \text{ and } |b\rangle \text{ differ by two 4-site loops or one 6-site loop} \\ 0, & \text{otherwise.} \end{cases} \quad (\text{F.12})$$

From the overlap between the non-orthogonal singlet coverings $S_{a,b} = \langle a|b\rangle$, we may construct an orthogonal set of states $|\bar{a}\rangle$, which we call the dimer basis. These quantum dimer coverings are defined as

$$|\bar{a}\rangle \equiv \sum_b S_{a,b}^{-1/2} |b\rangle \quad (\text{F.13})$$

such that

$$\langle \bar{a}' | \bar{a} \rangle = \delta_{a',a}. \quad (\text{F.14})$$

When we employ the expansion of Eq. F.10, we find that Eq. F.13 gives

$$S_{a,b}^{-1/2} = \delta_{a,b} - \frac{1}{2(2f+1)} \square_{a,b} - \frac{1}{2(2f+1)^2} \square_{a,b}^{(2)} + \frac{3}{8} \frac{1}{(2f+1)^2} \sum_c \square_{a,c} \square_{c,b} + \mathcal{O}(f^{-3}). \quad (\text{F.15})$$

To simplify these expressions, we let $\beta \equiv 1/(2f+1)$, such that

$$S_{a,b} = \delta_{a,b} + \beta \square_{a,b} + \beta^2 \square_{a,b}^{(2)} \quad (\text{F.16})$$

and define $M_{a,b} = \left(\frac{1}{2} \square_{a,b}^{(2)} - \frac{3}{8} \sum_c \square_{a,c} \square_{c,b} \right)$ such that

$$S_{a,b}^{-1/2} = \delta_{a,b} - \frac{\beta}{2} \square_{a,b} - \beta^2 \left(\frac{1}{2} \square_{a,b}^{(2)} - \frac{3}{8} \sum_c \square_{a,c} \square_{c,b} \right) + \mathcal{O}(f^{-3}) \quad (\text{F.17})$$

$$= \delta_{a,b} - \beta \frac{1}{2} \square_{a,b} - \beta^2 M_{a,b} + \mathcal{O}(f^{-3}). \quad (\text{F.18})$$

With these expressions, we are in a position to calculate the effective Hamiltonian.

To derive the effective Hamiltonian in the subspace of nearest-neighbor dimer coverings, we utilize the method of Raleigh-Schrödinger perturbation theory, as outlined in App. E. First we write our singlet Hamiltonian as

$$\hat{H} = -\hat{N} - \left(\sum_{\langle i,j \rangle} \hat{A}_{i,j}^\dagger \hat{A}_{i,j} - \hat{N} \right) \quad (\text{F.19})$$

where the operator

$$\hat{N} |\bar{a}\rangle = N_a |\bar{a}\rangle \quad (\text{F.20})$$

counts the number of nearest-neighbor dimers in the orthogonal basis states. We define the unperturbed Hamiltonian

$$\hat{H}_0 = -\hat{N}, \quad (\text{F.21})$$

which has a low-energy sector containing the completely degenerate set of states which contain the maximum number of nearest-neighbor bonds, which we denote $|\bar{a}\rangle_n$ and for which $\hat{H}_0 |\bar{a}\rangle_n = -N_n |\bar{a}\rangle_n$. The remaining portion,

$$\hat{V} = - \left(\sum_{\langle i,j \rangle} \hat{A}_{i,j}^\dagger \hat{A}_{i,j} - \hat{N} \right), \quad (\text{F.22})$$

serves as our perturbation, which connects different states in our target subspace. The projection operator \hat{P} moves states into the target subspace of orthogonal nearest-

neighbor-only dimer coverings, and is written as

$$\hat{P} = \sum_a |\bar{a}\rangle_n \langle \bar{a}|_n, \quad (\text{F.23})$$

while the resolvent, which contains the higher-energy portion of the dimer Hilbert space, weighted by the inverse of the energy difference from the ground state, and is given by

$$\hat{R} = \sum_{a \notin n} \frac{|\bar{a}\rangle \langle \bar{a}|}{E_0^n - E_0^a} = \sum_{a \notin n} \frac{|\bar{a}\rangle \langle \bar{a}|}{N_a - N_n}. \quad (\text{F.24})$$

To compute the effective Hamiltonian, we must determine the action of the operators PVP and $PVRVP$ in the dimer basis. We start by calculating just \hat{V} . We have

$$\langle \bar{a} | \hat{V} | \bar{b} \rangle = - \langle \bar{a} | \sum_{\langle i,j \rangle} \hat{A}_{i,j}^\dagger \hat{A}_{i,j} | \bar{b} \rangle + N_b \delta_{a,b}, \quad (\text{F.25})$$

and we then expand the dimer states in terms of the singlet coverings, since \hat{A} acts most cleanly on states in that basis. This yields

$$\langle \bar{a} | \sum_{\langle i,j \rangle} \hat{A}_{i,j}^\dagger \hat{A}_{i,j} | \bar{b} \rangle = \sum_{c,d} S_{a,c}^{-1/2} \langle c | \sum_{\langle i,j \rangle} \hat{A}_{i,j}^\dagger \hat{A}_{i,j} | d \rangle S_{d,b}^{-1/2}. \quad (\text{F.26})$$

We then utilize the action of the \hat{A} operators, as given in Eq. 5.4 to determine

$$\sum_{\langle i,j \rangle} \langle c | \hat{A}_{i,j}^\dagger \hat{A}_{i,j} | d \rangle = \sum_{\langle i,j \rangle \in d} \langle c | \hat{A}_{i,j}^\dagger \hat{A}_{i,j} | d \rangle + \sum_{\langle i,j \rangle \notin d} \langle c | \hat{A}_{i,j}^\dagger \hat{A}_{i,j} | d \rangle \quad (\text{F.27})$$

$$= N_d \langle c | d \rangle + \beta \sum_{\langle i,j \rangle \notin d} \langle c | (i,j) : d \rangle \quad (\text{F.28})$$

$$= N_d S_{c,d} + \beta \sum_{\langle i,j \rangle \notin d} S_{c,(i,j):d}. \quad (\text{F.29})$$

This can now be put back into Eq. F.25 to obtain

$$\langle \bar{a} | \hat{V} | \bar{b} \rangle = - \sum_{c,d} S_{a,c}^{-1/2} \left(N_d S_{c,d} + \beta \sum_{\langle i,j \rangle \notin d} S_{c,(i,j):d} \right) S_{d,b}^{-1/2} + N_b \delta_{a,b}. \quad (\text{F.30})$$

We then apply the expansions of $S_{a,b}$ and $S_{a,b}^{-1/2}$ from Eqs. F.16 and F.18, to obtain

$$\begin{aligned} \langle \bar{a} | \hat{V} | \bar{b} \rangle = & - \sum_{c,d} \left(\delta_{a,c} - \beta \frac{1}{2} \square_{a,c} - \beta^2 M_{a,c} \right) \left(N_d [\delta_{c,d} + \beta \square_{c,d} + \beta^2 \square_{c,d}^{(2)}] \right. \\ & \left. + \beta \sum_{\langle i,j \rangle \notin d} [\delta_{c,(i,j):d} + \beta \square_{c,(i,j):d}] \right) \left(\delta_{d,b} - \beta \frac{1}{2} \square_{d,b} - \beta^2 M_{d,b} \right) + N_b \delta_{a,b}. \end{aligned} \quad (\text{F.31})$$

Here, we can see that the $\mathcal{O}(0)$ terms cancel, such that $-\sum_{c,d} \delta_{a,b} N_d \delta_{c,d} \delta_{d,b} = -N_b \delta_{a,b}$. This a crucial cancellation, and it ensures that the matrix elements of our perturbing Hamiltonian are small in the orthogonal basis, and ensuring the truncation of our series expansion is valid. Working out the rest of the factoring, but keeping terms only to $\mathcal{O}(\beta^2)$ we find,

$$\begin{aligned} \langle \bar{a} | \hat{V} | \bar{b} \rangle = & -\beta \left(\sum_{\langle i,j \rangle \notin b} \delta_{a,(i,j):b} + \frac{1}{2} (N_b - N_a) \square_{a,b} \right) \\ & + \beta^2 \left((N_a + N_b) M_{a,b} + \frac{1}{4} \sum_c N_c \square_{a,c} \square_{c,b} + \frac{1}{2} N_b \sum_c \square_{a,c} \square_{c,b} - N_b \square_{a,b}^{(2)} \right. \\ & \left. + \frac{1}{2} \sum_c \sum_{\langle i,j \rangle \notin c} \delta_{a,(i,j):c} \square_{c,b} - \sum_{\langle i,j \rangle \notin b} \square_{a,(i,j):b} + \frac{1}{2} \sum_c \sum_{\langle i,j \rangle \notin b} \square_{a,c} \delta_{c,(i,j):b} \right) \end{aligned} \quad (\text{F.32})$$

While this expression seems unwieldy, we find that it will simplify tremendously when used to calculate PVP and $PVRVP$. The matrix elements of these operators need only be taken between states in the nearest-neighbor only subspace, meaning we are to calculate $\langle \bar{a} |_n PVP | \bar{b} \rangle_n = \langle \bar{a} |_n V | \bar{b} \rangle_n$, and $\langle \bar{a} |_n PVRVP | \bar{b} \rangle_n = \langle \bar{a} |_n VRV | \bar{b} \rangle_n$.

We have $N_a = N_b = N_n$, where N_n is the number of nearest-neighbor dimers in the nearest-neighbor-only subspace, and depends on the lattice. For PVP we then

find

$$\begin{aligned}
\langle \bar{a} | _n V | \bar{b} \rangle_n &= -\beta \sum_{\langle i,j \rangle \notin b} \delta_{a,(i,j):b} \\
&+ \beta^2 \left(2N_n M_{a,b} + \frac{1}{4} \sum_c N_c \square_{a,c} \square_{c,b} + \frac{1}{2} N_n \sum_c \square_{a,c} \square_{c,b} - N_n \square_{a,b}^{(2)} \right. \\
&+ \left. \frac{1}{2} \sum_c \sum_{\langle i,j \rangle \notin c} \delta_{a,(i,j):c} \square_{c,b} - \sum_{\langle i,j \rangle \notin b} \square_{a,(i,j):b} + \frac{1}{2} \sum_c \sum_{\langle i,j \rangle \notin b} \square_{a,c} \delta_{c,(i,j):b} \right). \quad (\text{F.33})
\end{aligned}$$

Meanwhile, for *PVRVP*, must calculate

$$\langle \bar{a} | _n V R V | \bar{b} \rangle_n = \sum_{c \notin n} \frac{1}{N_c - N_n} \langle \bar{a} | _n V | \bar{c} \rangle \langle \bar{c} | V | \bar{b} \rangle_n. \quad (\text{F.34})$$

We again make use of Eq. F.32, however, since we only are keeping to $\mathcal{O}(\beta^2)$, and Eq. F.34 is quadratic in V , we only require the $\mathcal{O}(\beta)$ from Eq. F.32. In this case, the element between a ground and excited state is

$$\langle \bar{c} | \hat{V} | \bar{b} \rangle_n = -\beta \left(\sum_{\langle i,j \rangle \notin b} \delta_{c,(i,j):b} + \frac{1}{2} (N_n - N_c) \square_{c,b} \right). \quad (\text{F.35})$$

This gives

$$\langle \bar{a} | _n V R V | \bar{b} \rangle_n = \beta^2 \sum_{c \notin n} \frac{1}{N_c - N_n} \left(\sum_{\langle i,j \rangle \notin c} \delta_{a,(i,j):c} + \frac{1}{2} (N_c - N_n) \square_{a,c} \right) \quad (\text{F.36})$$

$$\left(\sum_{\langle i',j' \rangle \notin b} \delta_{c,(i',j'):b} - \frac{1}{2} (N_c - N_n) \square_{c,b} \right), \quad (\text{F.37})$$

which becomes simplified to

$$\begin{aligned} \langle \bar{a} | {}_n V R V | \bar{b} \rangle_n &= \beta^2 \sum_{c \notin n} \left(-\frac{1}{N_n - N_c} \sum_{\langle i,j \rangle \notin c} \delta_{a,(i,j):c} \sum_{\langle i',j' \rangle \notin b} \delta_{c,(i',j'):b} \right. \\ &\quad \left. - \frac{1}{2} \square_{c,b} \sum_{\langle i,j \rangle \notin c} \delta_{a,(i,j):c} + \frac{1}{2} \square_{a,c} \sum_{\langle i',j' \rangle \notin b} \delta_{c,(i',j'):b} + \frac{1}{4} (N_n - N_c) \square_{c,b} \square_{a,c} \right). \end{aligned} \quad (\text{F.38})$$

We may now return to our determination of the effective dimer Hamiltonian, which is given by

$${}_n \langle \bar{a} | \hat{H}_{\text{eff}} | \bar{b} \rangle_n = -N_n \delta_{a,b} + \langle \bar{a} | {}_n V | \bar{b} \rangle_n + \langle \bar{a} | {}_n V R V | \bar{b} \rangle_n. \quad (\text{F.39})$$

By plugging in what we have found from Eqs. F.33 and F.38, we obtain a rather complicated form of \hat{H}_{eff} . As we will show, this Hamiltonian takes on a very general forms, even when put onto different lattices. Additionally, since the large- f limit corresponds to $\beta \rightarrow 0$, in this limit only terms of $\mathcal{O}(\beta)$ are relevant. However, for physical spins of $f = 1 - 8$, it is likely that the $\mathcal{O}(\beta^2)$ terms are relevant. Retaining to second order, we find for Eq. F.39:

$$\begin{aligned} {}_n \langle \bar{a} | \hat{H}_{\text{eff}} | \bar{b} \rangle_n &= -N_n \delta_{a,b} - \beta \sum_{\langle i,j \rangle \notin b} \delta_{a,(i,j):b} \\ &\quad + \beta^2 \left(2N_n M_{a,b} + \frac{1}{4} \sum_c N_c \square_{a,c} \square_{c,b} + \frac{1}{2} N_n \sum_c \square_{a,c} \square_{c,b} - N_n \square_{a,b}^{(2)} \right. \\ &\quad + \frac{1}{2} \sum_c \sum_{\langle i,j \rangle \notin c} \delta_{a,(i,j):c} \square_{c,b} - \sum_{\langle i,j \rangle \notin b} \square_{a,(i,j):b} + \frac{1}{2} \sum_c \sum_{\langle i,j \rangle \notin b} \square_{a,b} \delta_{c,(i,j):b} \\ &\quad - \sum_{c \notin n} \frac{1}{N_n - N_c} \sum_{\langle i,j \rangle \notin c} \delta_{a,(i,j):c} \sum_{\langle i',j' \rangle \notin b} \delta_{c,(i',j'):b} - \sum_{c \notin n} \frac{1}{2} \square_{c,b} \sum_{\langle i,j \rangle \notin c} \delta_{a,(i,j):c} \\ &\quad \left. + \sum_{c \notin n} \frac{1}{2} \square_{a,c} \sum_{\langle i',j' \rangle \notin b} \delta_{c,(i',j'):b} - \sum_{c \notin n} \frac{1}{4} (N_n - N_c) \square_{c,b} \square_{a,c} \right). \end{aligned} \quad (\text{F.40})$$

After a bit of simplification, we obtain a lattice-independent result, given by

$$\begin{aligned}
{}_n\langle \bar{a} | \hat{H}_{\text{eff}} | \bar{b} \rangle_n &= -N_n \delta_{a,b} - \beta \sum_{\langle i,j \rangle \notin b} \delta_{a,(i,j):b} + \beta^2 \left[- \sum_{\langle i,j \rangle \notin b} \square_{a,(i,j):b} \right. \\
&+ \sum_{c \notin n} \sum_{\langle i,j \rangle \notin b} \square_{a,c} \delta_{c,(i,j):b} + \frac{1}{2} \sum_{c \in n} \sum_{\langle i,j \rangle \notin c} \delta_{a,(i,j):c} \square_{c,b} + \frac{1}{2} \sum_{c \in n} \sum_{\langle i,j \rangle \notin b} \square_{a,c} \delta_{c,(i,j):b} \\
&\left. - \sum_{c \notin n} \sum_{\langle i,j \rangle \notin c} \sum_{\langle i',j' \rangle \notin b} \frac{1}{N_n - N_c} \delta_{a,(i,j):c} \delta_{c,(i',j'):b} \right]. \quad (\text{F.41})
\end{aligned}$$

This can in fact be further simplified, to give

$$\hat{H}_{\text{eff}} = -N_n \delta_{a,b} - \beta \sum_{\langle i,j \rangle \notin b} \delta_{a,(i,j):b} - \beta^2 \sum_{c \notin n} \frac{1}{N_n - N_c} \sum_{\langle i,j \rangle \notin c} \sum_{\langle i',j' \rangle \notin b} \delta_{a,(i,j):c} \delta_{c,(i',j'):b}, \quad (\text{F.42})$$

which is the result presented in Sec. 5.3. However, how this simplification occurs is most easily seen when examining the terms on specific lattices.

We apply Eq. F.42 term by term for the case of a square lattice, to obtain a QDM as expressed in its the most common form. Tabs. 5.1 and 5.1 illustrate the processes which lead to these terms. We find for the $\mathcal{O}(\beta)$ term

$$\sum_{\langle i,j \rangle \notin b} \delta_{a,(i,j):b} = 2 \square_{a,b}. \quad (\text{F.43})$$

The first four $\mathcal{O}(\beta^2)$ terms give

$$\sum_{\langle i,j \rangle \notin b} \square_{a,(i,j):b} = \delta_{a,b}(N_{- -} + N_{- |} + N_{- .} + 2N_{\text{flip}}) + 4\square_{a,b}^2 + 4\square\square_{a,b} \quad (\text{F.44})$$

$$\sum_{c \notin n} \sum_{\langle i,j \rangle \notin b} \square_{a,c} \delta_{c,(i,j):b} = \sum_{\langle i,j \rangle \notin \text{P of } b} \square_{a,(i,j):b} = \delta_{a,b}(N_{- -} + N_{- |} + N_{- .}) + 2\square\square_{a,b} \quad (\text{F.45})$$

$$\frac{1}{2} \sum_{c \in n} \sum_{\langle i,j \rangle \notin c} \delta_{a,(i,j):c} \square_{c,b} = \sum_{c \in n} \square_{a,c} \square_{c,b} = \delta_{a,b} N_{\text{flip}} + 2\square_{a,b}^2 + \square\square_{a,b} \quad (\text{F.46})$$

$$\frac{1}{2} \sum_{c \in n} \sum_{\langle i,j \rangle \notin b} \square_{a,c} \delta_{c,(i,j):b} = \sum_{c \in n} \square_{a,c} \square_{c,b} = \delta_{a,b} N_{\text{flip}} + 2\square_{a,b}^2 + \square\square_{a,b}, \quad (\text{F.47})$$

which are seen to cancel out. Here $\square_{a,b}^2$ is zero unless states a and b differ by exactly two distinct flippable plaquettes, not to be confused with $\square_{a,b}^{(2)}$, which also allows for states differing by a 3-dimer loop. The non-canceling second-order term yields

$$\sum_{c \notin n} \sum_{\langle i,j \rangle \notin c} \sum_{\langle i',j' \rangle \notin b} \frac{1}{N_n - N_c} \delta_{a,(i,j):c} \delta_{c,(i',j'):b} = 2\delta_{a,b}(N_{- -} + N_{- |} + N_{- .}) + 4\square\square_{a,b}. \quad (\text{F.48})$$

At this point, we have matrix elements of the effective Hamiltonian in the nearest-neighbor only dimer subspace, and it is given by

$${}_n \langle \bar{a} | \hat{H}_{\text{eff}} | \bar{b} \rangle_n = -2\beta \square_{a,b} + \beta^2 \left[-2\delta_{a,b}(N_{- -} + N_{- |} + N_{- .}) - 4\square\square_{a,b} \right]. \quad (\text{F.49})$$

The final step is to remove the overall energy shift. To do this, we use the fact that $N_{\text{empty}} = N_{- -} + N_{- |} + N_{- .} + N_{\text{P}}$ and therefore $N_{- -} + N_{- |} + N_{- .} = N_{\text{empty}} - N_{\text{P}}$ for a square lattice, and that $N_{\text{empty}} = (N_{\text{links}} - N_n) = (2N_{\text{sites}} - N_{\text{sites}}/2) = \frac{3}{2}N_{\text{sites}}$ is a constant in the nearest-neighbor only subspace. Therefore, we can subtract this overall constant, and use that $N_{\text{P}} = 2N_{\text{flip}}$ to obtain an effective Hamiltonian of

$${}_n \langle \bar{a} | \hat{H}_{\text{eff}} | \bar{b} \rangle_n = -2\beta \square_{a,b} - 4\beta^2 \square\square_{a,b} + 4\beta^2 N_{\text{flip}} \delta_{a,b}, \quad (\text{F.50})$$

where $\beta = (2f + 1)^{-1}$. To relate to the coefficients of a typical QDM, we use $-t$ for the coefficient of $\square_{a,b}$, $-t'$ for the coefficient of $\square\square_{a,b}$, and V for the coefficient of $N_{\text{flip}}\delta_{a,b}$. This is shown in Tab. 5.2. We then write the Hamiltonian as

$$\hat{H}_{\square} = \sum_{\text{plaquettes}} \left[-t \left(\left| \begin{array}{c} \text{---} \\ \text{---} \end{array} \right\rangle \langle \text{---} \text{---} | + \text{H.c.} \right) + V \left(\left| \begin{array}{c} \text{---} \\ \text{---} \end{array} \right\rangle \langle \text{---} | + \left| \text{---} \text{---} \right\rangle \langle \text{---} \text{---} | \right) \right] \\ + t' \sum_{\text{6-site plaquettes}} \left[\left| \begin{array}{c} \text{---} \\ \text{---} \end{array} \right\rangle \langle \text{---} \text{---} | + \left| \begin{array}{c} \text{---} \\ \text{---} \end{array} \right\rangle \langle \text{---} | + \text{H.c.} \right]. \quad (\text{F.51})$$

By following a similar procedure we may determine the quantum dimer Hamiltonian on different lattices. This process is assisted by the use of real-space diagrams of the dimer resonances, similar to the approach taken for the square lattice (Tab. 5.1), and is shown for the triangular lattice in Tab. F.2. For the triangular lattice we find

$${}_n \langle \bar{a} | \hat{H}_{\text{eff}} | \bar{b} \rangle_n = -2(\beta + \beta^2)\square_{a,b} - 4\beta^2\square\square_{a,b} + \beta^2 N_{\text{flip}}\delta_{a,b}, \quad (\text{F.52})$$

where again, $\beta = (2f + 1)^{-1}$, and so we see that in this case the 4-site resonance picks up a sub-leading contribution of $\mathcal{O}(f^{-2})$. The QDM on the triangular lattice may expressed in the semi-pictorial form as

$$\hat{H}_{\Delta} = \sum_{\text{plaquettes}} \left[-t \left(\left| \begin{array}{c} \text{---} \\ \text{---} \end{array} \right\rangle \langle \text{---} \text{---} | + \dots + \text{H.c.} \right) + V \left(\left| \begin{array}{c} \text{---} \\ \text{---} \end{array} \right\rangle \langle \text{---} | + \dots \right) \right] \\ + t' \sum_{\text{6-site plaquettes}} \left[\left| \begin{array}{c} \text{---} \\ \text{---} \end{array} \right\rangle \langle \text{---} \text{---} | + \dots + \text{H.c.} \right], \quad (\text{F.53})$$

where the “...” represent the other orientations of the dimers on 4- and -6-site plaquettes which are not shown. Other lattices, follow a similar approach, and the associated QDM coefficients for the kagome and honeycomb lattice are presented in Tab. 5.2.

	$ b\rangle$	$ c\rangle$	$ a\rangle$	Multiplicity
t		N/A		2
t				2
t'				4
V			$ b\rangle$	2
V			$ b\rangle$	2
V			$ b\rangle$	2
V			$ b\rangle$	2
V			$ b\rangle$	2
V			$ b\rangle$	2
V			$ b\rangle$	2
V			$ b\rangle$	2

Table F.2: Pictorial derivation of the t and t' terms of the quantum dimer model on the triangular lattice. We note that there is a sub-leading contribution to the 4-site resonance. The kinetic resonances result in $t : 2(\beta + \beta^2)\square_{a,b}$ and $t' : 4\beta^2\square_{a,b}$. Meanwhile, the effective repulsive potential becomes $V : 4\beta^2 N_{\text{flip}}\delta_{a,b}$.

References

- [1] L. Landau, *Nature* **138** (1936).
- [2] R. B. Laughlin, *Phys. Rev. Lett.* **50**, 1395 (1983).
- [3] H. L. Stormer and D. C. Tsui, *Science* **220**, 1241 (1983).
- [4] G. Moore and N. Read, *Nuclear Physics B* **360**, 362 (1991).
- [5] S. L. Sondhi, A. Karlhede, S. A. Kivelson, and E. H. Rezayi, *Phys. Rev. B* **47**, 16419 (1993).
- [6] X. G. Wen and Q. Niu, *Phys. Rev. B* **41**, 9377 (1990).
- [7] X. G. Wen, *ISRN Cond. Mat. Phys.* (2013).
- [8] S. C. Zhang, T. H. Hansson, and S. Kivelson, *Phys. Rev. Lett.* **62**, 82 (1989).
- [9] P. Anderson, *Materials Research Bulletin* **8**, 153 (1973).
- [10] L. Pauling, *Proceedings of the Royal Society of London A: Mathematical, Physical and Engineering Sciences* **196**, 343 (1949).
- [11] V. Kalmeyer and R. B. Laughlin, *Phys. Rev. Lett.* **59**, 2095 (1987).
- [12] S. A. Kivelson, D. S. Rokhsar, and J. P. Sethna, *Phys. Rev. B* **35**, 8865 (1987).
- [13] P. W. Anderson, *Science* **235**, 1196 (1987).
- [14] P. A. Lee, N. Nagaosa, and X.-G. Wen, *Rev. Mod. Phys.* **78**, 17 (2006).
- [15] F. Mila, *European Journal of Physics* **21**, 499 (2000).
- [16] X. Wen, *Quantum field theory of many-body systems* (OUP Oxford, 2004).
- [17] A. Kitaev and J. Preskill, *Phys. Rev. Lett.* **96**, 110404 (2006).
- [18] T. Senthil and M. P. A. Fisher, *Phys. Rev. Lett.* **86**, 292 (2001).
- [19] M. Punk, D. Chowdhury, and S. Sachdev, *Nature Physics* **10** (2014).
- [20] X. G. Wen, *Phys. Rev. B* **44**, 2664 (1991).
- [21] X.-G. Wen, *Phys. Rev. B* **65**, 165113 (2002).
- [22] M. Levin and X.-G. Wen, *Phys. Rev. Lett.* **96**, 110405 (2006).
- [23] L. Cincio and G. Vidal, *Phys. Rev. Lett.* **110**, 067208 (2013).
- [24] X.-G. Wen, *Phys. Rev. Lett.* **90**, 016803 (2003).
- [25] S. Yan, D. A. Huse, and S. R. White, *Science* **332**, 1173 (2011).
- [26] H.-C. Jiang, H. Yao, and L. Balents, *Phys. Rev. B* **86**, 024424 (2012).

- [27] P. A. Lee, *Science* **321**, 1306 (2008).
- [28] T.-H. Han, J. S. Helton, S. Chu, D. G. Nocera, J. A. Rodriguez-Rivera, C. Broholm, and Y. S. Lee, *Nature* **492**, 406 (2012).
- [29] T. Fennell, M. Kenzelmann, B. Roessli, H. Mutka, J. Ollivier, M. Ruminy, U. Stuhr, O. Zaharko, L. Bovo, A. Cervellino, et al., *Phys. Rev. Lett.* **112**, 017203 (2014).
- [30] T. Isono, H. Kamo, A. Ueda, K. Takahashi, M. Kimata, H. Tajima, S. Tsuchiya, T. Terashima, S. Uji, and H. Mori, *Phys. Rev. Lett.* **112**, 177201 (2014).
- [31] L. Balents, *Nature (London)* **464**, 199 (2010).
- [32] Y. Zhou, K. Kanoda, and T.-K. Ng, *Rev. Mod. Phys.* **89**, 025003 (2017).
- [33] M. Hermanns, I. Kimchi, and J. Knolle, *Annual Review of Condensed Matter Physics* **9**, 17 (2018).
- [34] S. Depenbrock, I. P. McCulloch, and U. Schollwöck, *Physical Review Letters* **109**, 067201 (2012).
- [35] M. J. Lawler, *New Journal of Physics* **15**, 043043 (2013).
- [36] W.-J. Hu, S.-S. Gong, W. Zhu, and D. N. Sheng, *Physical Review B* **92**, 140403 (2015).
- [37] Z. Zhu and S. R. White, *Physical Review B* **92**, 041105 (2015).
- [38] G. H. Wannier, *Phys. Rev.* **79**, 357 (1950).
- [39] P. W. Anderson, *Phys. Rev.* **102**, 1008 (1956).
- [40] C. Lacroix, P. Mendels, and F. Mila, *Introduction to frustrated magnetism: materials, experiments, theory* (Springer Berlin Heidelberg, 2011).
- [41] R. Moessner and A. P. Ramirez, *Physics Today* **59**, 24 (2006).
- [42] D. S. Rokhsar and S. A. Kivelson, *Phys. Rev. Lett.* **61**, 2376 (1988).
- [43] R. Moessner and S. L. Sondhi, *Phys. Rev. Lett.* **86**, 1881 (2001).
- [44] R. Moessner, S. L. Sondhi, and E. Fradkin, *Phys. Rev. B* **65**, 024504 (2001).
- [45] E. Fradkin, D. A. Huse, R. Moessner, V. Oganesyan, and S. L. Sondhi, *Phys. Rev. B* **69**, 224415 (2004).
- [46] R. Moessner, S. L. Sondhi, and P. Chandra, *Phys. Rev. Lett.* **84**, 4457 (2000).
- [47] G. Misguich, D. Serban, and V. Pasquier, *Phys. Rev. Lett.* **89**, 137202 (2002).
- [48] S. Sachdev, *Phys. Rev. B* **40**, 5204 (1989).
- [49] T. Senthil, A. Vishwanath, L. Balents, S. Sachdev, and M. P. A. Fisher, *Science* **303**, 1490 (2004).
- [50] A. Vishwanath, L. Balents, and T. Senthil, *Phys. Rev. B.* **69**, 1 (2004).
- [51] A. Kitaev, *Ann. Phys.* **303**, 2 (2003).

- [52] L. B. Ioffe, M. V. Feigel'man, A. Ioselevich, D. Ivanov, M. Troyer, and G. Blatter, *Nature* **415**, 503 (2002).
- [53] C. Nayak, S. H. Simon, A. Stern, M. Freedman, and S. Das Sarma, *Rev. Mod. Phys.* **80**, 1083 (2008).
- [54] D. Jaksch and P. Zoller, *Ann. Phys.* **315**, 52 (2005).
- [55] A. Koetsier, R. A. Duine, I. Bloch, and H. T. C. Stoof, *Phys. Rev. A* **77**, 023623 (2008).
- [56] U.-J. Wiese, *Annalen der Physik* **525**, 777 (2013).
- [57] M. Greiner, O. Mandel, T. Esslinger, T. W. Hänsch, and I. Bloch, *Nature (London)* **415**, 39 (2002).
- [58] W. V. Liu, F. Wilczek, and P. Zoller, *Physical Review A* **70**, 033603 (2004).
- [59] R. Jördens, N. Strohmaier, K. Günter, H. Moritz, and T. Esslinger, *Nature* **455**, 204 (2008).
- [60] O. Dutta, M. Gajda, P. Hauke, M. Lewenstein, D.-S. Lühmann, B. A. Malomed, T. Sowiński, and J. Zakrzewski, *Reports on Progress in Physics* **78**, 066001 (2015).
- [61] J. Simon, W. S. Bakr, R. Ma, M. E. Tai, P. M. Preiss, and M. Greiner, *Nature* **472**, 307 (2011).
- [62] A. Imambekov, M. Lukin, and E. Demler, *Phys. Rev. A* **68**, 063602 (2003).
- [63] D. Greif, T. Uehlinger, G. Jotzu, L. Tarruell, and T. Esslinger, *Science (New York, N.Y.)* **340**, 1307 (2013).
- [64] M. F. Parsons, A. Mazurenko, C. S. Chiu, G. Ji, D. Greif, and M. Greiner, *Science* **353** (2016).
- [65] D. M. Stamper-Kurn, M. R. Andrews, A. P. Chikkatur, S. Inouye, H.-J. Miesner, J. Stenger, and W. Ketterle, *Phys. Rev. Lett.* **80**, 2027 (1998).
- [66] J. Stenger, S. Inouye, D. M. Stamper-Kurn, H.-J. Miesner, A. P. Chikkatur, and W. Ketterle, *Nature* **396**, 345 (1998).
- [67] D. Jaksch, C. Bruder, J. I. Cirac, C. W. Gardiner, and P. Zoller, *Phys. Rev. Lett.* **81**, 3108 (1998).
- [68] C. Wu, *Physics* **3**, 92 (2010).
- [69] E. Demler and F. Zhou, *Phys. Rev. Lett.* **88**, 163001 (2002).
- [70] S. K. Yip, *Phys. Rev. Lett.* **90**, 250402 (2003).
- [71] F. Zhou and G. W. Semenoff, *Phys. Rev. Lett.* **97**, 180411 (2006).
- [72] K. Eckert, Ł. Zawitkowski, M. J. Leskinen, A. Sanpera, and M. Lewenstein, *New J. Phys.* **9**, 133 (2007).
- [73] S. Chen, C. Wu, S. C. Zhang, and Y. Wang, *Phys. Rev. B.* **72**, 3 (2005).

- [74] C. Xu and C. Wu, Phys. Rev. B. **77**, 1 (2008).
- [75] E. Szirmai and M. Lewenstein, Europhys. Lett. **93**, 66005 (2011).
- [76] B. Sundar, T. C. Rutkowski, E. J. Mueller, and M. J. Lawler, arXiv:1702.05514v2 (2017).
- [77] M. Hermele, V. Gurarie, and A. M. Rey, Phys. Rev. Lett. **103**, 135301 (2009).
- [78] Y.-H. Chan and L.-M. Duan, New J. Phys **14**, 113039 (2012).
- [79] P. Sinkovicz, A. Zamora, E. Szirmai, M. Lewenstein, and G. Szirmai, Phys. Rev. A **88**, 043619 (2013).
- [80] H. Song and M. Hermele, Phys. Rev. B. **87**, 1 (2013).
- [81] T. C. Rutkowski and M. J. Lawler, Phys. Rev. B **93**, 094405 (2016).
- [82] N. Y. Yao, M. P. Zaletel, D. M. Stamper-Kurn, and A. Vishwanath, Nature Physics (2018).
- [83] A. V. Gorshkov, M. Hermele, V. Gurarie, C. Xu, P. S. Julianne, J. Ye, P. Zoller, E. Demler, M. D. Lukin, and A. M. Rey, Nat. Phys. **6**, 289 (2010).
- [84] M. A. Cazalilla and A. M. Rey, Rep. Prog. Phys **77**, 124401 (2014).
- [85] J. Hubbard, Proceedings of the Royal Society of London A: Mathematical, Physical and Engineering Sciences **276**, 238 (1963).
- [86] A. Altland and B. Simons, *Condensed matter field theory* (Cambridge University Press, 2010).
- [87] G. Misguich, arXiv:0809.2257v1 (2008).
- [88] L. P. Kadanoff, Journal of Statistical Physics **137**, 777 (2009).
- [89] T. Holstein and H. Primakoff, Phys. Rev. **58**, 1098 (1940).
- [90] I. Rousochatzakis, R. Moessner, and J. Van Den Brink, Physical Review B **88** (2013).
- [91] H. N. V. Temperley and M. E. Fisher, The Philosophical Magazine: A Journal of Theoretical Experimental and Applied Physics **6**, 1061 (1961).
- [92] P. Kasteleyn, Physica **27**, 1209 (1961).
- [93] R. Moessner and K. S. Raman, arXiv:0809.3051v1 (2008).
- [94] J. Goldstone, A. Salam, and S. Weinberg, Phys. Rev. **127**, 965 (1962).
- [95] G. Misguich, “Quantum spin liquids and fractionalization”, in *Introduction to frustrated magnetism*, edited by C. Lacroix, P. Mendels, and F. Mila (Springer Berlin Heidelberg, Berlin, Heidelberg, 2011), pp. 407–435.
- [96] C. Adams and E. Riis, Prog. Quantum Electron. **21**, 1 (1997).
- [97] W. D. Phillips, Rev. Mod. Phys. **70**, 721 (1998).
- [98] M. H. Anderson, J. R. Ensher, M. R. Matthews, C. E. Wieman, and E. A. Cornell, Science **269**, 198 (1995).

- [99] K. B. Davis, M. O. Mewes, M. R. Andrews, N. J. van Druten, D. S. Durfee, D. M. Kurn, and W. Ketterle, *Phys. Rev. Lett.* **75**, 3969 (1995).
- [100] C. C. Bradley, C. A. Sackett, J. J. Tollett, and R. G. Hulet, *Phys. Rev. Lett.* **75**, 1687 (1995).
- [101] A. Griesmaier, J. Werner, S. Hensler, J. Stuhler, and T. Pfau, *Phys. Rev. Lett.* **94**, 1 (2005).
- [102] Y. Tang, N. Q. Burdick, K. Baumann, and B. L. Lev, *New J. Phys.* **17**, 045006 (2015).
- [103] T. Ohmi and K. Machida, *J. Phys. Soc. Jpn.* **67**, 1822 (1998).
- [104] T.-L. Ho, *Phys. Rev. Lett.* **81**, 742 (1998).
- [105] L. E. Sadler, J. M. Higbie, S. R. Leslie, M. Vengalattore, and D. M. Stamper-Kurn, *Nature* **443**, 312 (2006).
- [106] T. Zibold, V. Corre, C. Frapolli, A. Invernizzi, J. Dalibard, and F. Gerbier, *Phys. Rev. A - At. Mol. Opt. Phys.* **93**, 1 (2016).
- [107] D. S. Hall, M. W. Ray, K. Tiurev, E. Ruokokoski, A. H. Gheorghe, and M. Möttönen, *Nat. Phys.* **12**, 478 (2016).
- [108] M. Lewenstein, A. Sanpera, and V. Ahufinger, *Ultracold atoms in optical lattices: simulating quantum many-body systems* (OUP Oxford, 2012).
- [109] P. Jessen and I. Deutsch, *Advances in Atomic, Molecular and Optical Physics* **37**, 95 (1996).
- [110] I. Bloch, J. Dalibard, and W. Zwerger, *Rev. Mod. Phys.* **80**, 885 (2008).
- [111] R. Grimm, M. Weidemüller, and Y. B. Ovchinnikov, in *Adv. at. mol. opt. phys.* Vol. 42 (2000), pp. 95–170.
- [112] D. C. McKay and B. DeMarco, *Reports on Progress in Physics* **74**, 054401 (2011).
- [113] B. DeMarco and D. S. Jin, *Science* **285**, 1703 (1999).
- [114] S. Hensler, A. Greiner, J. Stuhler, and T. Pfau, *EPL (Europhysics Letters)* **71**, 918 (2005).
- [115] M. Fattori, T. Koch, S. Goetz, A. Griesmaier, S. Hensler, J. Stuhler, and T. Pfau, *Nat Phys* **2**, 765 (2006).
- [116] P. Medley, D. M. Weld, H. Miyake, D. E. Pritchard, and W. Ketterle, *Phys. Rev. Lett.* **106**, 195301 (2011).
- [117] R. A. Hart, P. M. Duarte, T.-L. Yang, X. Liu, T. Paiva, E. Khatami, R. T. Scalettar, N. Trivedi, D. A. Huse, and R. G. Hulet, *Nature* **519**, 211 EP (2015).
- [118] A. Mazurenko, C. S. Chiu, G. Ji, M. F. Parsons, M. Kanász-Nagy, R. Schmidt, F. Grusdt, E. Demler, D. Greif, and M. Greiner, *Nature* **545** (2017).
- [119] C. Wu, *Mod. Phys. Lett. B* **20**, 1707 (2006).

- [120] P. W. Anderson, Phys. Rev. **79**, 350 (1950).
- [121] L. Pitaevskii and S. Stringari, *Bose-einstein condensation*, International Series of Monographs on Physics (Clarendon Press, 2003).
- [122] A. Crubellier, O. Dulieu, F. Masnou-Seeuws, M. Elbs, H. Knöckel, and E. Tiemann, Eur. Phys. J. D **6**, 211 (1999).
- [123] N. N. Klausen, J. L. Bohn, and C. H. Greene, Phys. Rev. A **64**, 053602 (2001).
- [124] E. G. M. van Kempen, S. J. J. M. F. Kokkelmans, D. J. Heinzen, and B. J. Verhaar, Phys. Rev. Lett. **88**, 093201 (2002).
- [125] J. Werner, A. Griesmaier, S. Hensler, J. Stuhler, T. Pfau, A. Simoni, and E. Tiesinga, Phys. Rev. Lett. **94**, 183201 (2005).
- [126] B. Pasquiou, G. Bismut, Q. Beaufils, A. Crubellier, E. Maréchal, P. Pedri, L. Vernac, O. Gorceix, and B. Laburthe-Tolra, Phys. Rev. A **81**, 042716 (2010).
- [127] D. M. Stamper-Kurn and M. Ueda, Rev. Mod. Phys. **85**, 1191 (2013).
- [128] C. Pethick and H. Smith, *Bose-einstein condensation in dilute gases* (Cambridge University Press, Cambridge, United Kingdom, 2002).
- [129] S. Kotochigova and A. Petrov, Phys. Chem. Chem. Phys. **13**, 19165 (2011).
- [130] S. Ronen, D. C. E. Bortolotti, D. Blume, and J. L. Bohn, Phys. Rev. A **74**, 033611 (2006).
- [131] S. Yi and L. You, Phys. Rev. A **63**, 053607 (2001).
- [132] M. P. A. Fisher, P. B. Weichman, G. Grinstein, and D. S. Fisher, Phys. Rev. B **40**, 546 (1989).
- [133] H. A. Gersch and G. C. Knollman, Phys. Rev. **129**, 959 (1963).
- [134] I. Affleck, Journal of Physics: Condensed Matter **1**, 3047 (1989).
- [135] K. Chang, I. Affleck, G. W. Hayden, and Z. G. Soos, Journal of Physics: Condensed Matter **1**, 153 (1989).
- [136] J. B. Parkinson, Journal of Physics C: Solid State Physics **20**, L1029 (1987).
- [137] J. B. Parkinson, Journal of Physics C: Solid State Physics **21**, 3793 (1988).
- [138] M. N. Barber and M. T. Batchelor, Phys. Rev. B **40**, 4621 (1989).
- [139] A. Läuchli, G. Schmid, and S. Trebst, Phys. Rev. B **74**, 144426 (2006).
- [140] J. Oitmaa and C. J. Hamer, Phys. Rev. B **87**, 224431 (2013).
- [141] A. R. Moura and A. R. Pereira, Journal of Magnetism and Magnetic Materials **342**, 11 (2013).
- [142] F. Zhou, Eur. Lett. **63**, 505 (2003).
- [143] F. Zhou and M. Snoek, Ann. Phys. (N. Y). **308**, 692 (2003).
- [144] C. M. Puetter, M. J. Lawler, and H.-Y. Kee, Phys. Rev. B **78**, 165121 (2008).

- [145] R. Barnett, A. Turner, and E. Demler, *Phys. Rev. Lett.* **97**, 180412 (2006).
- [146] R. Barnett, A. Turner, and E. Demler, *Phys. Rev. A* **76**, 013605 (2007).
- [147] C. Chin, R. Grimm, P. Julienne, and E. Tiesinga, *Rev. Mod. Phys.* **82**, 1225 (2010).
- [148] M. Junker, D. Dries, C. Welford, J. Hitchcock, Y. P. Chen, and R. G. Hulet, *Phys. Rev. Lett.* **101**, 060406 (2008).
- [149] S. Kokkelmans, “Feshbach resonances in ultracold gases”, in *Quantum gas experiments* (Imperial College Press, 2014) Chap. Chapter 4, pp. 63–85.
- [150] J. Dalibard, “Collisional dynamics of ultra-cold atomic gases”, in *Proceedings of the international school of physics ”enrico fermi”* (1999), pp. 1–29.
- [151] L. M. Duan, *Phys. Rev. Lett.* **95**, 1 (2005).
- [152] T. Stöferle, H. Moritz, K. Günter, M. Köhl, and T. Esslinger, *Phys. Rev. Lett.* **96**, 1 (2006).
- [153] M. L. Wall and L. D. Carr, *Phys. Rev. A - At. Mol. Opt. Phys.* **87**, 1 (2013).
- [154] R. B. Diener and T.-L. Ho, *Phys. Rev. Lett.* **96**, 190405 (2006).
- [155] D. B. M. Dickerscheid, U. Al Khawaja, D. van Oosten, and H. T. C. Stoof, *Physical Review A* **71**, 043604 (2005).
- [156] P. O. Fedichev, Y. Kagan, G. V. Shlyapnikov, and J. T. M. Walraven, *Phys. Rev. Lett.* **77**, 2913 (1996).
- [157] M. Theis, G. Thalhammer, K. Winkler, M. Hellwig, G. Ruff, R. Grimm, and J. H. Denschlag, *Phys. Rev. Lett.* **93**, 123001 (2004).
- [158] G. Thalhammer, M. Theis, K. Winkler, R. Grimm, and J. H. Denschlag, *Phys. Rev. A* **71**, 033403 (2005).
- [159] J. D. Miller, R. A. Cline, and D. J. Heinzen, *Phys. Rev. Lett.* **71**, 2204 (1993).
- [160] C. D. Hamley, E. M. Bookjans, G. Behin-Aein, P. Ahmadi, and M. S. Chapman, *Phys. Rev. A* **79**, 023401 (2009).
- [161] J. M. Gerton, B. J. Frew, and R. G. Hulet, *Phys. Rev. A* **64**, 053410 (2001).
- [162] W. C. Stwalley and H. Wang, *Journal of Molecular Spectroscopy* **195**, 194 (1999).
- [163] H. Jelassi, B. V. de Lesegno, and L. Pruvost, *Phys. Rev. A* **74**, 012510 (2006).
- [164] H. Jelassi, B. Viaris de Lesegno, and L. Pruvost, *Phys. Rev. A* **73**, 032501 (2006).
- [165] M. Kemmann, I. Mistrik, S. Nussmann, H. Helm, C. J. Williams, and P. S. Julienne, *Phys. Rev. A* **69**, 022715 (2004).
- [166] H. Wang, P. L. Gould, and W. C. Stwalley, *Phys. Rev. A* **53**, R1216 (1996).
- [167] H. Wang, A. Nikolov, J. Ensher, P. Gould, E. Eyler, W. Stwalley, J. Burke Jr, J. Bohn, C. H. Greene, E. Tiesinga, et al., *Phys. Rev. A* **62**, 052704 (2000).

- [168] M. Pichler, H. Chen, H. Wang, W. Stwalley, A. Ross, F. Martin, M. Aubert-Frécon, and I. Russier-Antoine, *J. Chem. Phys.* **118**, 7837 (2003).
- [169] R. Ciuryło, E. Tiesinga, and P. S. Julienne, *Phys. Rev. A* **74**, 022710 (2006).
- [170] R. Ciuryło, E. Tiesinga, and P. S. Julienne, *Phys. Rev. A* **71**, 030701 (2005).
- [171] T. Rom, T. Best, O. Mandel, A. Widera, M. Greiner, T. W. Hänsch, and I. Bloch, *Phys. Rev. Lett.* **93**, 073002 (2004).
- [172] R. Wynar, R. S. Freeland, D. J. Han, C. Ryu, and D. J. Heinzen, *Science* **287**, 1016 (2000).
- [173] M. Theis, “Optical feshbach resonances in a bose-einstein condensate”, Ph.D. thesis (University of Innsbruck, Innsbruck, 2005).
- [174] M. Egorov, B. Opanchuk, P. Drummond, B. V. Hall, P. Hannaford, and A. I. Sidorov, *Phys. Rev. A* **87**, 053614 (2013).
- [175] W. Salzmann, T. Mullins, S. Götz, M. Albert, J. Eng, R. Wester, M. Weidemüller, F. Weise, A. Merli, S. M. Weber, et al., arXiv:0903.454 (2009).
- [176] B. Sundar and E. J. Mueller, *Phys. Rev. A* **93**, 023635 (2016).
- [177] J. Bohn and P. Julienne, *Phys. Rev. A* **56**, 1486 (1997).
- [178] T. Maier, I. Ferrier-Barbut, H. Kadau, M. Schmitt, M. Wenzel, C. Wink, T. Pfau, K. Jachymski, and P. S. Julienne, *Phys. Rev. A* **92**, 060702 (2015).
- [179] M. Yan, B. J. DeSalvo, B. Ramachandhran, H. Pu, and T. C. Killian, *Phys. Rev. Lett.* **110**, 123201 (2013).
- [180] C. Samuelis, E. Tiesinga, T. Laue, M. Elbs, H. Knöckel, and E. Tiemann, *Physical Review A* **63**, 012710 (2000).
- [181] S. Dutta, D. S. Elliott, and Y. P. Chen, *Europhys. Lett.* **104**, 63001 (2013).
- [182] S. Dutta, J. Lorenz, A. Altaf, D. S. Elliott, and Y. P. Chen, *Phys. Rev. A* **89**, 020702 (2014).
- [183] A. Messiah, *Quantum mechanics*, Vol. II (John Wiley & Sons, New York, 1961).
- [184] Q. Beaufils, A. Crubellier, T. Zanon, B. Laburthe-Tolra, E. Marechal, L. Vernac, and O. Gorceix, *Phys. Rev. A* **79**, 032706 (2009).
- [185] Q. Beaufils, T. Zanon, A. Crubellier, B. Laburthe-Tolra, E. Marechal, L. Vernac, and O. Gorceix, in *European quantum electronics conference 2009 - conference digest* (2009).
- [186] J. Stuhler, A. Griesmaier, J. Werner, T. Koch, M. Fattori, and T. Pfau, *Journal of Modern Optics* **54**, 647 (2007).
- [187] Z. Pavlović, R. V. Krems, R. Côté, and H. R. Sadeghpour, *Phys. Rev. A* **71**, 061402 (2005).
- [188] S. Kotochigova, *Reports on Progress in Physics* **77**, 093901 (2014).
- [189] K. Baumann, N. Q. Burdick, M. Lu, and B. L. Lev, *Phys. Rev. A* **89** (2014).

- [190] S. Giovanazzi, A. Görlitz, and T. Pfau, Phys. Rev. Lett. **89**, 130401 (2002).
- [191] A. Gorlitz, S. Giovanazzi, and T. Pfau, “Observing and tuning the dipolar interaction in a bose-einstein condensate”, in *European quantum electronics conference* (June 2003).
- [192] T. Lahaye, C. Menotti, L. Santos, M. Lewenstein, and T. Pfau, Rep. Prog. Phys. **72**, 126401 (2009).
- [193] K. Jensen, V. M. Acosta, J. M. Higbie, M. P. Ledbetter, S. M. Rochester, and D. Budker, Phys. Rev. A **79**, 023406 (2009).
- [194] F. Gerbier, A. Widera, S. Fölling, O. Mandel, and I. Bloch, Phys. Rev. A **73**, 041602 (2006).
- [195] Y. Kawaguchi and M. Ueda, Physics Reports **520**, 253 (2012).
- [196] M. Snoek and F. Zhou, Physical Review B **69**, 094410 (2004).
- [197] R. Ciuryło, E. Tiesinga, and P. S. Julienne, Phys. Rev. A **71**, 030701 (2005).
- [198] K. Enomoto, K. Kasa, M. Kitagawa, and Y. Takahashi, Phys. Rev. Lett. **101**, 203201 (2008).
- [199] D. J. Papoular, G. V. Shlyapnikov, and J. Dalibard, Phys. Rev. A **81**, 041603 (2010).
- [200] S. Yi, Ö. E. Müstecaplıoğlu, C. P. Sun, and L. You, Phys. Rev. A **66**, 011601 (2002).
- [201] T.-L. Ho and S. Yip, Phys. Rev. Lett. **82**, 247 (1999).
- [202] S. Sachdev, Phys. Rev. B **45**, 12377 (1992).
- [203] N. Read and S. Sachdev, Physical Review Letters **66**, 1773 (1991).
- [204] S. Sachdev and N. Read, Int. J. Mod. Phys. B **05**, 219 (1991).
- [205] N. Read and S. Sachdev, Phys. Rev. B **42**, 4568 (1990).
- [206] J. B. Marston and I. Affleck, Phys. Rev. B **39**, 11538 (1989).
- [207] N. Read and B. Chakraborty, Phys. Rev. B **40**, 7133 (1989).
- [208] N. Read and S. Sachdev, Phys. Rev. Lett. **62**, 1694 (1989).
- [209] D. Yoshioka, J. Phys. Soc. Japan **58**, 3733 (1989).
- [210] D. Yoshioka, J. Phys. Soc. Japan **58**, 32 (1989).
- [211] A. Auerbach and D. P. Arovas, Phys. Rev. Lett. **61**, 617 (1988).
- [212] D. P. Arovas and A. Auerbach, Phys. Rev. B **38**, 316 (1988).
- [213] K. Harada, N. Kawashima, and M. Troyer, Phys. Rev. Lett. **90**, 117203 (2003).
- [214] L. Savary and L. Balents, Reports on Progress in Physics **80**, 016502 (2017).
- [215] N. Read and S. Sachdev, Nucl. Phys. B **316**, 609 (1989).
- [216] D. S. Rokhsar and B. G. Kotliar, Phys. Rev. B **44**, 10328 (1991).

- [217] C. V. Ciobanu, S.-K. Yip, and T.-L. Ho, Phys. Rev. A **61**, 033607 (2000).
- [218] M. Ueda and M. Koashi, Phys. Rev. A **65**, 063602 (2002).
- [219] L. Santos and T. Pfau, Phys. Rev. Lett. **96**, 190404 (2006).
- [220] H. Mäkelä and K.-A. Suominen, Phys. Rev. A **75**, 033610 (2007).
- [221] A. M. Turner, R. Barnett, E. Demler, and A. Vishwanath, Phys. Rev. Lett. **98**, 190404 (2007).
- [222] J. L. Song, G. W. Semenoff, and F. Zhou, Phys. Rev. Lett. **98**, 160408 (2007).
- [223] C. Wu, J.-p. Hu, and S.-c. Zhang, Phys. Rev. Lett. **91**, 186402 (2003).
- [224] S. Trotzky, Y.-A. Chen, U. Schnorrberger, P. Cheinet, and I. Bloch, Phys. Rev. Lett. **105**, 265303 (2010).
- [225] E. R. I. Abraham, W. I. McAlexander, H. T. C. Stoof, and R. G. Hulet, Phys. Rev. A **53**, 3092 (1996).
- [226] I. D. Prodan, M. Pichler, M. Junker, R. G. Hulet, and J. L. Bohn, Phys. Rev. Lett. **91**, 080402 (2003).
- [227] D. A. Bonn, J. C. Wynn, B. W. Gardner, Y.-J. Lin, R. Liang, W. N. Hardy, J. R. Kirtley, and K. A. Moler, Nature (London) **414**, 887 (2001).
- [228] C. Menotti and M. Lewenstein, in *Recent progress in many-body theories: proceedings of the 14th international conference, barcelona, spain, 16-20 july 2007*, edited by J. Boronat, G. Astrakharchik, and F. Mazzanti, Series on advances in quantum many-body theory (World Scientific, Singapore, 2008), pp. 79–93.
- [229] A. Ralko, M. Ferrero, F. Becca, D. Ivanov, and F. Mila, Phys. Rev. B. **71**, 1 (2005).
- [230] C. Zeng and V. Elser, Phys. Rev. B **51**, 8318 (1995).
- [231] P. W. Leung, K. C. Chiu, and K. J. Runge, Phys. Rev. B **54**, 12938 (1996).
- [232] D. Banerjee, M. Bögli, C. P. Hofmann, F.-J. Jiang, P. Widmer, and U.-J. Wiese, Phys. Rev. B **90**, 245143 (2014).
- [233] R. Moessner and K. S. Raman, in *Introduction to frustrated magnetism*, Vol. 164, edited by C. Lacroix, P. Mendels, and F. Mila, First, Springer Series in Solid-State Sciences (Springer-Verlag, 2011) Chap. 17, pp. 437–479.
- [234] R. Moessner, S. L. Sondhi, and P. Chandra, Phys. Rev. B **64**, 144416 (2001).
- [235] R. Moessner and S. L. Sondhi, Prog. Theor. Phys. Suppl. **145**, 37 (2002).
- [236] O. F. Syljuasen, Phys. Rev. B **73**, 245105 (2006).
- [237] A. Ralko, D. Poilblanc, and R. Moessner, Phys. Rev. Lett. **100**, 2 (2008).
- [238] K. Nakata and K. Totsuka, J. Stat. Mech. Theor. Exp. **2011**, 01033 (2011).
- [239] W. S. Bakr, J. I. Gillen, A. Peng, S. Fölling, and M. Greiner, Nature **462**, 74 (2009).

- [240] K. M. Jones, E. Tiesinga, P. D. Lett, and P. S. Julienne, *Rev. Mod. Phys.* **78**, 483 (2006).
- [241] I. Lindgren, *Journal of Physics B: Atomic and Molecular Physics* **7**, 2441 (1974).